A study of Gamow-Teller strength using the ^{208}Pb(p,n) and ^{181}Ta(p,n) reactions at intermediate energy, E_p=122 MeV

Victor Makondelele Tshivhase

Thesis presented
for the degree of Doctor of Philosophy
in the Department of Physics
Faculty of Science
University of Cape Town

April 1997

Abstract

A study of Gamow-Teller strength using the ^{208}Pb(p,n) and ^{181}Ta(p,n) reactions at intermediate energy, E_p=122 MeV

Victor Makondelele Tshivhase

University of Cape Town, P/Bag, Rondebosch, 7700, South Africa

e-mail: tshivhase@nac.ac.za

The Gamow-Teller strength was measured in ^{208}Pb(p,n)^{208}Bi and ^{181}Ta(p,n)^{181}W reactions at an incident proton energy of 122 MeV. The experiment was performed using the beam-swinger facility at the National Accelerator Centre, Faure, South Africa. The time-of-flight(TOF) technique was employed with a flight-path of 100 m. Detectors comprised three stacks of four rectangular bars of NE 102A plastic scintillators. The outgoing neutrons were observed at laboratory angles, Θ_{Lab} = 0°, 2°, 4° and 10°.

A multipole decomposition analysis of spectra associated with ^{208}Pb(p,n)^{208}Bi and ^{181}Ta(p,n)^{181}W reactions was performed using the results of distorted-wave impulse approximation (DWIA) calculations. The spectra associated with the two reactions were decomposed into L=0,1 and 2 transfer components. The major contribution to the spectra were found to be L=0, with a very small L=2 multipole transfer contribution.

The spectra were modelled with a combination of symmetrical Gaussians and a polynomial background. The *GT* strength was extracted by normalizing the cross section of the *GT* states to the cross section of the isobaric analogue state.

The $\sum B(GT)$ strength associated with the ^{208}Pb(p,n)^{208}Bi and ^{181}Ta(p,n)^{181}W reactions was found by summing the individual GT strength in the 0–23 MeV and 0–20 MeV excitation regions respectively.

The $\sum B(GT)$ strength associated with the ^{208}Pb(p,n)^{208}Bi and ^{181}Ta(p,n)^{181}W reactions were found to be less than the values predicted by the $3(N - Z)$ sum rule, being 81 $\pm$ 10% and 78 $\pm$ 3% of the sum rule strength respectively.

Acknowledgements

I wish to express my appreciation to the following people without whose invaluable help the success of this work would be impossible:

- my supervisor, Prof. D.G. Aschman for his guidance throughout this project.
- the collaborators who participated in the experiment: Prof. D.G. Aschman, Dr. Richard Newman, Dr. Roger Fearick, Dr. Douw Steyn, Mr. Marco Benetar.
- Prof. Charles Goodman for making the visit to Indiana University Cyclotron Facility possible and his valuable suggestion.
- Prof. Jack Rapaport, Dr. Xun Wang and Dr. David Prout for their help in my struggle to understand DW81.
- Foundation for Research and Development, University of Cape Town and National Accelerator Centre (NAC) for their financial support.
- Prof. J. F. Sharpey-Schafer and the NAC program advisory committee for their allocation of beam time to this experiment.
- Dr. Gideon Steyn for manufacturing the lithium target.
- Dr. Adriaan Botha and his operators for producing a high quality proton beam.
- Mr. Charles Wikner who was of great assistance in electronics.
- Mr. Dave Boulton, Mr. Graham Fowle and Mr. Danie Momsen for constructing the detectors.
- Dr. John Pilcher, Dr. Richard Newman, Dr. Jacobus Lawrie, Dr. Fredrick Smit and Dr. Douw Steyn for their assistance with online and offline software.

- Dr. John Pilcher for his assistance in computing and maintaining the data acquisition system.

- Dr. Salie Allie, Mr. Andy Buffler, Dr. Loveness Makina-Kaunda, Dr. Richard Newman, Dr. John Pilcher and Dr. Fredrick Smit for proofreading this document.

- my parents for their encouragement and moral support that motivated me into University studies.

Contents

List of figures

List of tables

Chapter 1

Introduction

Nuclear physics originated in 1896 after the discovery of radioactivity in radioactive compounds by Becquerel. Extensive research was performed in an attempt to understand and characterize the nature of radiation emitted by radioactive nuclei. Rutherford classified emitted radiation as alpha, beta and gamma rays. Rutherford and his students Geiger and Marsden carried out a number of scattering experiments and later established that the nucleus of an atom can be regarded as a point mass and point charge. These experiments demonstrated that nuclear force is a short-range force. Since then a number of experiments were performed in order to understand the constituents of nuclei. The nucleon-nucleon (NN) interaction is the most important factor governing the properties of a nucleus. The (p,n) experiments are performed to complement β-decay in studying the NN interaction as discussed in the next section.

The time-of-flight technique established by Alvarez et al. in 1938 became a powerful technique to measure neutron energy. In 1962 Anderson et al. discovered the isobaric analog state, which dominates the (p,n) spectra in the 10 - 40 MeV energy range. Ikeda et al. suggested that the Gamow-

Teller strength (B(GT)) function is localized near the isobaric analog state as part of a broken but persistent, Wigner supermultiplet [Ike 63]. The giant Gamow-Teller resonance (GTGR) was later discovered in 1975 by Doering et al..

At the Indiana University Cyclotron Facility the time-of-flight technique, using large scintillators with subnanosecond time resolution [Goo 79] was extended to make (p,n) studies at intermediate energies. These (p,n) measurements yielded valuable information about the spin-isospin dependent part of the effective NN interaction and also mapped the B(GT) function in nuclei.

The next section in this chapter begins by describing in detail the main theoretical concepts underpinning this study; namely the isobaric analog state, the Gamow-Teller resonance, the independent sum rule, the distorted-wave impulse approximation and the t_F matrix interaction. Chapter 1 is concluded by outlining the aims and objectives of this study.

In chapter 2 the experimental arrangement, electronics used, data acquisition system and experimental procedure are discussed. Data analysis, generation of time-of-flight spectra, background subtraction, energy calibration of the spectrum, modelling of the spectra, cross section calculations and extraction of B(GT) are discussed in chapter 3. To conclude chapter 3 the results are tabulated, compared with the independent sum rule value of $3(N-Z)$ and also compared with data on neighbouring nuclei (A = 165 and 205) available in the literature.

In conclusion the results obtained are discussed relative to the independent sum rule. A comparison of quenching of the B(GT) in the two reactions is then made. In appendix A multipole and distorted-wave analysis are outlined qualitatively. The different types of systematic errors involved in

the experiment are discussed in appendix B.

1.1 Theoretical Background

Beta decay is a very simple tool to study the nuclear structure, transforms a neutron(proton) to proton(neutron) and at the same time emits a β^- (β^+)-particle and an anti-neutrino(neutrino). The leptons carry off little momentum, the transition favours L=0 which is an allowed transition (where L is the total angular momentum of the lepton system with respect to the nucleus). Transitions with L>0 are possible and are forbidden. We are only interested in allowed transitions which exist in forms according to the spin coupling of the leptons. If the two leptons have total spin S=0, the transition is of Fermi type and no spin is transferred to the nucleon. If they have S=1, the transition is of Gamow-Teller(GT) type and one unit of spin is tranferred. Fermi and Gamow-Teller transitions do not involve changes in spatial configuration. In a shell-model picture in which the nucleus may be represented by a pattern of occupancy nucleons. The effect of Fermi decay is to flip one of the nucleon's isospin without disturbibg the remaining part of the wave function. The effect of Gamow-Teller decay is to flip both the spin and the isospin of a single nucleon. The transition strength to a daughter state is proportional to the overlap of the new wave function resulting from the above spin-isospin flips and the daughter wave function. The transition strength reflects the structure of the nucleus [Goo 83].

The giant multipole resonances are elementary modes of nuclear excitations which involve the coherent motion of many nucleons in the nucleus, e.g. the shape and density oscillations of the nucleus around its equilibrium configuration [Ost 92]. The isoscalar ($\Delta T = 0$) modes - giant quadrupole

resonance ($J^\pi = 2^+$, $\Delta T = 0$) [Pit 71] [Lew 72] and the giant monopole resonance ($J^\pi = 0^+$, $\Delta T = 0$) [Mar 75] [Har 77] [You 77] [Ros 80] [You 81] - are vibrations where the neutrons and protons move in phase. The modes in which protons and neutrons move out of phase are called isovector e.g. giant dipole resonance ($J^\pi = 1^-$, $\Delta T = 1$) [Bal 47].

Nucleons with spin-up and spin-down may move either in phase (spin-scalar $\Delta S = 0$ - modes) or out of phase (spin-vector $\Delta S = 1$ - modes). The latter are known as spin excitations or spin-flip transitions. These spin excitations are again subdivided into isoscalar spin-flip ($\Delta S = 1, \Delta T = 0$) and isovector spin-flip ($\Delta S = 1, \Delta T = 1$) states. Collective spin modes provide direct information on the spin and spin-isospin dependent effective interactions in the nuclear medium.

To probe the spin excitations one can use the weak or the strong interactions. In the weak interaction the axial vector current couples to the spin of the nucleon and induces the Gamow-Teller (GT) transitions of the nuclear $\beta_\pm$-decay [Boh 69]. The GT transitions are mediated by a spin-isospin product operator of the form $g_A\vec{\sigma}\tau_\pm$, where g_A is the axial vector coupling constant. By studying these transitions one obtains valuable information on the spin-isospin properties of nuclei. β-decay has access to nuclear states in a very limited energy range. In order to map out the complete response function in the $\vec{\sigma}\tau_\pm$ channels, one needs hadronic probes such as (p,n) and (n,p) charge exchange reactions which allow the independent variation of both energy transfer and momentum transfer to the target nucleus.

The V_o, V_τ and V_σ terms in the NN potential are at minimum in the region were the proton beam energy (E_p) is more than 100 MeV and less than

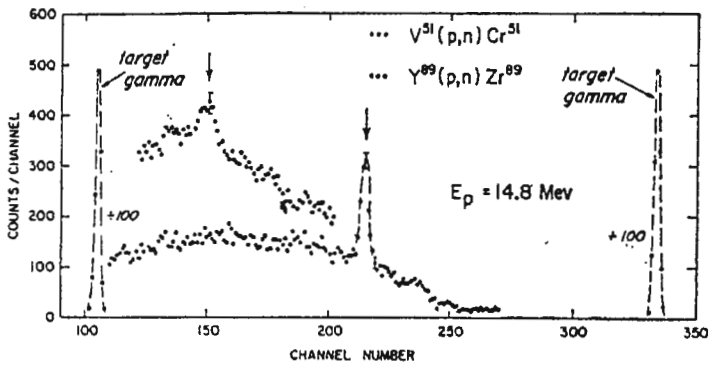

Figure 1.1: *The Isobaric Analog State discovery spectrum by Anderson et al. [And 62]. The IAS from two different reactions are indicated by the arrows.*

400 MeV as shown in figure 1.6. The production at National Accelerator Centre (NAC) of a proton beam with narrow time structure is well understood in the region of 120 to 160 MeV. At $E_p = 122$ MeV there is less background than at higher energies in the TOF spectra and ^{7}Li cross sections are readily available in literature for detector's efficiency determination.

1.1.1 Isobaric Analog State

The IAS was first discovered by Anderson and Wong [And 61] in a study of the ^{51}V(p,n)^{51}Cr reaction at $E_p = 14$ MeV, the spectra is shown in figure 1.1.

The IAS is reached by acting on the target ground state with the Fermi-operator

$$T_- = \frac{1}{2}\sum_{j=1}^{A} \tau_-(j).$$

The strength is concentrated in one state and the distribution is almost a delta function. The single-particle transitions involved in the ^{90}Zr nucleus

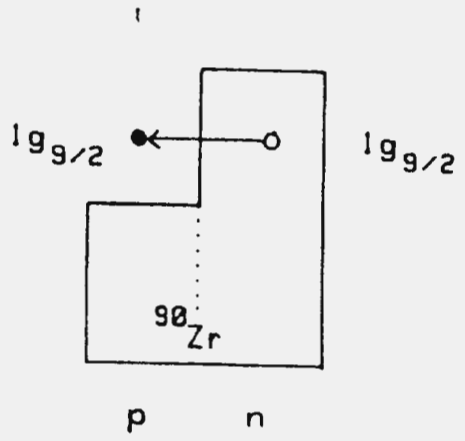

Figure 1.2: *Schematic representation of the single particle transitions involved in the Fermi transition. From ref. [Ost 92].*

are shown in figure 1.2. The (p,n)-reaction excites the IAS through the force component $V_\tau \vec{\tau}_p . \vec{\tau}_j$ which contains no spin operator.
The interaction strength V_τ gets strongly reduced with increasing projectile energy while the interaction strength $V_{\sigma\tau}$ is roughly independent of the incident energy, e.g. figure 1.3 shows the ^{14}C(p,n)^{14}N spectra [Ost 92] at different energies.

1.1.2 Gamow-Teller resonance

The existence of collective spin-isospin modes in the nucleus were demonstrated by (p,n) charge-exchange experiments [And 80] [Bai 80] [Gaa 81] [Goo 80] [Hor 80] [Hor 81] [Rap 81] [Pet 84]. The spectra from such experiments for target nuclei with neutron excess, i.e. $(N - Z) \geq 0$, are dominated by the giant Gamow-Teller resonance (GTGR) predicted by Ikeda, Fujii and Fujita in 1963 [Ike 63]. The first experimental evidence of the GTGR was

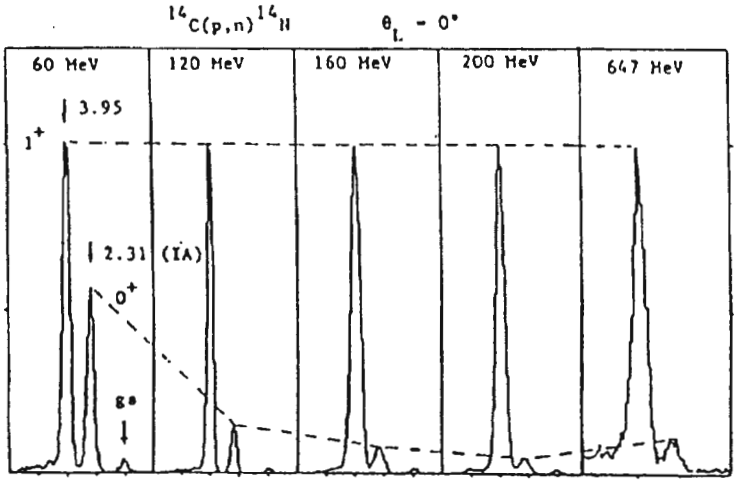

Figure 1.3: *Zero-degree cross section spectra for* ^{14}C(p,n)^{14}N *reactions at the indicated bombarding energies. From McClelland et al. [Mcc 87].*

found by Doering et al. [Doe 75] using the ^{90}Zr(p,n)^{90}Nb reaction at 35 MeV. (see figure 1.4.).

The GTGR is a collective spin-isospin oscillation where the excess neutrons coherently change the direction of their spins and isospins without changing their orbital motion. For a target ground state with spin-parity $J^\pi = 0^+$ the spin transfer then makes the GTGR a $J^\pi = 1^+$ state.

The single-particle transitions contributing to the GT-oscillation are shown in figure 1.5 for the closed shell nucleus ^{90}Zr. To excite these transitions one has to apply to the target ground-state the GT transition operator:

$$\beta_\pm(\mu) = \frac{1}{2}\sum_{j=1}^{A}\sigma_\mu(j)\tau_\pm(j) \tag{1.1}$$

Unlike the Fermi operator, the Gamow-Teller strength is shared by a number of adjacent states. The strength in the ^{90}Zr(p,n)^{90}Nb reaction appears as a giant resonance in the neutron spectra shown in figure 1.4 at neutron energies

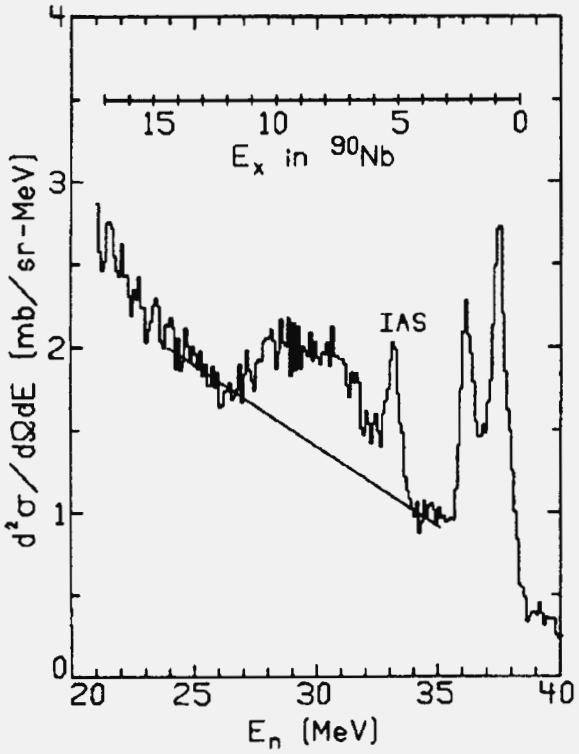

Figure 1.4: *The Gamow-Teller resonance discovery spectrum at $\theta = 0°$ for $^{90}Zr(p,n)^{90}Nb$ at $E_p = 45$ MeV by Doering et al. [Doe 75]. The GTGR lies between E_x 6 and 12 MeV.*

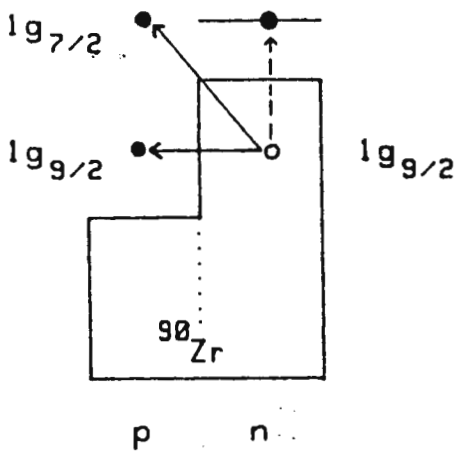

Figure 1.5: *Schematic picture of the single-particle transitions involved in the Gamow-Teller transition. The transitions are excited by the $\beta_-(\mu)$ operator. From ref. [Ost 92].*

just below the IAS peak, where the $\sigma_\mu(j)$ are the spherical components of the Pauli spin matrices and $\tau_\pm(j) = \tau_x(j) \pm i\tau_y(j)$ are the isospin ladder operators converting a neutron into a proton $(-)$ and vice versa $(+)$.

In the (p,n)-reaction the GT operator is contained in the $V_{\sigma\tau}\vec{\sigma}_p.\vec{\sigma}_j\vec{\tau}_p.\vec{\tau}_j$ component of the projectile-target nucleon interaction, where p and j denote the projectile and struck target nucleon respectively.

1.1.3 Sum rules

For both Gamow-Teller and Fermi operators there exist model-independent sum rules [Ike 63] [Gaa 81].

For Fermi transitions

$$S_{\beta_-}(F) - S_{\beta_+}(F) = \sum_f |< f|T_-|i >|^2 - \sum_f |< f|T_+|i >|^2$$
$$\sum B(F)^- - \sum B(F)^+ = (N - Z)$$

and for GT transitions we obtain

$$S_{\beta_-}(GT) - S_{\beta_+}(GT) = \sum_{f,\mu} |< f|\beta_-(\mu)|i >|^2 - \sum_{f,\mu} |< f|\beta_+(\mu)|i >|^2$$

where

- $B(F)$ is the Fermi transition probability,
- $B(GT)$ is the Gamow-Teller transition probability,
- N is the number of neutrons, and
- Z is the number of protons.

Replacing $\beta_-(\mu)$ and $\beta_+(\mu)$ by equation 1.1 and using the fact that for a single nucleon the intrinsic spin $\vec{s} = \frac{1}{2}\vec{\sigma}$, where $\vec{\sigma}$ is the Pauli spin matrices, and the expectation value of $\vec{\sigma}^2$ is 3. We obtain the GT sum rule to be

$$\sum B(GT)^- - \sum B(GT)^+ = 3(N - Z).$$

The Fermi strength is assumed to be concentrated in the IAS transtion. For nuclei with an excess on neutrons over protons,
$\sum B(F)^+ = 0$ and $\sum B(F)^- = N - Z$.
The GT strength (B(GT)) may be spread over many states and exists in both β^- and β^+ decays. But the minimum total strength will always be

$$\sum B(GT)^- \geq 3(N - Z).$$

For nuclei with large neutron excesses, the β^+ strength is Pauli blocked and the total $\sum B(GT)^- \approx 3(N-Z)$.

1.1.4 Scattering observables

To evaluate and interpret the nucleon-nucleus inelastic scattering observables we need to construct the transition amplitude $\mathcal{T}_{fi}$. The $\mathcal{T}_{fi}$ describes the transition of the scattering system from the initial (i) to the final (f) reaction channel.

The spin quantum numbers of the projectile and target are denoted by $|\frac{1}{2}, m>$ and $|I, M>$ respectively. The transition operator $\mathcal{T}$ can be written as

$$\mathcal{T}_{fi} =< \vec{k}_f, I_f M_f, \frac{1}{2} m_f | \mathcal{T} | \vec{k}_i, I_i M_i, \frac{1}{2} m_i >$$

where $\vec{k}_i$ and $\vec{k}_f$ are the projectile momenta before and after the collision. The scattering amplitude $\mathcal{M}_{fi}$ is related to the transition amplitude and defined [Ost 92] by

$$\mathcal{M}_{fi} = -\frac{\mu}{2\pi h^2} \sqrt{\frac{k_f}{k_i}} \mathcal{T}_{fi}$$

where μ is the reduced mass ($\mu_i \approx \mu_f$ for inelastic scattering and charge exchange reactions).

Different scattering observables can be constructed from the scattering amplitude. For example, the differential cross section for an unpolarized (u) beam is given by

$$\sigma_u(\theta) = \frac{d\sigma}{d\Omega}$$

$$
\begin{aligned}
&= \frac{1}{2(2I_i+1)} \sum_{m_i m_f}^{M_i M_f} | < I_f M_f, \frac{1}{2} m_f | \mathcal{M} | I_i M_i, \frac{1}{2} m_i > |^2 \\
&\equiv \frac{1}{2(2I_i+1)} \mathrm{Tr}(\mathcal{M}\mathcal{M}^\dagger) \\
&\equiv \sum_{m_i m_f} \sigma_{m_i m_f}.
\end{aligned}
$$

Here $\mathcal{M}$ is an operator and the cross section σ_u is a function of the scattering angle θ between $\vec{k}_i$ and $\vec{k}_f$.

1.1.5 Distorted-wave approximation

At incident proton energies above 100 MeV the (p,n) reaction mechanism operative is preferentially of a direct, one-step nature [Ost 92], hence the transition operator $\mathcal{T}$ simplifies. The inelastic transition between target states can be evaluated to first order in an effective interaction $V_{pt} = \sum_{j=1}^{A} V_{pj}$ between the projectile nucleon p and the jth nucleon in the target. The interaction V_{pt} has large diagonal matrix elements in the target states. These matrix elements represent average one-body potentials which govern the relative-motion wave function of the projectile and target before and after the inelastic scattering event, making them distorted waves [Ker 59]. Hence

$$
\mathcal{T}_{if}^{DW} = \int d\vec{r}_p \chi_f^{(-)^*}(\vec{k}_f, \vec{r}_p) < I_f M_f, \frac{1}{2} m_f | \sum_{j=1}^{A} V_{pj} | I_i M_i, \frac{1}{2} m_i > \chi_i^{(+)}(\vec{k}_i, \vec{r}_p). \tag{1.2}
$$

Here $\mathcal{T}_{if}^{DW}$ is the distorted-wave approximation to the scattering amplitude, and $\chi_i^{(+)}$ and $\chi_f^{(-)^*}$ are distorted waves of the projectile in the initial and final states respectively, $|I_i M_i >$ and $|I_f M_f >$ are associated many-particle wave functions of the target states. In actual calculations one has to accommodate the exchange effects by replacing V_{pj} by $\bar{V}_{pj} = V_{pj}(1 - \mathcal{P}_{pj})$, where $\mathcal{P}_{pj}$ is the

exchange operator that exchanges the space, spin, and isospin coordinates of the nucleons p and j, hence the nonlocal effective interaction. At high incident energies nonlocal operators can be well approximated by a local form [Pet 69]. With these assumptions the transition amplitude in Eq 1.2 is factorizable into a nuclear structure part and a nuclear reaction part [Sat 83] [Pet 86] i.e.

$$\mathcal{T}_{fi}^{DW}(\vec{k}_f, \vec{k}_i) = \int d\vec{q} D(\vec{k}_f, \vec{k}_i, \vec{q}) V(\vec{q}) \rho_{I_f I_i}(\vec{q}) \tag{1.3}$$

where

$$\rho_{I_f I_i}(\vec{q}) \equiv < I_f M_f | \sum_{j=1}^{A} \delta(\vec{r} - \vec{r}_j) | I_i M_i > .$$

is the nuclear transition density in $\vec{q}$ space, and where $D(\vec{k}_f, \vec{k}_i, \vec{q})$ is the projectile distortion function defined by

$$D(\vec{k}_f, \vec{k}_i, \vec{q}) = \frac{1}{(2\pi)^3} \int d\vec{r}_p \chi_{\frac{1}{2}} m_f^{(-)^*}(\vec{k}_f, \vec{r}_p) \times \exp[-i\vec{q}\cdot\vec{r}_p] \chi_{\frac{1}{2}} m_i^{(+)}(\vec{k}_i, \vec{r}_p). \tag{1.4}$$

For a detailed derivation of equation 1.4. see reference [Ost 92]. By transforming equation 1.3 into r-space we obtain

$$\mathcal{T}_{fi}^{DW}(\vec{k}_f, \vec{k}_i) = \int d\vec{r} \rho_{I_f I_i}(\vec{r}) P(\vec{k}_f, \vec{k}_i, \vec{r}),$$

where

$$P(\vec{k}_f, \vec{k}_i, \vec{r}) = \int d\vec{q} \ \exp[i\vec{q}\cdot\vec{r}] D(\vec{k}_f, \vec{k}_i, \vec{q}) V(\vec{q})$$

is known as the hadronic transition operator [Ber 70] [Sat 83]. This is the interaction operator or probe seen by the target during collision.

1.1.6 Effective projectile-target nucleon interaction.

To extract the nuclear structure information from $\mathcal{T}_{fi}$ one needs to know the effective interaction V_{pj}. It depends on the incident projectile energy $E_{\rm p}$ and each scattering situation starting from a bare nucleon-nucleon (NN) potential V_{NN} which, when used in a two-body Schrodinger equation, describes the free NN scattering data.

Modern NN-potentials [Erk 74] [Hol 77] [Nag 78] [Lac 80] [Mac 87] are based on meson-exchange models. The long-range part in these potentials is provided by the one-pion exchange, the medium-range attraction is produced by correlated two-pion exchange and the short-range repulsion is due to the exchange of heavy vector mesons. The repulsive core has to be properly regularized by converting the bare potentials V_{NN} into weak effective interactions, before pertubative calculations can be done. The final sum of all interactions is a weak effective interaction represented by the free NN scattering matrix t_F.

In the case of the scattering of the projectile nucleon p from a nucleon j in the nucleus, one has to incorporate the nuclear medium effects into the two-nucleon scattering amplitude. The effective interaction produced is known as Brueckner's scattering matrix G [Bru 54] [Bru 55] [Day 67] [Bet 71] which is the solution of the Bethe-Goldstone equation [Bet 57] defined by

$$G(\omega) = V_{NN} + V_{NN}\frac{Q}{\omega - H_0 + i\epsilon}G(\omega).$$

For high incident-projectile energies, i.e., for energies large compared to the Fermi energy ($\epsilon \sim 37$ MeV) of the nucleons in the target, the G matrix approaches the free t_F matrix.

The replacement of the G by t_F is the impulse approximation [Ker 59], which becomes a good approximation for incident energies greater than about

400 MeV.

1.1.7 The free nucleon-nucleon t_F-matrix interaction

The t_F matrix is related to the NN scattering amplitude M by

$$\begin{aligned} t_F &= -\frac{4\pi(\hbar c)^2}{E_{CM}} M(E_{CM}, \theta), \\ E_{CM}^2 &= m^2c^4 + (\hbar ck)^2, \end{aligned}$$

where E_{CM} and $\hbar k$ are the energy and momentum in the two-nucleon center-of-mass frame, respectively, m is the nucleon rest mass, and θ is the scattering angle between the initial and final momenta $\vec{k}$ and $\vec{k}'$ of either particle.
The scattering amplitude M can be written in a longitudinal transverse representation [Lov 84] [Ber 87] using the relation

$$\sigma_1 \cdot \sigma_2 = \sigma_1 \cdot \hat{q}\sigma_2 \cdot \hat{q} + \sigma_1 \cdot \hat{Q}\sigma_2 \cdot \hat{Q} + \sigma_1 \cdot \hat{n}\sigma_2 \cdot \hat{n} = \sigma_1 \cdot \hat{q}\sigma_2 \cdot \hat{q} + (\sigma_1 \times \hat{q}) \cdot (\sigma_2 \times \hat{q})$$

as

$$M(E_{CM}, \theta) = A + C(\vec{\sigma}_1 + \vec{\sigma}_2) \cdot \hat{n} + E\mathcal{O}_l + \frac{B+F}{2}\mathcal{O}_t + \frac{B-F}{2}\mathcal{O}_u$$

with one longitudinal $\mathcal{O}_l$ and two transverse operators $(\mathcal{O}_t, \mathcal{O}_u)$ where the coefficients A, B, C, E and F are complex functions of the energy E_{CM}, the scattering angle θ, and the two-body isospin.

1.1.8 The construction of a local effective interaction in r space

The free nucleon-nucleon t_F-matrix interaction is defined for free NN kinematics and for antisymmetrized two-nucleon wave functions. In the nucleon-

nucleus scattering one of the nucleons is bound in the target. Love et al. [Lov 81] and Franey et al. [Fra 85] worked out a partial solution to this problem by constructing a coordinate representation of the t matrix which reproduces the scattering matrix in the physically accessible region and provides a way to extrapolate to off-shell momenta,

$$M(E_{CM},\theta) = A'\Lambda_S + B'\Lambda_T + C(\vec{\sigma}_1+\vec{\sigma}_2)\cdot\hat{n} + E'S_{12}(\hat{q}) + F'S_{12}(\hat{Q}),$$

where $S_{12}(\hat{u}) = 3\vec{\sigma}_1\cdot\hat{u}\vec{\sigma}_2\cdot\hat{u} - \vec{\sigma}_1\cdot\vec{\sigma}_2$ is the tensor operator and $\Lambda_S = (1-\vec{\sigma}_1\cdot\vec{\sigma}_2)/4$ and $\Lambda_T = (3+\vec{\sigma}_1\cdot\vec{\sigma}_2)/4$ are the singlet and triplet spin-projection operators respectively. The amplitudes A' and B' represent the central parts of M, and the terms E' and F' represent tensor interactions. The t_F-matrix interaction is obtained by assuming a local functional form $V_{12}(r)$ in the r space and by adjusting its parameters until the antisymmetrized NN matrix element in momentum space

$$t_F(\vec{q},E_{CM}) = \int d\vec{r}\exp[-i\vec{k'}\cdot\vec{r}]V_{12}(\vec{r})(1-\mathcal{P}_{12})\exp[-i\vec{k'}\cdot\vec{r}]$$

reproduces the free t_F matrix in each spin and isospin channel at a given energy E_{CM}.

The effective interaction is then written as a sum of central (C), spin-orbit (LS), and tensor (T) terms with the following spin-isospin decomposition:

$$\begin{aligned} V_{12}(r) &= V_0^C(r) + V_\sigma^C(r)\vec{\sigma}_1\cdot\vec{\sigma}_2 + V_\tau^C(r)\tau_1\cdot\tau_2 + V_{\sigma\tau}^C(r)\vec{\sigma}_1\cdot\vec{\sigma}_2\tau_1\cdot\tau_2 \\ &+ [V^{LS}(r) + V_\tau^{LS}(r)\tau_1\cdot\tau_2]\vec{L}_{12}\cdot S \\ &+ [V^T(r) + V_\tau^T(r)\tau_1\cdot\tau_2]S_{12}(\hat{r}) \end{aligned} \tag{1.5}$$

where $\vec{L}_{12} \equiv (\vec{r}_1-\vec{r}_2)\times(\vec{k}_1-\vec{k}_2)/2$ is the relative angular momentum operator between nucleons 1 and 2, and $\vec{S} = \vec{s}_1+\vec{s}_2$ is the total two-nucleon spin. The

coefficients $V_{\sigma\tau}^{C}$, etc., depend on the relative coordinate $\vec{r} = \vec{r}_1 - \vec{r}_2$ of the two interacting nucleons, and can be represented by a sum of Yukawa functions

$$V_{12}(r) = \sum_{i=1}^{N} V_i \frac{\exp[\frac{-r}{R_i}]}{\frac{r}{R_i}}.$$

The interaction ranges R_i and interaction strengths V_i are determined from a best fit to the t_F matrix and generally they depend on the incident energy E_{CM}.

The spin operators $\vec{\sigma}_1$, $\vec{\sigma}_2$, $\vec{S}$, or S_{12} produce spin-flip ($S = 1$) transitions in the projectile and in the target, and all terms that involve the isospin operator $\vec{\tau}_1 \cdot \vec{\tau}_2$ induce isospin (T = 1) transitions.

1.1.9 Properties of the free t_F-matrix interaction

The force components in Eq 1.5 are functions of the incident energy E_{p} and the momentum transfer q.

The most prominent feature of the curves in the top part of figure 1.6 is that the central scalar-isoscalar interaction V_o^C dominates the other central spin-, isospin-, and spin-isospin-dependent interaction terms at all energies considered. In the energy region 150 MeV $\leq E_{\mathrm{p}} \leq$ 500 MeV V_o^C becomes relatively weak.

1.1.10 (p,n) reaction as probe of Gamow-Teller strength

In β^- decay a neutron in a nucleus is transformed into a proton. This occurs with very little momentum transfer into the nucleus, which implies that the nuclear excitations are due to a change in intrinsic quantum numbers (spin and isospin) of the nucleon [Goo 83].

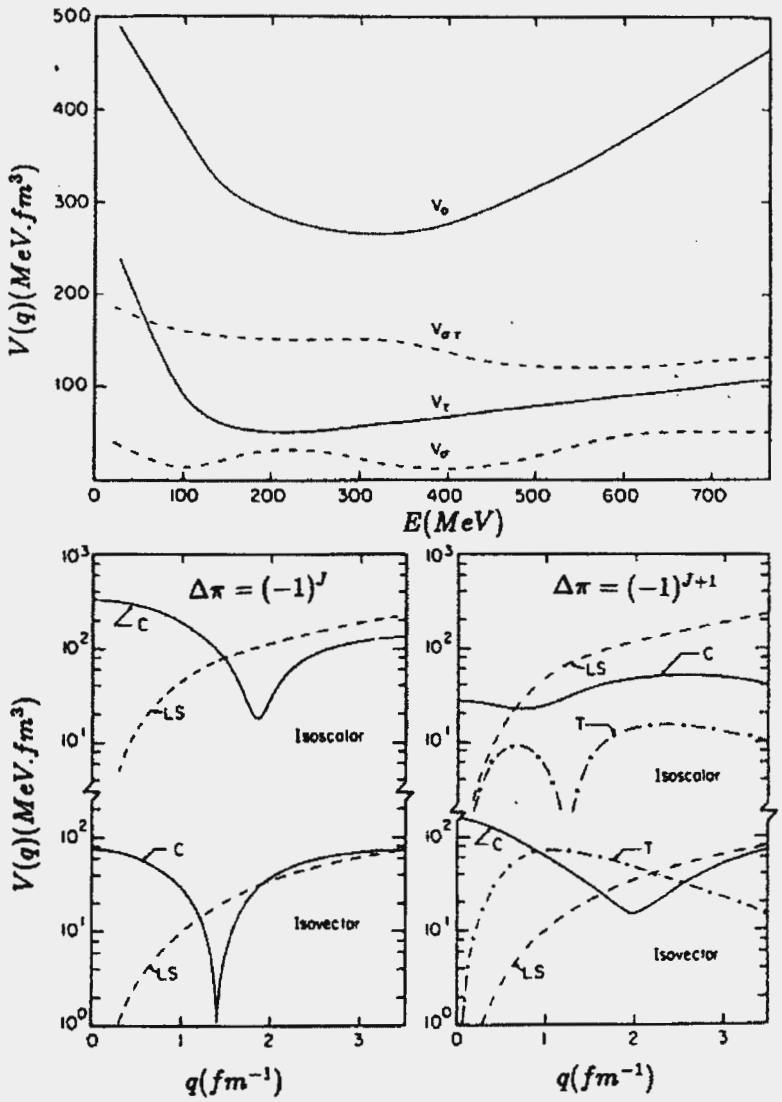

Figure 1.6: *Energy and momentum dependence of the free nucleon-nucleon t_F-matrix. The upper figure shows the energy dependence of the central components of the effective t_F-matrix at zero momentum transfer (including direct and exchange terms). The G-matrix interaction of Bertsch et al. [Ber 78] was used below 100 MeV and joined smoothly to the t_F-matrix above 100 MeV. The lower figures show the momentum dependence of the 135 MeV t_F-matrix for natural (left figure) and unnatural (right figure) parity transitions. Isoscalar and isovector central (C), spin-orbit (LS), and tensor (T) components are shown. From Petrovich and Love [Pet 81].*

To search for the GT strength we need a GT probe that can transform a neutron to a proton or vice versa without changing the orbital angular momentum of the nucleus. The probe should be applicable at high enough energies to reach states of interest.

The (p,n) reaction inserts a proton into the target nucleus and removes a neutron. If performed at intermediate energies and small momentum transfer it induces similar transitions to those in β^- decay. We should be able to establish a relationship between the (p,n) 0° cross sections and the GT strength.

1.1.11 The cross section

In the distorted-wave approximation [Sat 64] the differential cross section is given by [Goo 80]

$$\begin{aligned} \frac{d\sigma}{d\Omega} &= \left(\frac{\mu}{2\pi\hbar^2}\right)\frac{k_f}{k_i}\frac{1}{(2J_i+1)(2s_p+1)} \\ &\times \sum |\chi_f^{(-)*}(r_p) < f|\sum_f v_{jp}(1-P_{jp})|i > \chi_i^{(+)}(r_p)d^3r_p|^2 \end{aligned} \quad (1.6)$$

where:

- μ is the reduced energy divided by c^2;
- k is the wave number;
- χ's are distorted waves;
- $< f|\sum_f v_{jp}(1-P_{jp})|i >$ is the target matrix element;
- v_{jp} is the effective nucleon-nucleon interaction;
- P_{jp} is the permutation operator accounting for knockout exchange; and

- the sum is over initial and final spin projections of the projectile and target.

The impulse approximation [Ker 59] is also reasonable for beam energies higher than 100 MeV, so that v_{jp} is expected to be close to the free nucleon-nucleon t-matrix.

The (p,n) reaction selects the isovector parts of the v_{jp}, and for 0° scattering, only the low-momentum components contribute appreciably to the transition amplitude. The central parts of the isovector effective interaction dominate at low q and non-central parts can be neglected [Pet 79] [Lov 80] [Pet 80a] [Pet 80b]. With this simplification the distorted-wave born approximation 0° cross section for (p,n) transitions with appreciable Fermi and/or Gamow-Teller strength can be described by [Pet 79] [Pet 80a] [Pet 80b] [Goo 83]

$$\frac{d\sigma}{d\Omega} = \left(\frac{\mu}{\pi\hbar^2}\right)\frac{k_f}{k_i}\left[N_\tau^D|J_\tau|^2 B(F) + N_{\sigma\tau}^D|J_{\sigma\tau}|^2 B(GT)\right] \tag{1.7}$$

where J_τ and $J_{\sigma\tau}$ are magnitudes of the volume integrals of $q = 0$ components of the effective spin-independent $(\tau_1 \cdot \tau_2)$ and the effective spin dependent $(\sigma_1 \cdot \sigma_2 \tau_1 \cdot \tau_2)$ isovector central terms in $v_{jp}(1 - P_{jp})$, N_τ and $\mathrm{N}_{\sigma\tau}$ are distortion factors calculated by Love et al., and q is the three-momentum transfer.

1.1.12 Gamow-Teller strength

The calculation of the strength of different peaks in the (p,n) spectrum is done by calibrating the cross section for the GT transitions to the cross section for the Fermi transition. The Fermi strength $B(F)$ which is concentrated in the IAS has the value $B(F) = N - Z$.

At low momentum transfers, the noncentral parts of the effective interaction become small; therefore, in the distorted-wave impulse-approximation, the

(p,n) cross section at the minimum kinematically allowed momentum transfer $q = \omega = 0$ can be written [Goo 80] [Tad 87].

$$\sigma_F(q,\omega) = K(E_p,\omega)N_\tau|J_\tau|^2B(F) \tag{1.8}$$

and

$$\sigma_{GT}(q,\omega) = K(E_p,\omega)N_{\sigma\tau}|J_{\sigma\tau}|^2B(GT) \tag{1.9}$$

In even-A targets the transition to the IAS is pure Fermi, and the ratio of the cross sections is

$$\frac{\sigma_{GT}(q,\omega)}{\sigma_F(q,\omega)} = \frac{K_{GT}(E_p,\omega)}{K_F(E_p,\omega)}\frac{N_{\sigma\tau}|J_{\sigma\tau}|^2}{N_\tau|J_\tau|^2}\frac{B(GT)}{B(F)} \tag{1.10}$$

The factor $F(q,\omega)$ accounts for the non-zero momentum (q) and energy (ω) transfer of the (p,n) reaction and is used to extrapolate the cross section to $q = \omega = 0$. $F(q,\omega)$ approaches unity as (q,ω) approaches (0,0). the extrapolated cross section is then

$$\sigma(0,0) = \frac{\sigma(q,\omega)}{F(q,\omega)}$$

Then

$$\frac{\sigma_{GT}(0,0)}{\sigma_F(0,0)} = \frac{K_{GT}(E_p,\omega)}{K_F(E_p,\omega)}\frac{N_{\sigma\tau}|J_{\sigma\tau}|^2}{N_\tau|J_\tau|^2}\frac{B(GT)}{B(F)}$$

and

$$\frac{\sigma_{GT}(0,0)}{\sigma_F(0,0)} = R(E_p,A)^2\frac{B(GT)}{B(F)}$$

Taddeucci et al. [Tad 81] [Tad 87] determined the following relationship: For even-mass nuclei

$$R(E_p, A) = \frac{E_p}{E_o} \tag{1.11}$$

where

- E_p is the proton beam energy, and
- $E_o = 55.0 \pm 0.4 MeV$.

Hence

$$B(GT) = \frac{B(F)}{R(E_p, A)^2} \frac{\sigma_{GT}(0,0)}{\sigma_F(0,0)} \tag{1.12}$$

1.2 Aims and objectives of present study

Theoretical studies have suggested different models to explain the quenching of GT strength. These include: the spreading of the strength from giant Gamow-Teller resonance to higher excitation energies due to the influence of the tensor force [Tak 74], the Δ resonance [Ost 85], meson-exchange currents [Tow 83], or ground-state correlations [Gro 83]. A number of studies [Gaa 81] [Fla 89] [Mad 89] were undertaken of the quenching of GT strength on even-mass targets. A few of these studies [Gaa 81] [Wat 85] were done on odd-mass targets of which most of them were light nuclei.

The ^{208}Pb(p,n)^{208}Bi reaction was studied by Horen et al. [Hor 80] in 1980 at E_p = 120 MeV and 160 MeV. The energy resolution was not good enough to study the GT strength in the discrete states. They concentrated on the search for IAS of M1 states and giant spin-flip resonances.

In 1981 Gaarde et al. [Gaa 81] studied the ^{208}Pb(p,n)^{208}Bi reaction at a proton energy of 200 MeV. The low-lying states were not resolved at this energy, and they studied spin-isospin multipole vibrations.

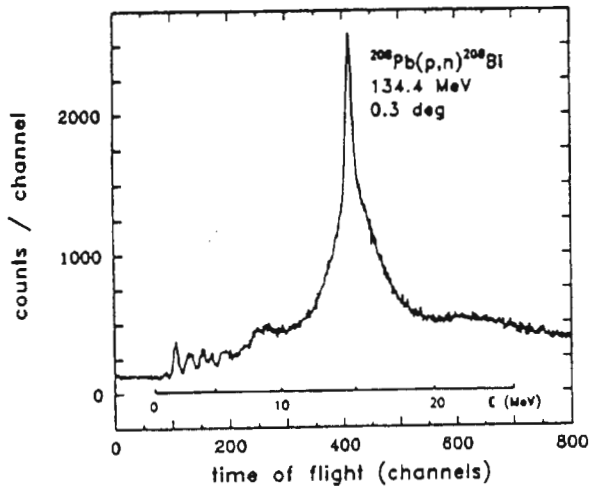

Figure 1.7: *Neutron time-of-flight spectrum at* $\Theta_{\mathrm{Lab}} = 0.3°$ *associated with the* ^{208}Pb(p,n)^{208}Bi *reaction at 134.3 MeV.(Flanders et al. [Fla 89]).*

Flanders et al. [Fla 89] studied GT strength in the ^{208}Pb(p,n)^{208}Bi reaction at 134.3 MeV for excitation energies up to 38 MeV. A polynomial background and hyper-Gaussians were fitted to the time-of-flight spectra. The GT strength was extracted by normalizing the GT strength of the 1^+ states to the Fermi transition. The GT strength observed in 1^+ peaks was 56% of the $3(N-Z)$ sum rule, with 45% from the GTGR and 10% from structures below the GTGR.

The motivation for the present study is that

(a) the total B(GT) extracted as shown in figure 1.8 is 40% less than the value predicted by the independent sum rule.

(b) there is an ambiguity in the comparison of B(GT) in odd- and even-mass nuclei due to the scarcity of odd-A data in the heavy nuclei region between 165 and 205.

The Gamow-Teller strength of a given transition can be measured in to possible ways. One can measure the cross section and then obtain the

proportionality constant $\hat{\sigma}_{GT} = \sigma_{GT}/B(GT)$ from DWIA calculation or from a known Gamow-Teller transition in the same target. Another approach, is to use the IAS as the calibration transition provided the proportionality ratio $\hat{\sigma}_{GT}/\hat{\sigma}_F$ is known. In the study of some light odd-mass targets it has been observed that some anomalies exist: if the cross proportionality ratio is the same as for the even-A case, then the GT and F proportionality constants must both be larger than either DWIA calculations or even-A data would allow. If instead one assumes that the GT proportionality constant must be similar to that for even-A nuclides, then the Fermi proportionality constant $\hat{\sigma}_F$ must be smaller than expected. This is the ambiguity associated with odd-A targets. It is important to address and attempt to resolve this ambiguity for the following reason: several GT transitions of interest to neutrino physics, notably in ^{127}I, occur in odd-A nuclides. If accurate GT transition strengths are to be determined for these cases, the origin or magnitude of the "even-odd ambiguity" must be understood.

The present data can be applied to "odd-even" problem in the following way: ^{181}Ta is an odd-A nuclide and ^{208}Pb is an even-A nuclide. Measuring cross sections for both targets at the same time under the same experimental conditions removes or minimizes potential systematic error with respect to their relative normalizations. The cross section spectra for each spectra can then be analyzed in the same way, and the resultant GT and F strengths compared. Assuming that the spreading or quenching mechanism for the total GT stregth should be approximately the same in each case, one would expect to obtain similar results for the fraction of total GT proportionality or GT/F cross proportionality factor, this should reveal itself by yielding a much different fraction for the apparent GT strength observed. In this case, caution would be advised in the analyses of the (p,n) data applied to the

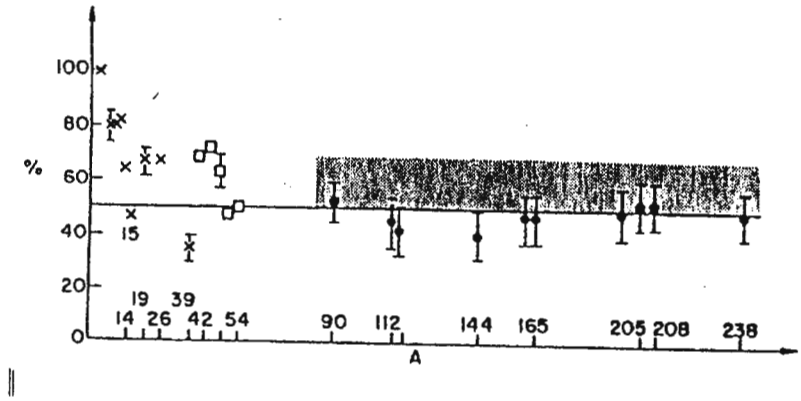

Figure 1.8: *Fraction(%) of the Gamow-Teller sum rule strength observed in* (p,n) *reactions on different targets. For the heavier targets the full points represent the strength concentrated in the peaks, whereas the shaded area also includes the strength under the collective states. From [Gaa 85].* A *denotes target mass.*

neutrino targets.

Chapter 2

Experimental Work

2.1 Overview

The (p,n) experiment requires detection of neutrons. The main problem in detecting neutrons is that they are electrically neutral. Therefore one cannot use the standard methods for detecting charged particles. Instead one must resort to a technique involving the interaction of the neutron with a nucleus, and the detection of secondary charged particles at the energies of interest. This usually involves the scattering of neutrons from hydrogen nuclei and detection of the recoil protons. Because of the detection of charged particles from a secondary scattering reaction sensitivity is greatly reduced, and unique energy information of the neutron is lost.

The method employed in this experiment is the time-of-flight technique [Alv 38], developed by Goodman et al. [Goo 79] for (p,n) reactions at intermediate energies. The disadvantage of this method is that it needs a long flight-path to achieve good time resolution. The long flight path results in a small detection solid angle and a low count rate in the detectors. The two major considerations when designing a neutron time-of-flight detector system

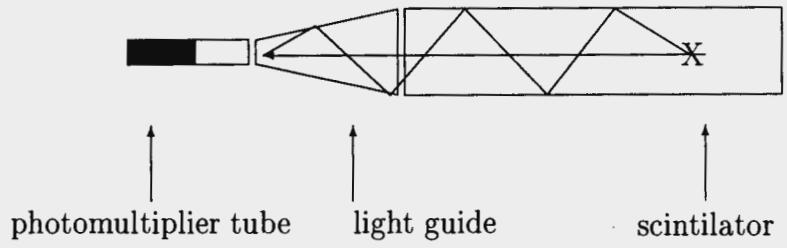

Figure 2.1: *Two different light rays from one point marked by an X in the scintillator follow different paths with different arrival times.*

are count rate(efficiency) and time(energy) resolution. The sub-nanosecond is required so that $\Delta E \approx 0.3$ MeV can be achieved.

To compensate for the low count rate one needs large volume detectors. However increasing the volume of the detector degrades the time resolution, since the time resolution of detectors depends on light collection time and this is a geometrical effect as illustrated in figure 2.1.

Consider a neutron interaction at a certain point in the scintillator. This scintillation can reach the phototube undeflected or after a number of reflections on the sides of the scintillator. The former path of scintillation will result in a narrow distribution and the latter will produce a broad distribution with the centroids of the distributions coinciding with each other.

2.2 Experimental arrangement

2.2.1 Beam

The experiment was performed using the beam swinger neutron time-of-flight facility at the National Accelerator Centre (NAC), Faure, near Cape Town. Figure 2.2 shows the layout of the cyclotrons and beam lines at the NAC. The beam swinger facility is located at the end of the N beam-line.

The proton beam was created in two stages. In the first stage the ion source of the solid pole injector cyclotron (SPC1) produced unpolarized light ions and SPC1 accelerated protons to a maximum energy of 5.316 MeV. In the second stage protons that have attained maximum energy were injected into the first orbit of the separated sector cyclotron (SSC) where they were accelerated to an energy of 122 MeV. The interval between beam pulses was 282 ns since a pulse selection of one in six bursts was used.

The time structure of the beam was measured by looking at the elastically scattered protons detected in a fast scintillator telescope consisting of ΔE and E detectors. This system was located at 30° with respect to the undeflected incident proton beam (see figure 2.5).

2.2.2 Targets

The targets were, a self supporting ^{208}Pb foil enriched to 98.8% with an areal density of 61.0 mg.cm^{-2}, natural Ta (99.99% ^{181}Ta) with an areal density of 41.2 mg.cm^{-2} and natural Li (92.5% ^{7}Li) with an areal density of 51.4 mg.cm^{-2}. The Li target was sandwiched between two 2.075 mg.cm^{-2} of Havar foils to prevent chemical degradation of the target. A lithium target with a piece of polythene attached was used under identical experimental conditions to determine the flight-path, time offset t_0, and thus calibrate the time-of-flight in terms of excitation energy, as described in section 3.1.3.

2.2.3 Flight-path

Neutrons destined to reach the neutron detectors had to pass through a narrow collimator (with dimensions of approximately 6.0 m × 0.1 m × 0.1 m) in the shield wall of the beam swinger area. The twelve neutron detectors were located parallel to the 0° line at a distance of 100.0 m from the

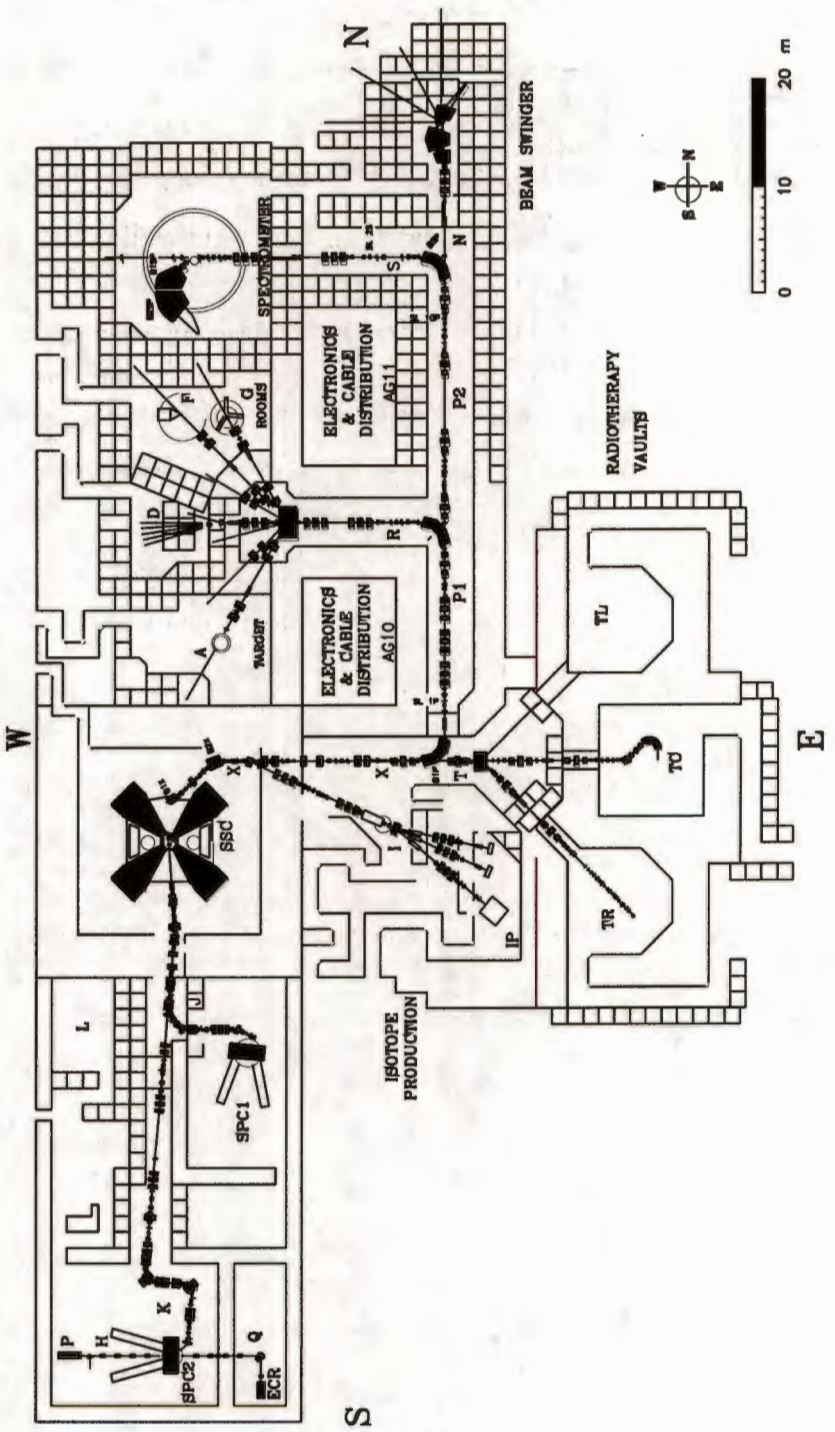

Figure 2.2: *The layout of the NAC cyclotron.*

target. The orientation of three stacks of four detectors is shown in figure 2.3. Measurements were made at four different laboratory angles, Θ_{Lab}, namely 0°, 2°, 4°, and 10°. These angles were reached by using the beam swinger to change the angle with which the beam hits the target.

2.2.4 The detectors

The detector system consisting of twelve neutron counters and the ΔE–E proton telescope are described in more detail below.

2.2.5 The neutron counters

The design of a neutron counter is shown in figure 2.4. Each of the twelve counters consisted of a 60 cm × 10 cm × 10 cm rectangular bar of NE 102A scintillator, two conical perspex light guides (one on each end of the counter), and the two Hamamatsu R329 photomultiplier tubes mounted on the light guides. The photomultiplier tubes, which were used in conjuction with E931 bases, were sheathed in μ–metal cylinders to provide magnetic shielding. Adjacent optical surfaces were glued with Silgaurel gel RTV-ME 600/601. The scintillators were covered with white paper to improve the efficiency of light collection. The system was kept in an aluminium casing covered with black plastic to make it light-tight. Springs in the aluminium casing were used to maintain optical contact. The intrinsic time resolution of the detectors of 0.3 to 0.8 ns was achieved. The high voltage for each photomultiplier tube was set between −1500 and −2000 V.

2.2.6 The ΔE–E proton telescope

The telescope comprised of two types of detectors (see figure 2.5).

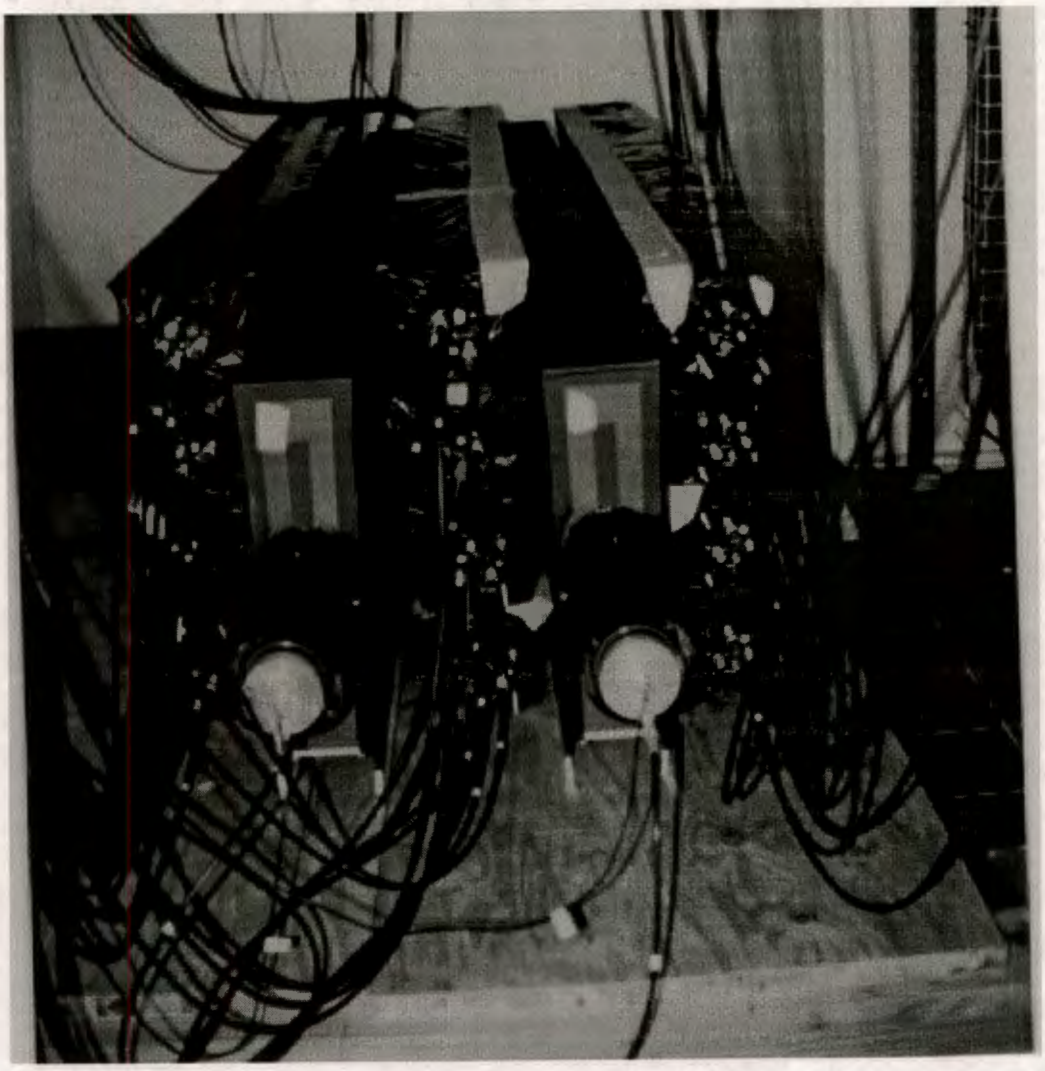

Figure 2.3: *The orientation of the three stacks of four detectors with two veto counters between the stacks facing the beam.*

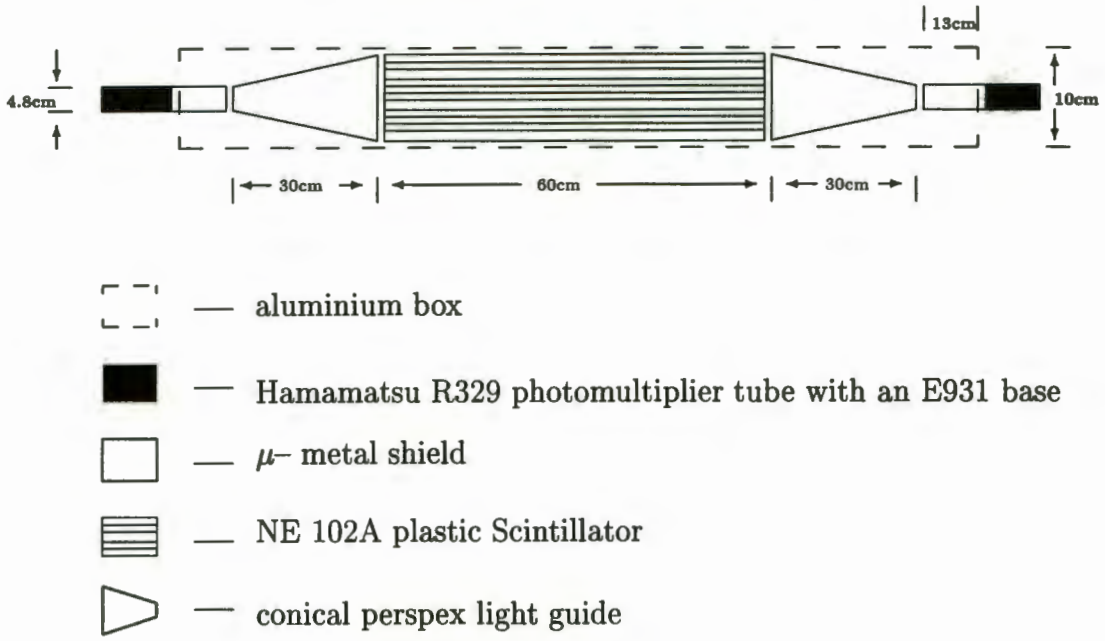

Figure 2.4: *A schematic representation of a neutron detector design.*

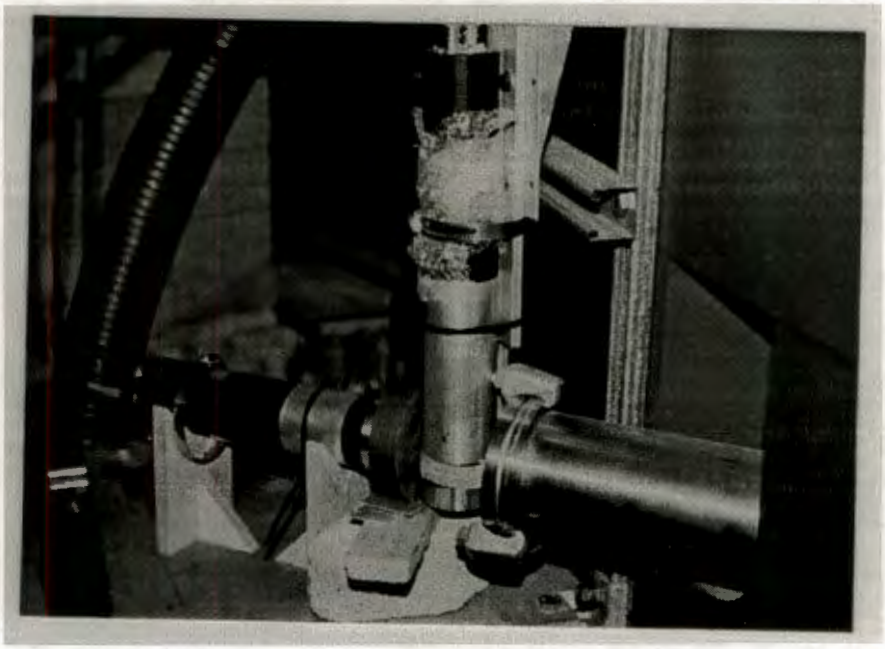

Figure 2.5: *The arrangement of the ΔE-E telescope in the beam-swinger vault shown with a copper degrader between the two detectors. The copper degrader was not used in these experiments. The telescope was positioned at 30° with respect to the beam-line.*

The ΔE detector consisted of a small, circular NE 102A plastic scintillator glued to a light guide and mounted on a Hamamatsu H2431 photomultiplier tube. This detector was mounted in a cylindrical aluminium tube. The high voltage was set at −2750 V. The E detector consisted of a 10 cm thick cylindrical NE 102A plastic scintillator, a light guide, and a Hamamatsu H2431 photomultiplier tube. High voltage was set at −1300 V.

2.3 The electronics

The electronic circuit diagram is divided by function into four sections (figures 2.6 to 2.10). A further figure, figure 2.11 shows the electronics used to

measure the beam resolution. These diagrams show only one detector for simplicity.

2.3.1 Time-of-flight measurement

A schematic representation of the electronic circuit used to measure the time-of-flight is shown in figure 2.6. Negative high voltages were applied to the detectors supplied by a North Electronics Systems (N.E.S.) HV unit which was controlled by the VAX over a RS-232 data line. The anode signals from the photomultiplier tubes on each end of the detector were transfered via 50 Ω coaxial cable. An EDA36 50Ω 6dB splitter was used split the signal into two signals in order to send timing signals and pulse height signals through separate electronic channels. One anode signal was fed to an Ortec 934 constant fraction discriminator (CFD) with a threshold set below the 20 MeV deposited by a minimum ionizing cosmic ray muon going through 10cm of plastic scintillator. These two discriminated pulses from each end of the counter went into a LeCroy 624 octal meantimer (MT) where the mean-time associated with a cosmic event was derived. All anode signals from the twelve counters went through similar circuits. The outputs from the four detectors in each of the three stacks were used to obtain a 4-fold coincidence to select cosmics that went through that stack. The output from each stack was fed into a LeCroy 365AL 4-fold logic unit set on coincidence of level 1 in order to generate a cosmic trigger. This trigger occurred if and only if all four counters in one of the three stacks fired within 20 ns of one another.

To generate the neutron trigger the two second anode signals from the splitter at each end of the counter were passively summed in the Phillips 744 fan-in/fan-out(FIFO). The output from this FIFO were fed to a Phillips 711 six-channel discriminator. This discriminator had a threshold set corresponding

to a neutron energy of about 60 MeV (for E_p = 122 MeV) in order to cut out the low energy signals and wrap-around[1]. Its sum output was fanned out to a LeCroy 365AL logic unit(logic unit) to provide a NIM neutron trigger. This output occurred whenever the counter recorded a pulse height above the 60 MeV threshold.

The cosmic and neutron triggers went into a logic unit, the output of which fed into a LeCroy 821 quad disc(quad disc) to form the TDC start. Two further outputs of the quad disc were utilised. One of the outputs was delayed to provide the strobe and the other to form two LeCroy 2249A analog-to-digital conveter(ADC) gates. The other output was fed into a Phillips 711 discriminator to form the event trigger for the event trigger module (ETM). Upon receiving the trigger, the ETM set a busy flag and waited a preset time before it initiated the read-out cycle. The time was set in an Ortec 719 timer which was linked to the ETM via a LeCroy 688A level adapter. The level adapter converted the TTL input to NIM output. Since the Li target was thicker than the Pb and Ta targets, a faster read-out cycle was required for the former target, to monitor the beam time and fine tuning of the electronics. The timer was set at 1 Hz for lithium runs and 10 Hz for lead and tantalum runs.

The outputs from the twenty-four CFDs were delayed, before serving as the stops for the LeCroy 2228A time-to-digital converters(TDC). The four TDCs were started by the four TDC starts. The VAX 11/750 data acquisition computer was interfaced to the CAMAC crates through a BiRa Microprogrammable Branch Driver (MBD) or VME system. The VAX 11/750 read the digitized times of the stops relative to the start which allowed the time-of-flight spectra to be generated, via the MBD/VME system.

[1]Described in section 3.1.3

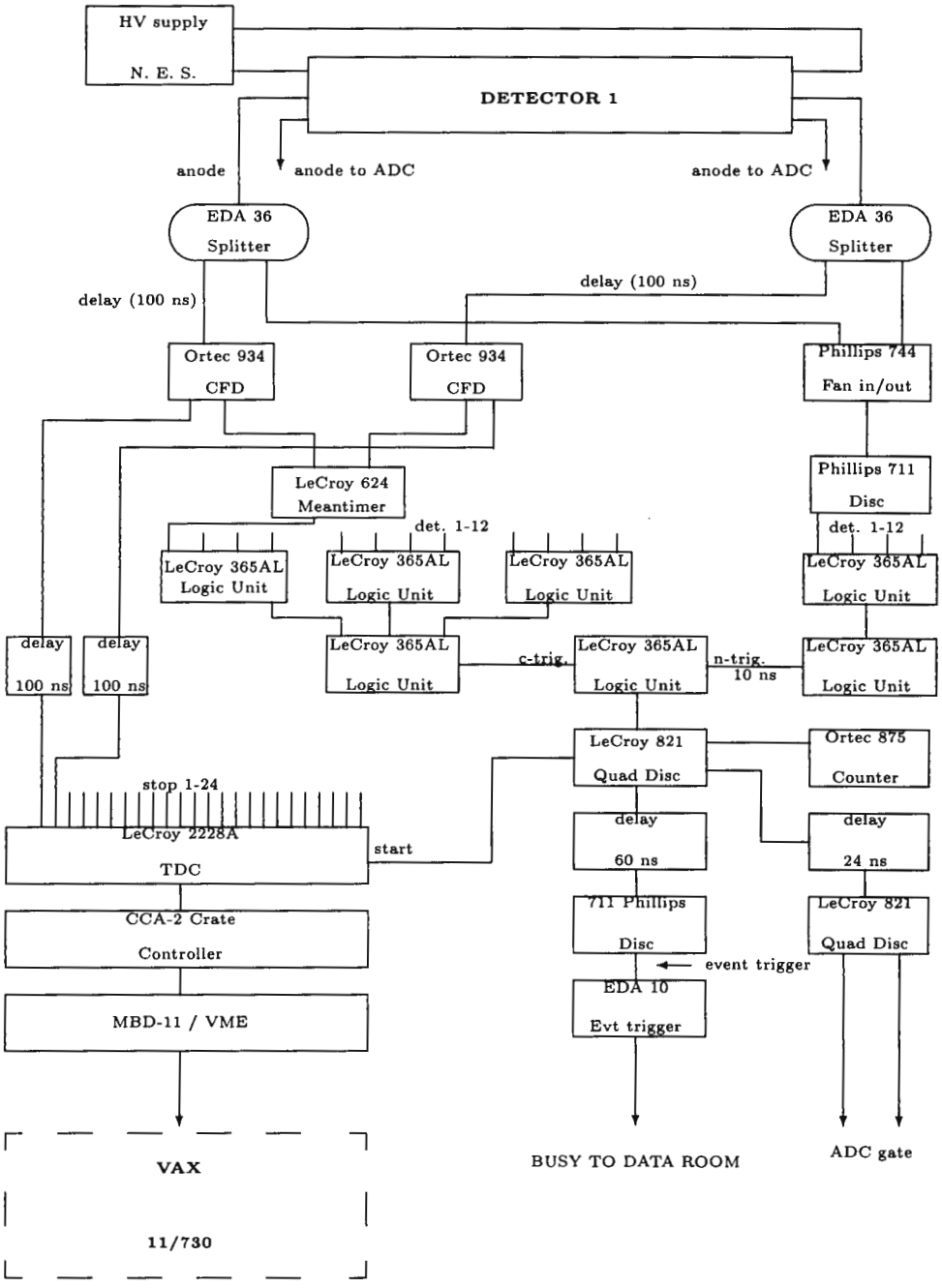

Figure 2.6: *A schematic representation of the electronics used to measure the neutron time-of-flight.*

2.3.2 Pattern register

The electronic circuit in figure 2.7 gives information about the event detected, namely, whether it is a cosmic or a neutron event, in which stack the event occurred and which detector fired. The anode signal from each phototube was split by the 50Ω 6dB splitter into identical signals to derive the cosmic bit, the neutron bit, and the bit for each counter which registered an event. One signal was discriminated in the CFD whose output was combined with similar output from the other end of the counter and fed into the MT. The pulse from the MT was stretched to 10 μs by a logic stretcher. This output was registered in channel 1 of the BiRa NIM Register corresponding to counter number one. Similarly, outputs from counters two to twelve were registered in channels 2 to 12 respectively.

The cosmic and neutron triggers for each stack (section 2.3.1) set three cosmic bits and three neutron bits respectively. When an event occurred the strobe instructed the pattern register module to latch the pattern. (The strobe was described earlier in section 2.3.1.). The register module which provided the pattern for the counters was read as part of each event by the VAX 11/750 computer via the MBD/VME system.

2.3.3 Pulse heights

The electronic circuit in figure 2.8 was used to acquire pulse height data associated with neutrons detected by one of the stacks. The first twelve anode signals from each end of the first six counters were delayed by 320 ns (cable delay) and the remaining anode signals were delayed by 200 ns (cable delay). The two types of delay cables were used because of the availability of delay cables. The ADC gate was adjusted to accommodate for these two

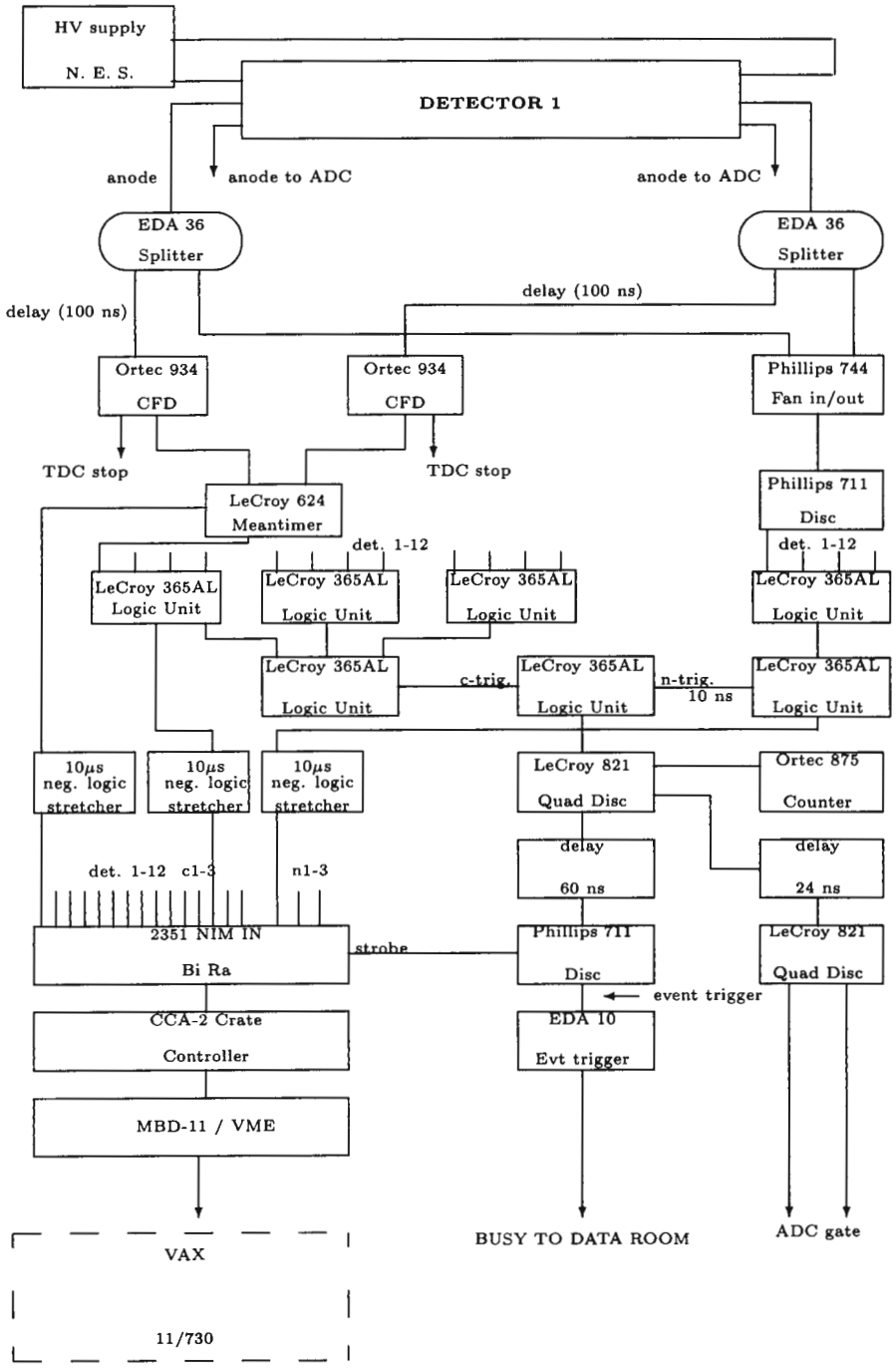

Figure 2.7: *A schematic representation of the electronics used to determine the bit counter pattern.*

types of delays. (The ADC gate was described earlier in section 2.3.1.). Each signal was fed via a 50 Ω attenuator before being input to the LeCroy 2249A analog-to-digital converter (ADC). The CAMAC ADC was read by the VAX 11/750 computer via the MBD/VME system.

2.3.4 Measurement of integrated beam current

The beam swinger is composed of three dipole magnets, (see figure 2.9.) two bending magnets and one beam-dump magnet. The first circular-pole magnet (B1N) deflects the beam away from the beam line. The second magnet (B2N) is a contoured wedge magnet which bends the beam back to the beam line and focuses the beam on the target. The angle of incidence can be varied over a range of about 30° by varying the amount of bend. The third magnet (B3N) swings the charged particles that exit from the target away from the 0° flight path, and focuses them onto a Faraday cup situated in the beam dump. The Faraday cup is connected to a current integration unit (Brookhaven Instrument Corporation model 1000C) via a Faraday cup relay interface (EDA 14-2). Current integrator settings were read by the data acquisition computer via a current integrator interface (EDA 14-3).

The electronic circuit used to measure the integrated current is shown in figure 2.10. The signal from the current integration unit was discriminated in a Ortec 436 100 MHz discriminator to provide a fast logic pulse. Its output was fed into a LeCroy 365AL logic unit since this module can accept veto input. The veto was generated by a busy signal (established by the event trigger modules described in section 2.3.1) either from the dataroom or from the hut. The output(which contained the charge information) was counted in a LeCroy 2551 scaler.

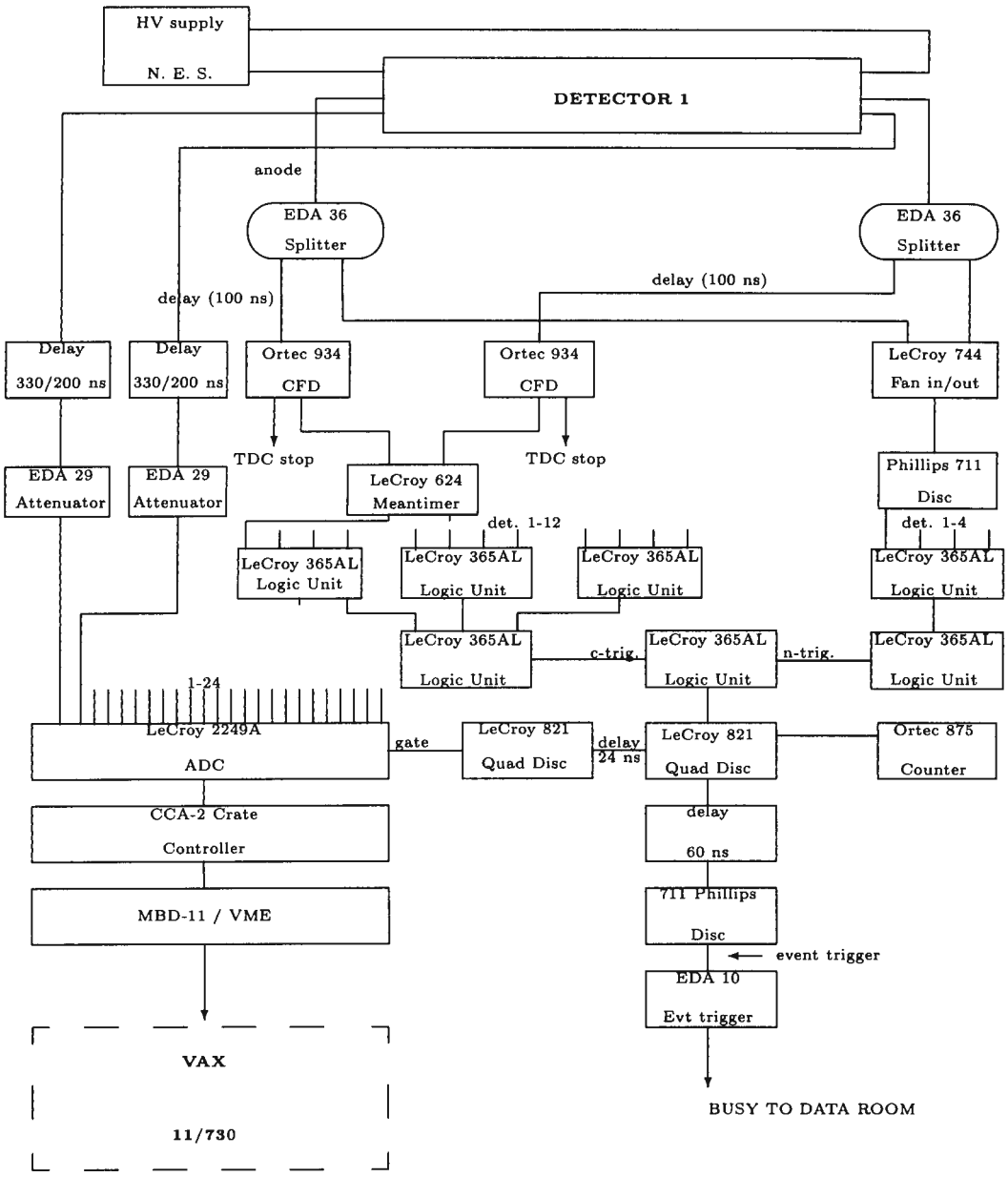

Figure 2.8: *A schematic representation of the electronics used to measure the neutron pulse heights.*

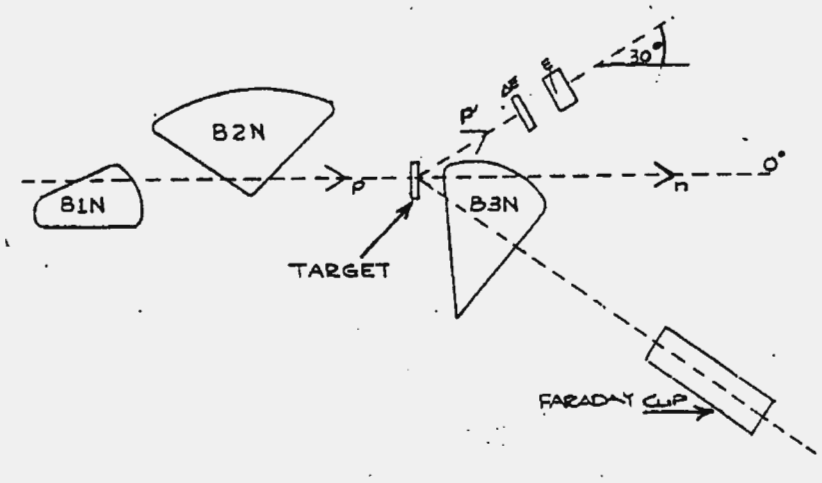

Figure 2.9: *A schematic diagram of the three dipole magnets, target position, proton telescope and the Faraday cup.*

An Ortec 719 timer was set to produce pulses at a rate of 1 Hz. These pulses were counted by an Ortec 875 counter and also by a LeCroy 2551 scaler. The timer pulses were also fed to a logic unit, vetoed by the busy signal, to give the number of pulses that went through when the event trigger (VAX 11/750) was alive. This second output was also read by a counter and scaler. The two scalers were used to estimate the fraction of events lost due to computer dead time, and were read by the VAX 11/750 computer via the MBD/VME system.

2.3.5 Beam time resolution

A fast plastic-scintillator telescope detecting elastic scattered protons of the target was used to measure the width of the beam pulse, which gives a measure of the beam time resolution. The FWHM of the proton bunch was 250 ps in most runs. Runs with very low resolution were discarded and in some cases the operators were asked to retune the beam.

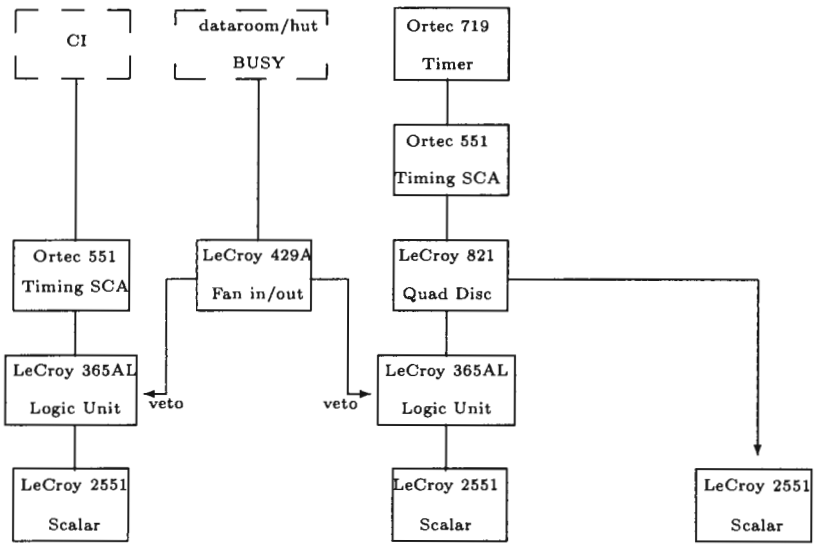

Figure 2.10: *A schematic representation of the electronics used to measure the integrated current.*

The electronic circuit used is shown in figure 2.11. These scattered protons deposited some of their energy in the ΔE detector before they stopped in the E detector. High voltages of −2.7 kV and −1.2 kV were supplied to the ΔE and E photomultiplier tubes respectively via Ortec 556 high voltage supplies. The pulse from the E phototube was split by a 50 Ω splitter. One pulse fed a fast 300 MHz oscilloscope for visual inspection. The other pulse was fed into the Ortec 584 CFD whose lower threshold was set to select only the highest energy protons, i.e. the elastically scattered ones, which formed the brightest band on the oscilloscope. The output was discriminated in a Quad Disc. The oscilloscope was triggered on this E pulse, then the position of the ΔE on the oscilloscope was noted.

The pulse from the ΔE photomultiplier tube was split by the splitter to the fast 300 MHz oscilloscope. The other pulse was fed to a Ortec 583 CFD.

Triggering the oscilloscope on the ΔE pulse, the window of the Ortec 583 CFD was set such that the selected ΔE band fell on the position noted above. This output was discriminated by the Quad Disc. The width of this pulse was set and delayed to fit in the discriminated E pulse. The ΔE and E pulses were set in coincidence in the logic unit. The coincidence ensured selection of the elastically scattered protons that went through the telescope. The output was discriminated in a Quad Disc then delayed by 260 ns, after which it was fanned out to a Quad Disc. The output provided the start for an Ortec 567 time-to-amplitude converter (TAC).

The discriminated pulse selected radio frequency (PSRF) (in section 2.3.1) provided stops for the TAC. The times of the stops relative to the starts were converted to amplitude in the TAC. The analog amplitude signals were digitized in a Canberra 8077 fast ADC. The ADC was read by the VAX 11/750 computer via the MBD/VME system. This provided the beam measurement of the beam-time resolution.

2.4 Data acquisition

Data were acquired over four weekends in March and May 1996. During the first two weekends the VAX was interfaced to the CAMAC crates through an MBD. The on-line analysis software limited the event rate during the first two weekends, so a lower beam current of 100 nA had to be used.

Data were acquired using the XSYS software on the NAC VAX 11/750 computer. The software was divided into the Data Acquisition Program(DAP) and the Event Analysis Language (EVAL) sorting algorithm. The DAP file

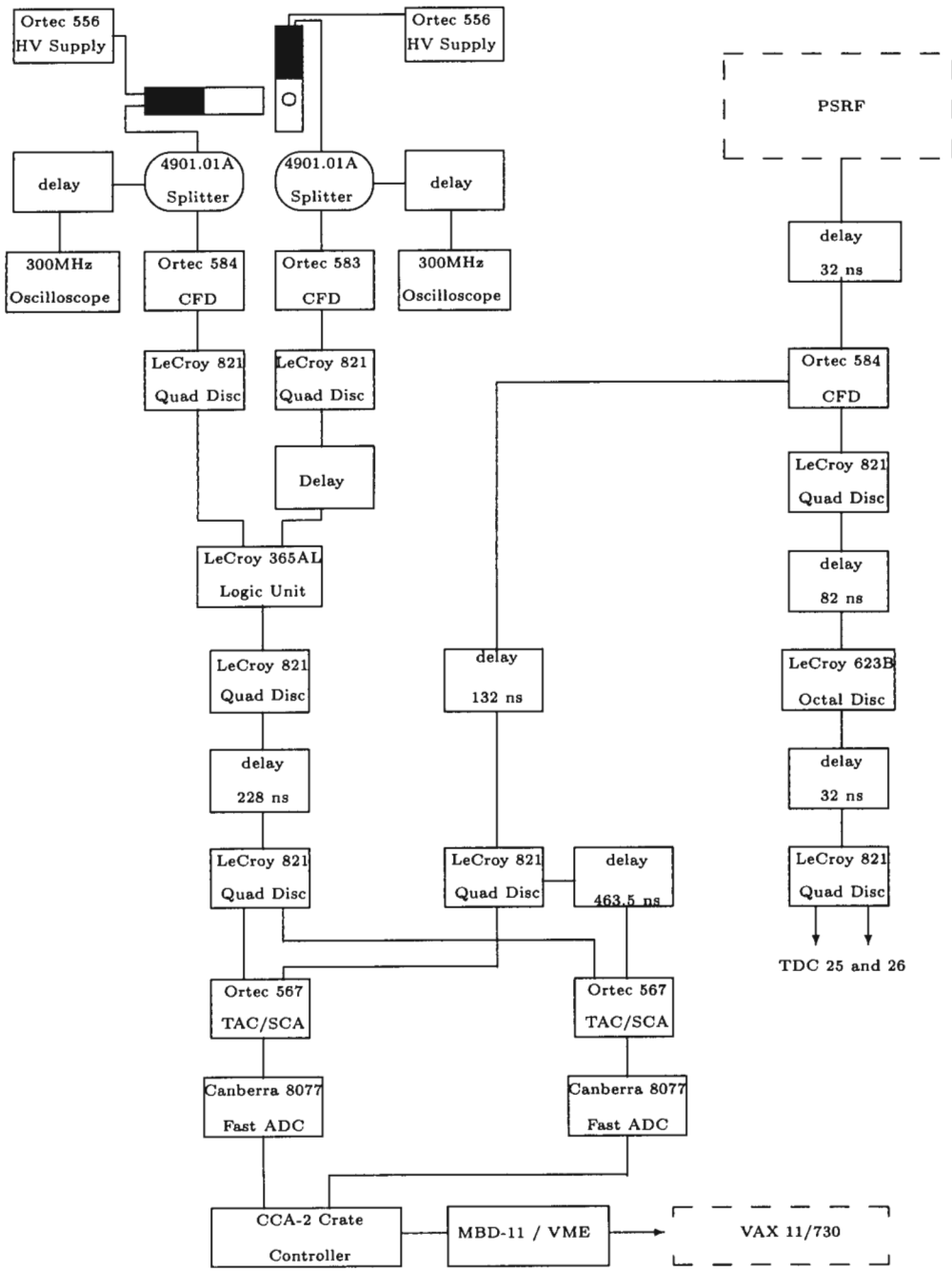

Figure 2.11: *A schematic representation of the electronics used to measure beam time-resolution.*

contained the list of instructions that were loaded into the MBD[2]. This file controlled the CAMAC crates and read event data from the interfaces in the crates. The EVAL program running in the VAX data acquisition computer controlled the incrementing of the histograms.

During the last two weekends a VAXstation was interfaced to the CAMAC crates through a VME system. Since the VAXstation could handle higher data rates, the current was increased to 300 nA to achieve data rates around 2000 events/s. Data were acquired for about 2 hours on each of Pb and Ta targets, and for about 10 minutes on the Li target.

Event data files were written directly onto a 4Gbyte hard disk, and were transferred to 4 mm DAT tapes at the end of the weekend, for offline analysis.

At the beginning and the end of the weekend two types of cosmic runs were acquired; cosmic4441 and cosmic1113. Cosmic4441 means vertical muons fired each detector in one of the stacks. These were used to balance the gains. Cosmic1113 means horizontal muons fire at least one detector in each stack. Cosmic1113 runs could be used to calculate the offsets between the twelve detectors and hence align the TOF neutron spectra. Cosmic4441 were also collected throughout the runs for online gain monitoring.

Each Pb or Ta run was sandwiched between Li runs, since the data from the Li runs were used later for neutron efficiency determination.

[2]The MBD was later replaced by a VME system, the DAP was replaced by subroutines written in *C* language, and the VAX 11/750 by a VAXstation 4000.

2.5 Calibration procedure

2.5.1 Detector gain balancing

The gains of the twelve detectors were balanced by monitoring the pulse height deposited by vertical muons which go downwards through the four detectors in a stack and horizontal muons which go horizontally through three detectors; one in each stack. The energy deposition dE/dx in each detector if muons traverse the full breadth is the same for all detectors and the average enrgy loss of the muons is 2.2 MeV/cm. Hence cosmic rays are useful in calibrating the pulse height spectra and for gain balancing.

Gain balancing between detectors is done by comparing responses of individual detectors to cosmic rays going through the stack. The energy deposited in each detector is about 22 MeV for vertical and horizontal cosmic rays muons.

The overall gain balance was achieved by aligning the geometric mean of the pulse heights to lie in channel 45 for all detectors. The required overall detector gain changes can be made by changing the high voltage applied to the phototube base.

An example of the pulse-height spectra of cosmics that went through one of the three stacks of detectors is shown in figure 2.12. The pulse-heights are lined up with their front edges at approximately channel 45 corresponding to 22 MeV. The low energy tails in the top and bottom spectra are associated with those cosmic rays that only went through part of the top and bottom detectors as shown in figure 2.13. Similar tails were not seen in the middle detectors because in order to trigger all detectors within a plane the muons had to pass through their full thickness.

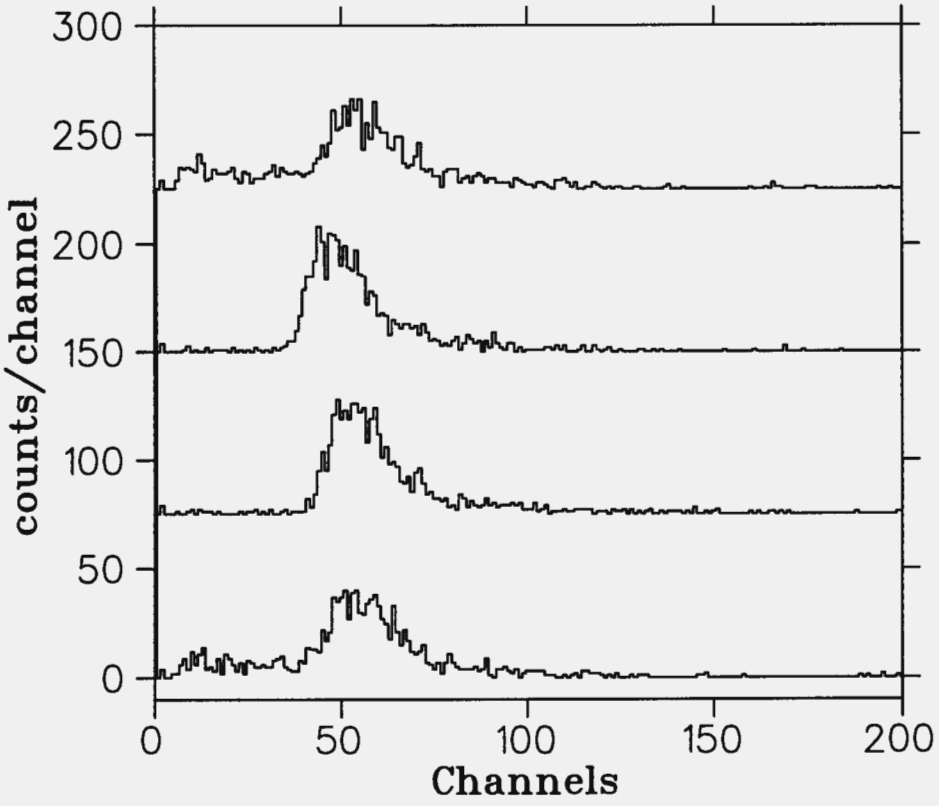

Figure 2.12: *Pulse height spectra associated with a cosmic rays that went through one stack of neutron detectors. Each spectrum is displaced vertically from the previous one by 75 counts/channel for purpose of clarity.*

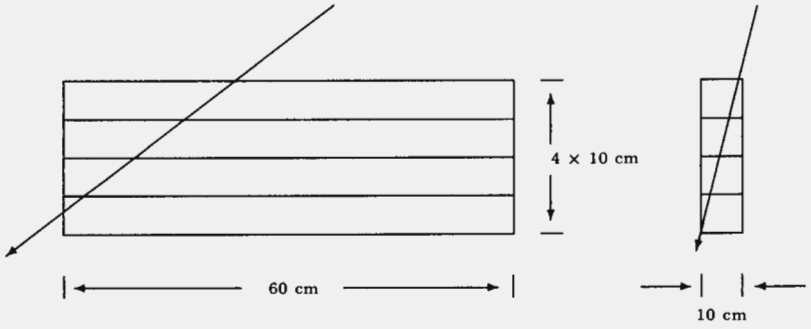

Figure 2.13: *A schematic diagram of a muon that went through four detectors, but only partially through the top and bottom detector.*

Chapter 3

Data Reduction and Analysis

In section 3.1.1 it will be explained how neutron time-of-flight (TOF) spectra were generated and summed into a single spectrum.
The background due to wrap-around will be subtracted in section 3.1.2. The TOF spectra will be calibrated and transformed into excitation energy spectra in section 3.1.6. The TOF spectra will be modelled with lineshapes to determine the yield, cross section and Gamow-Teller strength $B(GT)$ of transitions to different "states". In conclusion the extracted $B(GT)$ will be compared with the sum rule prediction and data available in literature.

3.1 Data analysis

The data recorded on the 4 mm DAT tapes were read using the tape drives linked to the VAX. Data were unpacked and sorted event-by-event using the XSYS [Gou 81] [Gou 83] [Pil 88] [Pil 88] EVAL code.
The flight time of the neutron from the target to the detector was reconstructed. Events with pulse heights above 75 channel (corresponding to 1.5 times the pulse height deposited by a minimum ionizing cosmic ray traversing

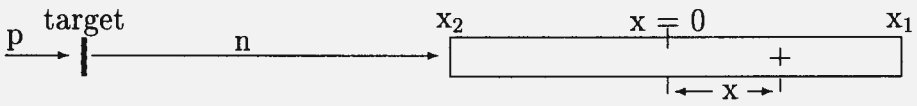

Figure 3.1: *Single detector showing incoming neutron longitudinally to the detector.*

a detector bar vertically) were selected and their time-of-flight calculated. Occasionally, multiple hits were experienced in the detectors. These were caused by neutrons detected a number of times in the detectors, and the detector with the highest pulse height was selected.

3.1.1 Generation of time-of-flight spectrum

In the present experiment both time signals were recorded for each event in separate TDC channels with respect to an arbitrary common start t_s. The orientation of detectors was longitudinal to the neutron beam as shown in figure 3.1.

A neutron starting its flight from the target at $t = 0$, reached position x in the detector. The time measured in $TDC_i = t_i - t_s$, where i denotes TDC channel from 1 to 24. The time taken by the neutron from the target to the detector as seen by side 2 of the detector is given by

$$t'_2 = (TDC_2 - t_s) - (t_{psrf} - t_s)$$

$$t'_2 = TDC_2 - t_{psrf} = t_x + \frac{1}{2}t_d + \frac{x}{v_{eff}} \tag{3.1}$$

where

- t_x is the time taken by the neutron to reach position x;

- t_d is the time of neutron inside the detector;
- v_{eff} is the effective velocity of neutrons inside the scintillator, and
- t_{psrf} is the time for the pulse selected radio frequency(PSRF).

Similarly the neutron as seen by side 1 of the detector is given by

$$t_1' = (TDC_1 - t_s) - (t_{psrf} - t_s)$$

$$t_1' = TDC_1 - t_{psrf} = t_x + \frac{1}{2}t_d - \frac{x}{v_{eff}}. \tag{3.2}$$

Subtracting equation equation 3.2 from 3.1 gives

$$TDC_2 - TDC_1 = \frac{2x}{v_{eff}} \tag{3.3}$$

$$x = \frac{v_{eff}}{2}(TDC_2 - TDC_1) \tag{3.4}$$

Adding equations 3.1 and 3.2

$$TDC_2 + TDC_1 - 2t_{psrf} = 2t_x + t_d$$
$$t_x = \frac{1}{2}(TDC_2 + TDC_1) - \frac{1}{2}t_d - t_{psrf}$$

If the interaction is calculated from the center of the detector, at position $x = 0$, then the neutron time-of-flight becomes

$$t_o = t_x - \frac{x}{\beta_n c}$$

$$t_o = \frac{1}{2}(TDC_2 + TDC_1) - \frac{x_o}{v_{eff}} - t_{psrf} - \frac{v_{eff}}{2\beta_n c}(TDC_2 - TDC_1)$$

Replacing v_{eff} by $\beta_{eff}c$ gives

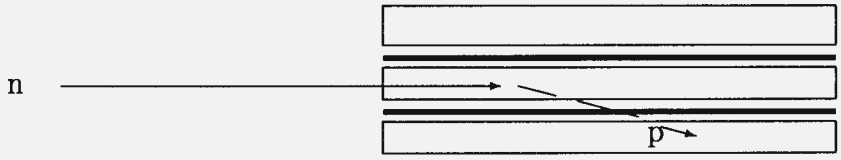

Figure 3.2: *Schematic top-view of the stack of detectors showing neutron detected in two counters. Dashed line indicates proton recoil from the detector.*

$$t_o = \frac{1}{2}(TDC_2 + TDC_1) - \frac{x_o}{\beta_{eff}c} - t_{psrf} - \frac{\beta_{eff}}{2\beta_n c}(TDC_2 - TDC_1)$$

To convert channels to time-of-flight the x_o is multiplied by
4 channels/nanosecond, being the TDC sensitivity that was used. Thus t_o becomes

$$t_o = \frac{1}{2}(TDC_2 + TDC_1) - \frac{4x_o}{\beta_{eff}c} - t_{psrf} - \frac{\beta_{eff}}{2\beta_n c}(TDC_2 - TDC_1) \qquad (3.5)$$

where

- c is the speed of light;
- β_{eff} is the effective velocity of neutrons inside the scintillator divided by speed of light;
- β_n speed of neutrons divided by speed of light, and
- x_o is the position of interaction in the scintillator.

To avoid double counting of events that were detected in two detectors, such as shown in the figure 3.2, the detector yielding the highest pulse height is

selected. The time-of-flight to the centre of the detector is calculated using equation 3.5

$$t_o = \frac{1}{2}(TDC_2 + TDC_1) - \frac{4x_o}{\beta_{eff}c} - t_{psrf} - \frac{\beta_{eff}}{2\beta_n c}(TDC_2 - TDC_1).$$

Time-of-flight was calculated for the good events[1] and the time-of-flight spectrum corresponding to the detector where the event occurred was incremented.

The calculated TOF were dependent on the length of the connecting cables and delay cables to the TDCs, and also on the flight-path to each detector. The coaxial cables were not of exactly the same length, but varied by up to 5 cm. The scintillators were also not at exactly the same flight-path relative to each other, but varied by up to 1 cm. Hence the TOF spectra associated with the twelve detectors were not time aligned with each other, but varied by up to 4 ns. To realign the TOF spectra the position of the IAS in the spectrum associated with the first detector was taken as the reference point, and the remaining TOF spectra were shifted relative to the first one, (alignment shift of -5 to 15 channels relative to the first spectrum were necessary). The twelve TOF spectra associated with the twelve detectors were then summed into a single spectrum. These summed TOF spectra were moved out of XSYS for further analysis with FORTRAN programmes.

Figure 3.3 shows neutron time-of-flight (TOF) spectra from the ^{208}Pb(p,n)^{208}Bi and the ^{181}Ta(p,n)^{181}W reactions (E_p=122 MeV) at 0°. The spectrum associated with the ^{208}Pb(p,n)^{208}Bi reaction was created by summing the TOF spectra of five runs, while the spectrum associated with the ^{181}Ta(p,n)^{181}W reaction was created by summing the TOF spectra of nine runs. In both cases the summed spectra are presented in counts/channel versus TOF (channels),

[1]Events within the allowed pulse height range as explained in section 3.1.

where 1 channel is 0.25 ns. The two spectra are dominated by the narrow Isobaric Analog State (IAS), the giant Gamow-Teller resonance (GTGR) and a broad bump in the region below and above the GTGR. In the case of the ^{208}Pb(p,n)^{208}Bi reaction six low lying discrete ^{208}Bi final states are well resolved. Typical (FWHM) energy resolutions of 580 keV for a state at E = 1.75 MeV and 420 keV for a state at E = 8.13 MeV were achieved. These structures rest on top of a background which is mainly due to cosmic ray events as well as neutron events associated with earlier beam bursts.

3.1.2 Background subtraction

The proton beam used in this experiment was produced using a pulse selection of pulses resulting in a beam-burst interval of 282 ns. The slowest neutrons leaving the target will arrive at the detector at the same time as the fastest neutrons produced by the next beam burst. This phenomenon is called wrap-around. To estimate the background due to the wrap-around, two spectra were created from the same data in such a way that their consecutive points are separated by a beam-burst interval of 282 ns. To subtract this background an exponential curve was fitted on the (p,n) spectrum above IAS as shown in figures 3.4 and 3.5 on the earlier spectrum. The tail of this exponential curve was then subtracted from the second TOF spectrum.

3.1.3 Energy calibrations

In order to convert neutron TOF spectra into excitation energy spectra, data were collected under similar conditions using a target made of a combination of natural Li and ^{12}C.

The time-of-flight spectrum at Θ_{Lab}=0° associated with the ^{7}Li(p,n)^{7}Be and ^{12}C(p,n)^{12}N reactions is shown in figure 3.11. The ground states of Be and N

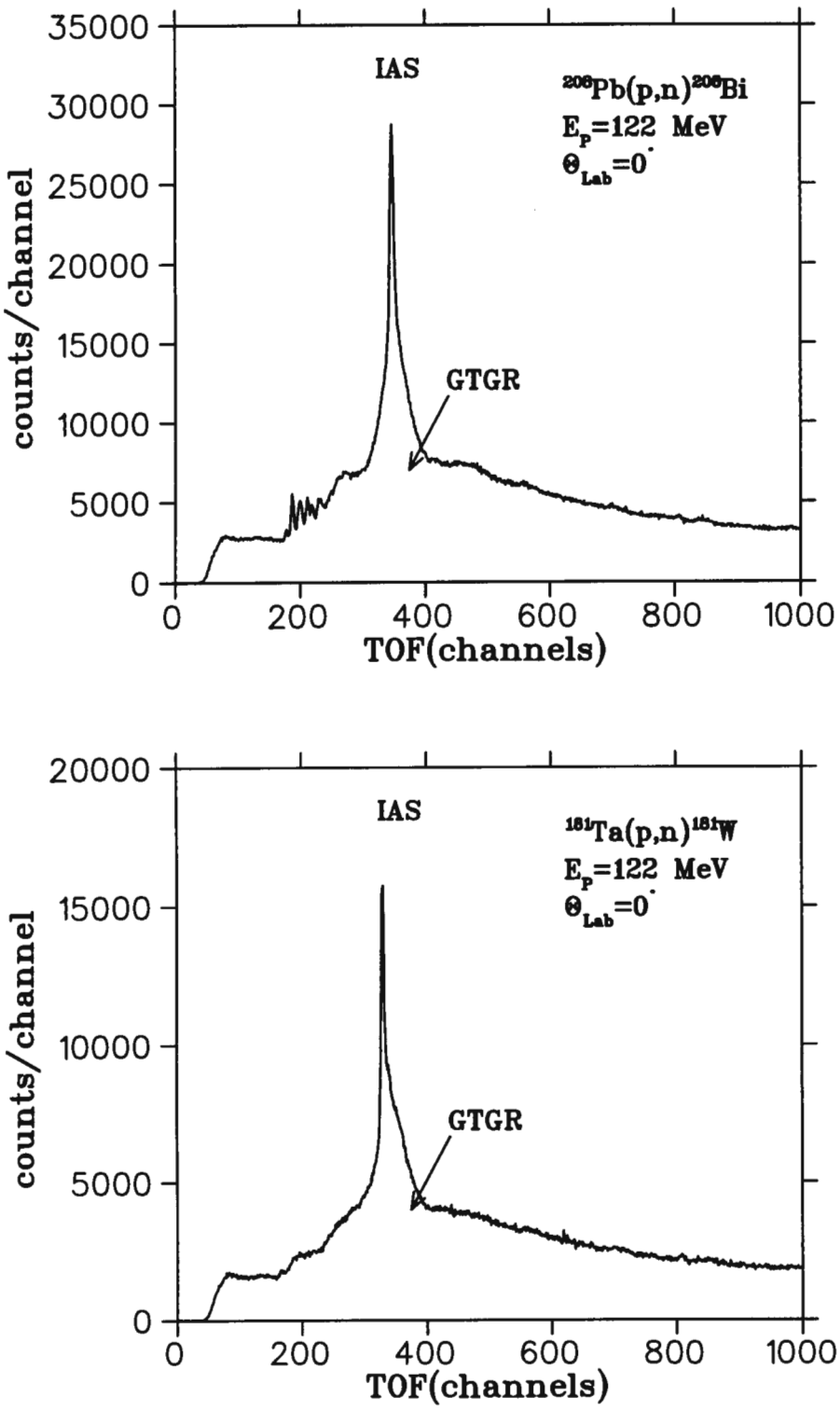

Figure 3.3: *Neutron time-of-flight spectra at* $\theta_{\mathrm{Lab}} = 0°$ *associated with the* ^{208}Pb(p,n)^{208}Bi *and* ^{181}Ta(p,n)^{181}W *reactions at* E_p=*122 MeV.*

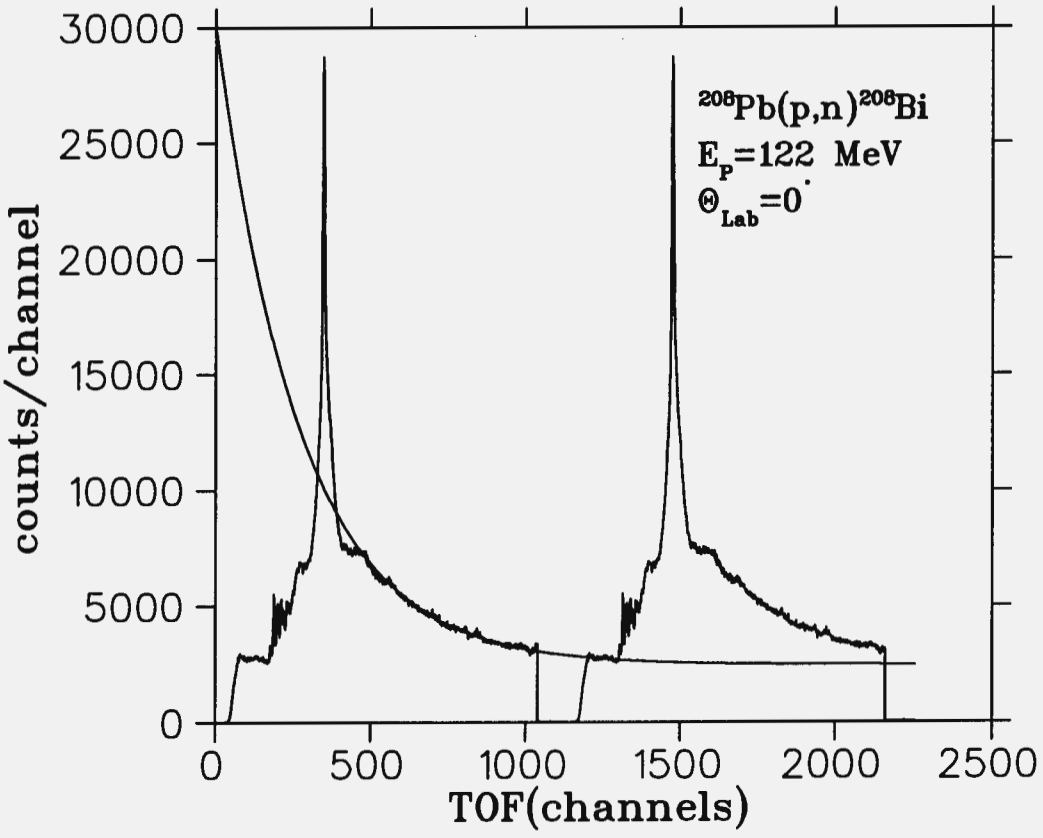

Figure 3.4: *Neutron time-of-flight spectrum at* $\Theta_{\mathrm{Lab}}=0°$ *associated with the* $^{208}Pb(\mathrm{p,n})^{208}Bi$ *reaction at* $E_{\mathrm{p}}=122$ *MeV. The fitted exponential curve was used to estimate the wrap-around contribution to the background.*

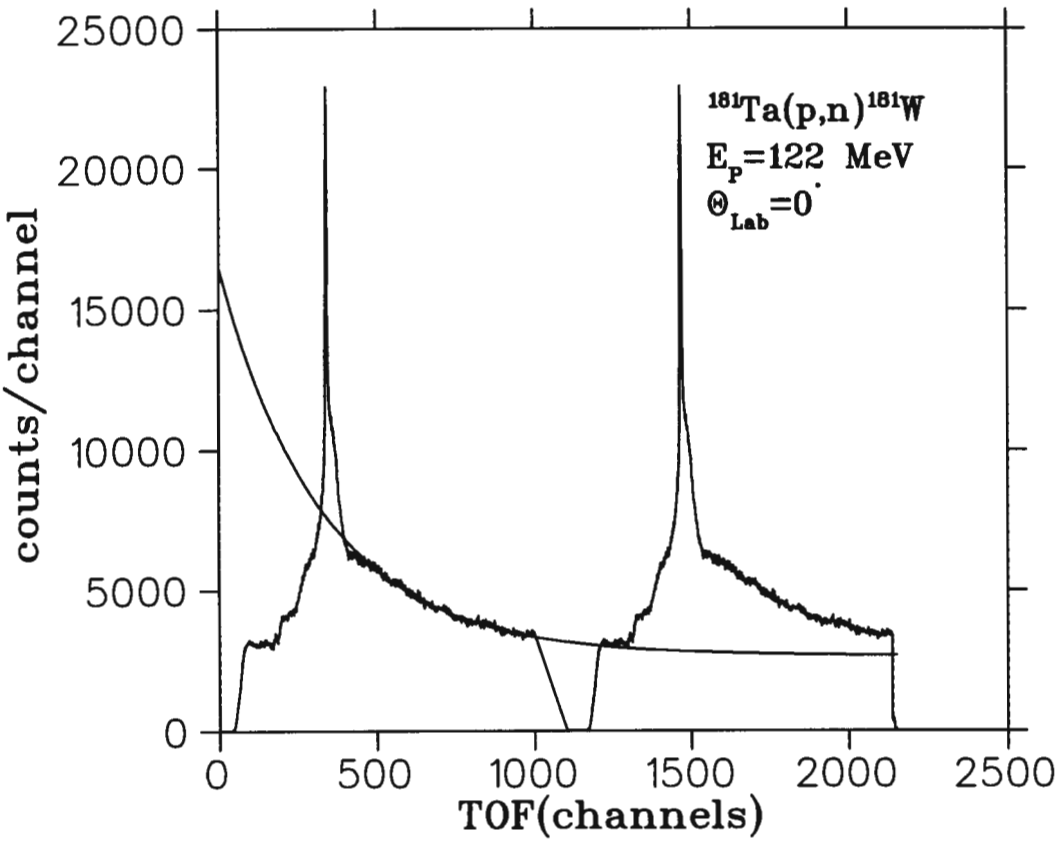

Figure 3.5: *Neutron time-of-flight spectrum at* $\Theta_{\mathrm{Lab}}=0°$ *associated with the* $^{181}Ta(\mathrm{p,n})^{181}W$ *reaction at* $E_{\mathrm{p}}=122$ *MeV. The fitted exponential curve was used to estimate the wrap-around contribution to the background.*

are at 150 and 345 channels respectively. Using the Q-value of the ^{7}Li(p,n)^{7}Be and ^{12}C(p,n)^{12}N reactions and the positions of the peaks in channels the time-of-flight offset and the flight-path were calculated. Data from other experimental targets were collected at similar conditions to ensure that the offset remained unchanged throughout the experiment.

Once events are binned in the TOF spectrum the information about the position of the events in the particular bin disappears. The events were arbitrarily spread over each bin. The neutron energy associated with each event was calculated relativistically as follows:

$$E_n = \left(\frac{1}{\sqrt{1-\beta^2}} - 1 \right) m_n$$

with

$$\beta = \frac{l}{c \times (1 \times 10^{-9}) \times t_o}$$

where

- m_n is the mass of the neutron;
- l is the flight path.

From the law of energy conservation the excitation energy (E_x) is related to the proton energy (E_{p}), the neutron energy (E_n), and the (Q-value) for the reaction, via

$$E_{\mathrm{p}} + Q = E_n + E_x.$$

After correcting for the energy lost in the target and for the center of mass motion, the excitation energy spectrum can be obtained from:

$$E_x = \frac{A}{A+1}E_{\mathrm{p}} - 0.5E_{loss} + Q - E_n \tag{3.6}$$

where

- A is the mass number of the target;
- E_{loss} is the energy lost by the proton in the target calculated using the program ELOSS [Mar 92];
- Q is the Q-value of the reaction;
- E_n is the energy of the outgoing neutron, and
- E_{p} is the energy of the incoming proton.

Equation 3.6 was used to transform TOF spectra (in channels) to excitation energy spectra (in MeV), and the excitation energy scales associated with ^{208}Pb(p,n)^{208}Bi and ^{181}Ta(p,n)^{181}W are shown in figures 3.6 and 3.7 respectively.

3.1.4 Modelling of the spectra

The yield of each state was found by fitting an individual line-shape to each "state" observed in the spectra using the non-linear least-squares minimization program MINUIT [Jam 75].
The line-shape chosen for the "states" was a symmetric Gaussian of the form

$$A \exp\left[-\frac{1}{2}\left(\frac{(x-x_0)}{\sigma}\right)^2\right]$$

where

- A is the amplitude,

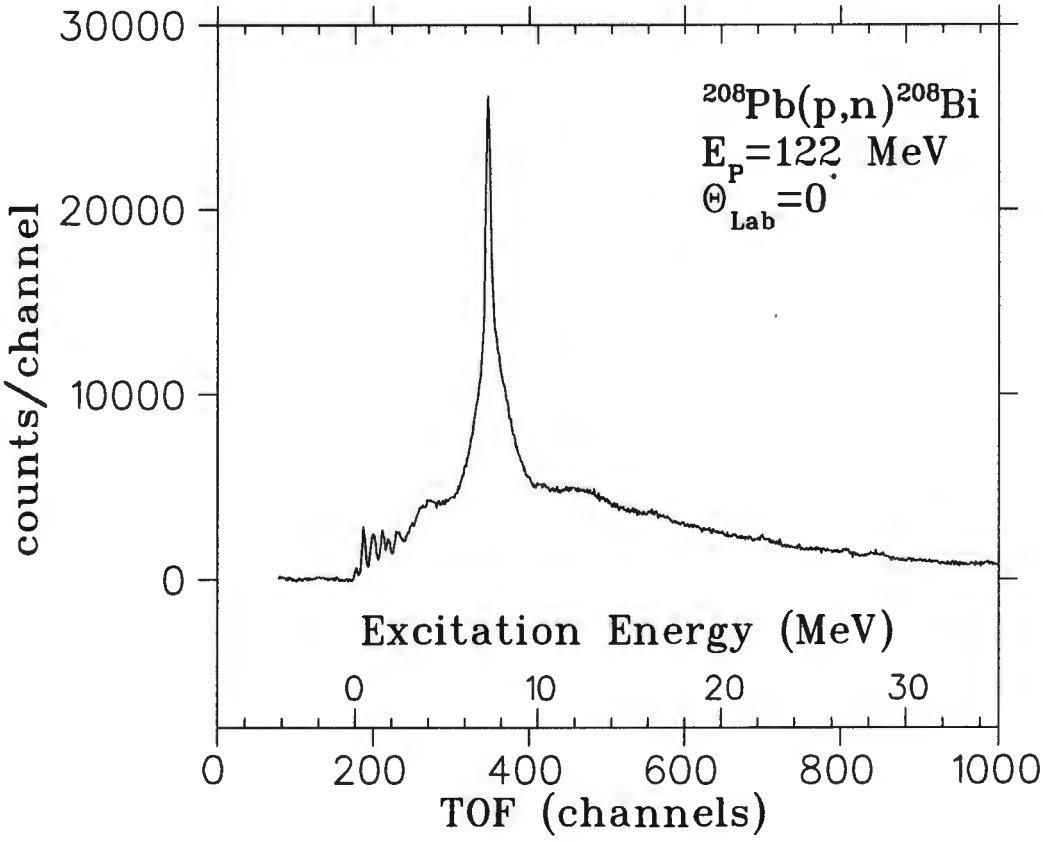

Figure 3.6: *Excitation energy spectrum at* $\Theta_{Lab}=0°$ *associated with the* $^{208}Pb(p,n)^{208}Bi$ *reaction at* $E_p=122$ *MeV.*

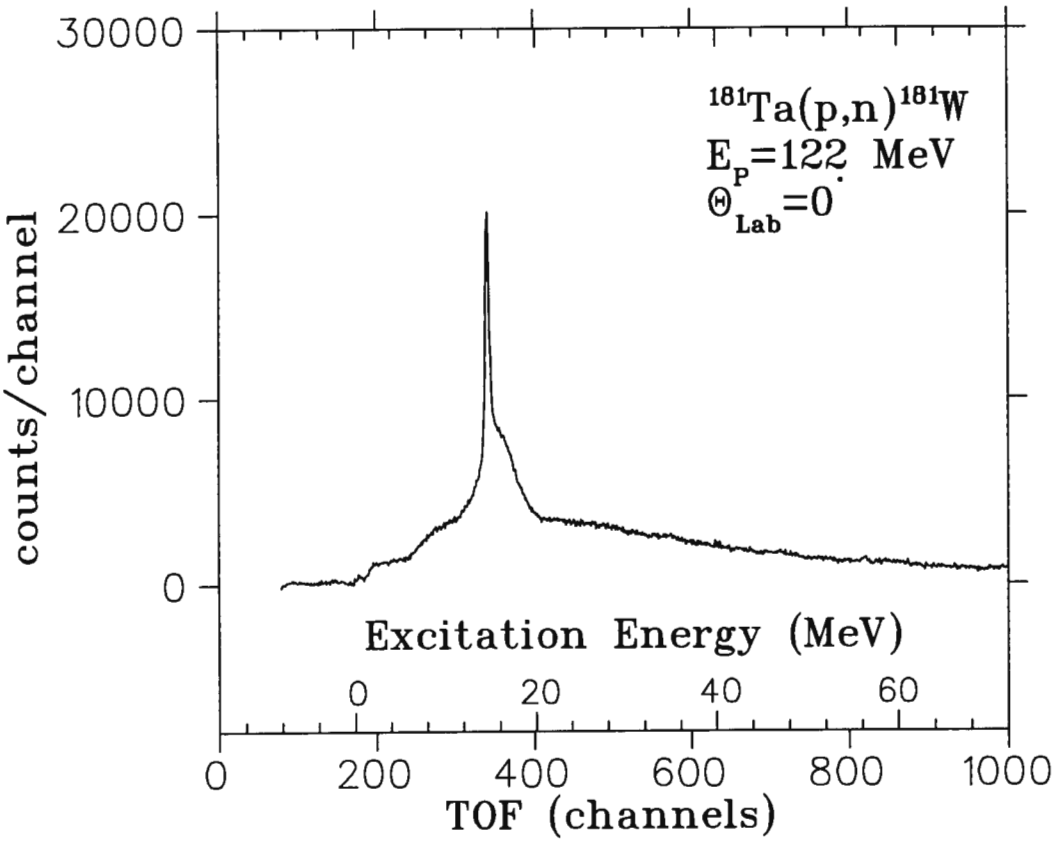

Figure 3.7: *Excitation energy spectrum at* Θ_{Lab}*=0° associated with the* ^{181}*Ta*(p,n)^{181}*W reaction at* E_{p}*=122 MeV.*

- x_0 is the centroid and
- σ is the width of the Gaussian.

The fitting was done with A, x_0, σ allowed to vary.

The TOF spectrum associated with the ^{208}Pb(p,n)^{208}Bi reaction was fitted with seventeen symmetrical Gaussians and a background of the form:

$$a + \frac{b}{1 + \exp\frac{c-x}{d}}. \tag{3.7}$$

The "states" are lying on top of the slowly increasing background as the excitation energy increases into the continuum region. The shape of this background is further confirmed by the multipole decomposition analysis as shown in figures A.5 and A.7.

The width of the resolved discrete states was determined by the experimental resolution, (FWHM) time resolution of 1.4 ns, hence the six resolved discrete states were fitted with Gaussians of equal width. The broad bump is made up of unresolved states. The number of Gaussians used to model the broad bump was varied until six Gaussians of equal width were chosen because it yielded the best χ^2 -per degree of freedom. The narrow IAS was fitted with a single Gaussian. The giant Gamow-Teller resonance (GTGR) was fitted with two Gaussians of different width and the continuum was fitted with two Gaussians of equal width. The choice of fitting the GTGR and continuum with four Gaussians of different width was arbitrary, since they are made up of an unknown number of states. The fitted TOF spectrum associated with the ^{208}Pb(p,n)^{208}Bi reaction is shown in figure 3.8.

Similarly, the TOF spectrum associated with the ^{181}Ta(p,n)^{181}W reaction is shown in figure 3.9. The total structure of the ^{181}Ta(p,n)^{181}W TOF spectrum was fitted with eleven symmetrical Gaussians and a background similar to the one described above.

Different numbers of Gaussians were fitted to model the region 0.13 MeV to 7.0 MeV. The resolved low lying state, with (FWHM) time resolution of 1.35 ns, was fitted with a single Gaussian. The next region of the spectra was fitted with two Gaussians of equal width, and four peaks of equal width were chosen to fit the broad bump because it yielded the best χ^2-per degree of freedom. The narrow IAS was fitted with a single peak. The GTGR and continuum were fitted with three peaks of different width. The choice of the width of the peaks was arbitrary, since they are made up of unknown number of states.

3.1.5 Cross section calculation

The knowledge of the target thickness used to calculate the cross section is not important in this work, but it was carefully determined. Once the yield of each peak was known the corresponding differential cross section was calculated using the relationship:

$$\frac{d\sigma}{d\Omega}(\theta) = \frac{Y}{N\Delta\Omega t[LT\epsilon(E)]} \tag{3.8}$$

where

- Y is the number of neutrons detected
- N is the number of protons incident on the target
- $\Delta\Omega$ is the solid angle subtended by the detectors
- t is the target surface density [nuclei $\cdot$ cm^{-2}]
- L is the fractional livetime of data acquisition system
- T is the neutron transmission factor from target to detector, and

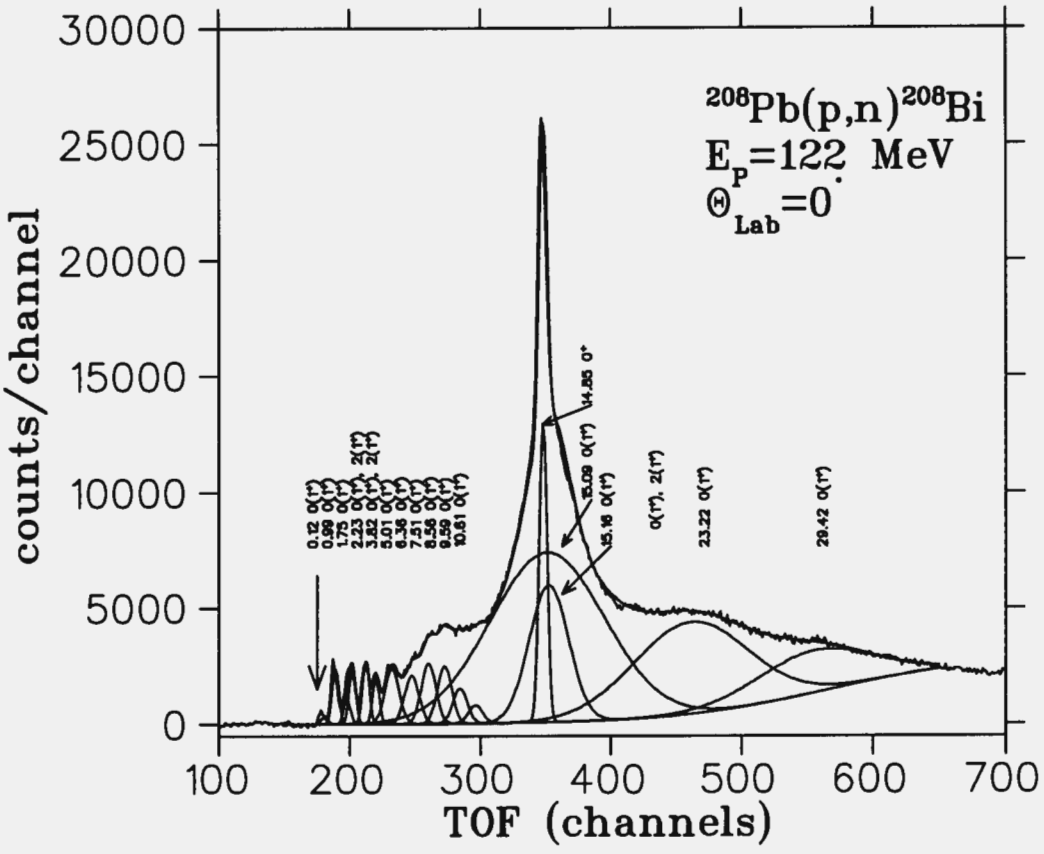

Figure 3.8: *Neutron time-of-flight spectrum at* $\Theta_{\mathrm{Lab}}=0^{\circ}$ *associated with the* ^{208}Pb(p,n)^{208}Bi *reaction at* $E_{\mathrm{p}}=122$ *MeV. The solid lines are the results from the Gaussian fitting procedure described in the text.*

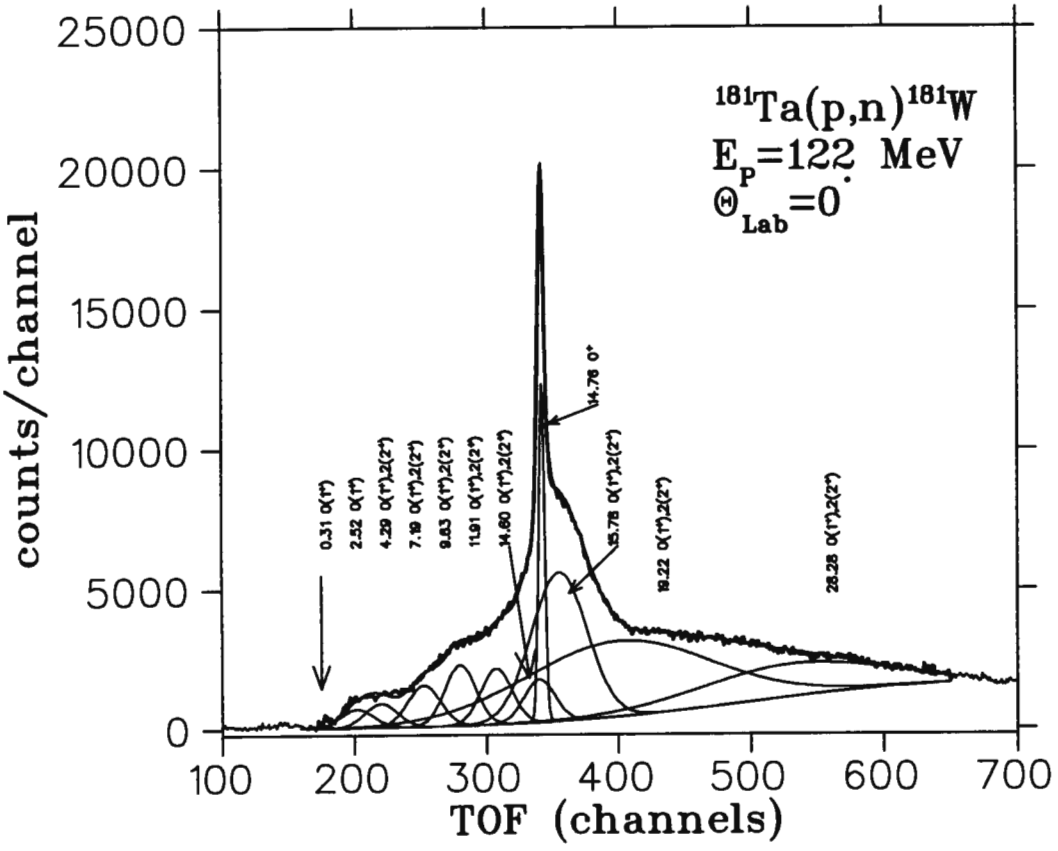

Figure 3.9: *Neutron time-of-flight spectrum at* Θ_{Lab}*=0° associated with the* ^{181}*Ta*(p,n)^{181}*W reaction at* E_{p}*=122 MeV. The solid lines are the results from the Gaussian fitting procedure described in the text.*

- $\epsilon(E)$ is the efficiency for detecting a neutron of energy E incident on the front face of the detector

The cross sections were extrapolated to $q = \omega = 0$ using the equation

$$\sigma(0,0) = \frac{\sigma(q,\omega)}{F(q,\omega)}$$

The uncertainty $\frac{\Delta\sigma}{\sigma}$ associated with the ^{208}Pb(p,n)^{208}Bi reaction, for the state at 3.13 MeV is 7.79% while that associated with the ^{181}Ta(p,n)^{181}W reaction, for the state at 4.29 MeV is 7.09%. They were propagated from the errors of Y, N, $\Delta\Omega$, t and $[LT\epsilon(E)]$, using the formula

$$\frac{\Delta\sigma}{\sigma} = \sqrt{\left(\frac{\Delta Y}{Y}\right)^2 + \left(\frac{\Delta(\Delta\Omega)}{\Delta\Omega}\right)^2 + \left(\frac{\Delta N}{N}\right)^2 + \left(\frac{\Delta t}{t}\right)^2 + \left(\frac{\Delta[LT\epsilon(E)]}{[LT\epsilon(E)]}\right)^2}$$

Yield determination

After subtracting the background, the yield of each state was estimated by integrating the area under the fitted Gaussian. The yield of each Gaussian is given by

$$Y = \sigma A\sqrt{2\pi}$$

where

- σ is the full-width at half maximum (FWHM), and
- A is the amplitude of the Gaussian

The total spectrum is made up of a number of Gaussians. The total yield is therefore the sum of the areas under all the Gaussians. The error associated with Gaussian amplitude and width were calculated by MIGRAD a subroutine of the MINUIT program.

Target thickness

The thickness of each target surface density was calculated using the relationship:

$$t = \frac{\rho d N_A}{M}$$

where

- ρ is the target density $[g \cdot cm^{-3}]$;
- d is the target thickness $[cm]$
- m is the mass of the target $[g]$
- N_A is the Avogadro's number $[mol^{-1}]$, and
- M is the molar mass $[g \cdot mol^{-1}]$

A lump of ^{7}Li was placed inside a washer(ring) of known mass and thickness. The ^{7}Li was then pressed between a Havar foils until it was level with the washer. As a check the mass of the Li was determined by weighing the total combination on an electronic balance. The mass of the ^{208}Pb and ^{181}Ta targets were determined by weighing them on the electronic balance. The thickness was measured with a micrometer screw gauge. The uncertainties associated with the target surface density t were estimated from the micrometer screw gauge and electronic balance least count and are 1.1%, 3.7% and 8.1% for ^{7}Li, ^{208}Pb and ^{181}Ta targets respectively.

$$\frac{\Delta t}{t} = \sqrt{\left(\frac{\Delta m}{m}\right)^2 + \left(\frac{\Delta d}{d}\right)^2}$$

Solid angle

The detectors were arranged in three stacks of four, longitudinal to the beam. The solid angle of the detectors is given by:

$$\Delta\Omega = \frac{N \times hb}{f_p^2}$$

where

- N is the total number of detectors
- h is the height of detectors $[cm]$
- b is the breath of the detectors $[cm]$, and
- f_p is the flight-path $[cm]$

The height ($h = 10cm$) and breath ($b = 10cm$) of the detectors were carefully measured. The center of the detectors in the TOF hut were placed 2 m away from the 100 m pre-surveyed point, thus 102 m from the target. As a check, two reference points in the spectrum associated with $^{7}Li/^{12}C$ were used to determine the flight-path f_p. The uncertainty of 0.98% associated with the solid angle $\Delta\Omega$ was propagated from

$$\frac{\Delta(\Delta\Omega)}{\Delta\Omega} = \sqrt{\left(\frac{\Delta h}{h}\right)^2 + \left(\frac{\Delta b}{b}\right)^2 + \left(\frac{2 \times \Delta f_p}{f_p}\right)^2}$$

Incident protons

The number of protons incident on the target is given by:

$$N = \frac{Q}{p_Q}$$

where

- Q is the total accumulated charge in a run or number of runs, and
- p_Q is the charge of one proton.

The error in the number of the protons incident on the target is given by the uncertainty in the integrated current from the Faraday cup. Typically the fractional error in this quantity is 0.5%.

Efficiency of detectors

In order to calculate the differential cross sections associated with the different reactions it was necessary to correct for neutron transmission (T) from the target to detectors, the efficiency of detectors (ϵ) to detect neutron at incident energy on the detector and the fractional livetime (L) of the data acquisition system. The product $TL\epsilon(E)$ was calculated using the ^{7}Li(p,n)^{7}Be(g.s + 0.43 MeV) differential cross section at zero degree as a reference cross section. The value of this cross section is 37.7 $\pm$ 3.1 mb/sr [Tad 87].
A typical neutron TOF spectrum from ^{7}Li(p,n)^{7}Be reaction associated with one detector is shown in figure 3.11. The yield of the ^{7}Be(g.s + 0.43) state was determined by summing the two partly resolved peaks from each of the twelve spectra independently. Once the yield was known the term in square bracket $[LT\epsilon(E)]$ was obtained by dividing the calculated $Y/N\Delta\Omega t$ by the reference cross section σ_r
i.e.

$$[LT\epsilon(E)] = \frac{Y}{N\Delta\Omega t\sigma_r}$$

Since the Q-values between Li, Pb and Ta are different, and the analyses extended to excitation energy of about 20 MeV, it is necessary to know the efficiencies as a function of incident neutron energy.

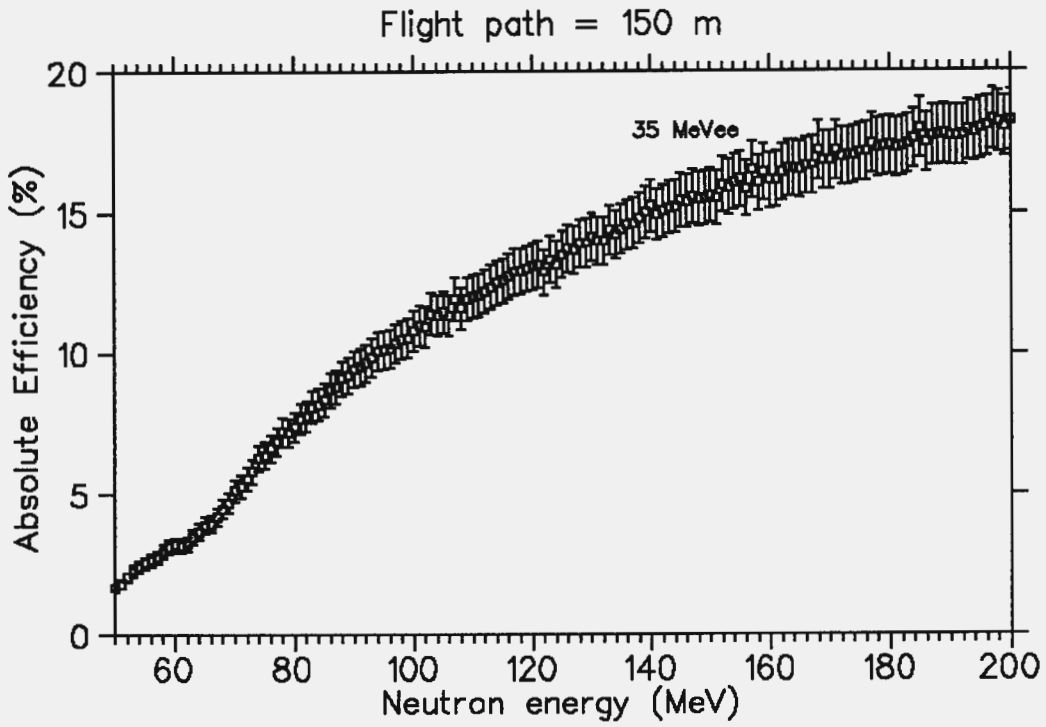

Figure 3.10: *Calculated efficiencies for the longitudinal detector orientation at a threshold of 35 MeVee. [Sty 97]*

The intrinsic detector efficiencies curves as a function of incident neutron energy at various pulse size threshold values were modelled with Monte Carlo code of Cecil, Anderson and Madey [Cec 79]. The calculated absolute efficiencies are plotted in figure 3.10 were normalised to the measured ^{7}Li(p,n)^{7}Be(g.s + 0.43) before using them to calculate the cross sections.

These values range between 8.7 and 7.0, and between 8.5 and 7.0 for the ^{208}Pb(p,n)^{208}Bi and ^{181}Ta(p,n)^{181}W reactions, with the uncertainty of 2.81% and 6.36% respectively. The calculated term in bracket was propagated from errors associated with Y, N, $\Delta\Omega$, t and σ_r.

i.e.

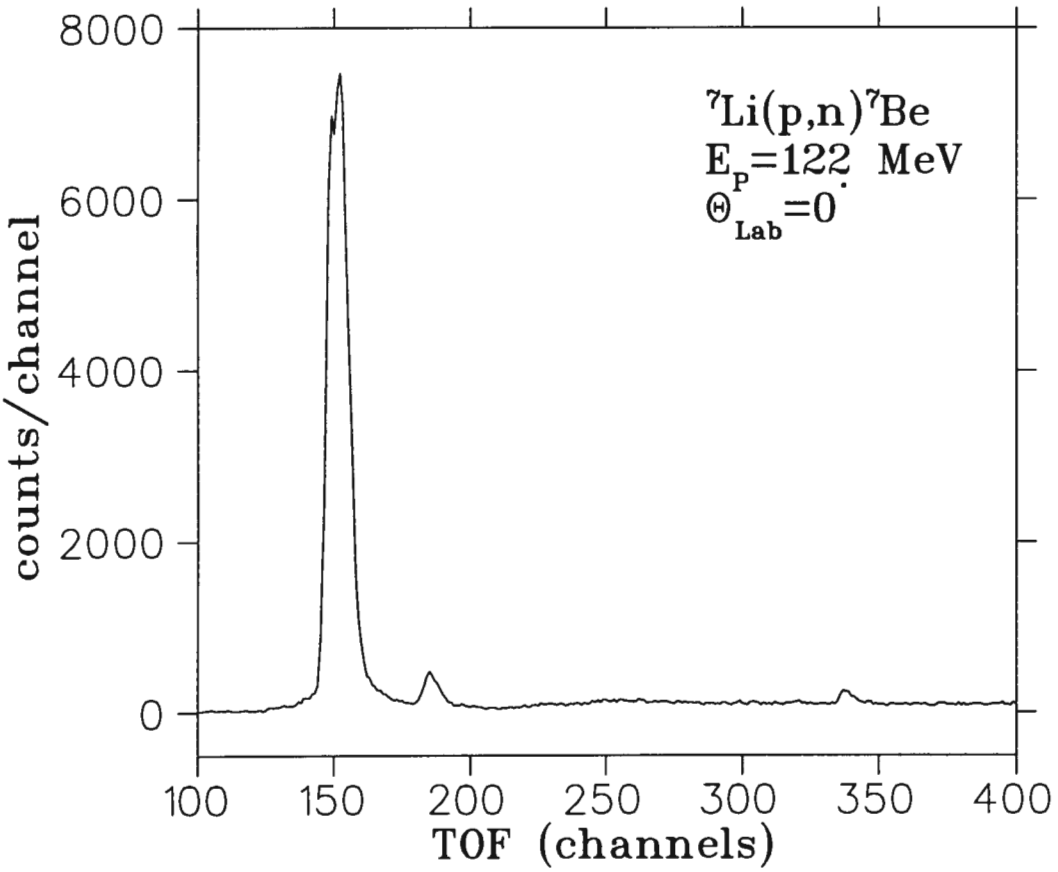

Figure 3.11: *Neutron time-of-flight spectrum at* $\Theta_{\mathrm{Lab}}=0°$ *associated with the* ^{7}Li(p,n)^{7}Be *and* ^{12}C(p,n)^{12}N *reactions at* $E_{\mathrm{p}}=122$ *MeV. The ground states of Be and N are at 150 and 345 channels respectively.*

$$\frac{\Delta[LT\epsilon(E)]}{[LT\epsilon(E)]} = \sqrt{\left(\frac{\Delta Y}{Y}\right)^2 + \left(\frac{\Delta N}{N}\right)^2 + \left(\frac{\Delta(\Delta\Omega)}{\Delta\Omega}\right)^2 + \left(\frac{\Delta t}{t}\right)^2 + \left(\frac{\Delta\sigma_r}{\sigma_r}\right)^2}$$

The weighted average $[LT\epsilon(E)]$ of all detectors in a run was calculated.

The cross sections associated with transitions to ^{208}Bi and ^{181}W final states reached via the ^{208}Pb(p,n)^{208}Bi and ^{181}Ta(p,n)^{181}W reactions are shown in the tables 3.1 and 3.2 including the propagated uncertainties from the factors discussed above.

3.1.6 Extraction of Gamow-Teller strength

^{208}Pb(p,n)

The different L transfer components of the spectra associated with the ^{208}Pb(p,n)^{208}Bi reaction were identified by a multipole decomposition analysis. The details of this procedure are given in appendix A.

All structures with L=0 angular distributions, except for the transition to the IAS, were identified as transitions to $J^{\pi} = 1^{+}$ states. The $B(GT)$ in each fitted "state" in figure 3.8 was extracted by normalizing its cross section to the cross section of the IAS (in which the Fermi strength is concentrated) using equations 1.12.

The Fermi transition strength associated with the ^{208}Pb(p,n)^{208}Bi reaction was calculated from the model independent sum rule, $B(F) = N - Z = 44$.

The extracted $B(GT)$ associated with ^{208}Pb(p,n)^{208}Bi reaction are tabulated in tables 3.1. The $\sum B(GT)$ strength of 106 ± 14 was extracted by summing the strength associated with Gaussians 1 to 15. The uncertainty of the $B(GT)$ was estimated by propagating errors associated with all terms in equation 1.12.

A good MDA must be performed to differentiate contributions from different L components. Data on the ^{208}Pb(p,n)^{208}Bi reaction were collected at only a few angles, and it was not possible to differentiate between different L components.

It was assumed that the decomposed ^{208}Pb(p,n)^{208}Bi spectra would be similar to that of ^{181}Ta(p,n)^{181}W in which it can be seen that 15% of Gaussian no 16 should be L=0. This assumption contributes about +5 to the systematic error in the $B(GT)$.

The MDA performed on the ^{181}Ta(p,n)^{181}W reaction further suggests that

10% of the strength in the region from 0 to 15 MeV is not L=0. This correction contributes -2 to the systematic error.

The measured $B(GT)$ expressed as a fraction of the sum-rule value is shown in figure 3.12. The unsymmetrical error quoted with the point include statistical errors as well as systematic errors. The systematic errors are discussed in more detail in appendix B.

The total systematic error is $^{+5}_{-2}$ and is unsymmetrical since the worst case error is to underestimate the $B(GT)$ by not including the $B(GT)$ from one of the fitted Gaussians. The $B(GT)$ predicted by the $3(N-Z)$ model independent sum rule is 132, of which 81 $\pm$ 10% was extracted from the ^{208}Pb(p,n)^{208}Bi spectrum. Of this 3.06% of the $B(GT)$ was extracted from the resolved discrete states up to 5 MeV, 8.17% was extracted from the broad bump below the IAS, and 69.72% was extracted from the GTGR. The quenching factor in the ^{208}Pb(p,n)^{208}Bi reaction is 0.81 $\pm$ 0.10.

The statistical uncertainty of 8 associated with the $B(GT)$ extracted from ^{208}Pb(p,n)^{208}Bi reaction was obtained by propagating equation 1.12. The propagated equation is given by

$$\frac{\Delta B(GT)}{B(GT)} = \sqrt{\left(\frac{\Delta\sigma_{GT}}{\sigma_{GT}}\right)^2 + \left(\frac{\Delta\sigma_{IAS}}{\sigma_{IAS}}\right)^2 + \left(\frac{\Delta(\Delta\Omega)}{\Delta\Omega}\right)^2 + \left(\frac{2\times\Delta E_p}{E_p}\right)^2 + \left(\frac{2\times 0.4}{55.0}\right)^2} \tag{3.9}$$

where

- $\left(\frac{\Delta\sigma_{GT}}{\sigma_{GT}}\right)$ is the ratio of the uncertainty associated with the cross section in the GT transition to the cross section of the GT transition;
- $\left(\frac{\Delta\sigma_{IAS}}{\sigma_{IAS}}\right)$ is the ratio of the uncertainty associated with the cross section in the IAS transition to the cross section of the IAS transition;

	E_x (MeV)	$\frac{d\sigma}{d\Omega}(q,\omega)$ (mb/sr)	L(J^π)	Strength ($B_{GT}(q,\omega)$ units)
1	0.12	0.15 ± 0.01	$0(1^+)$	0.13 ± 0.02
2	0.99	1.08 ± 0.08	$0(1^+)$	0.91 ± 0.14
3	1.75	0.89 ± 0.07	$0(1^+)$,$2(2^+)$	0.75 ± 0.11
4	2.23	0.71 ± 0.06	$0(1^+)$,$2(2^+)$	0.60 ± 0.09
5	3.82	1.15 ± 0.08	$0(1^+)$	0.96 ± 0.14
6	5.01	0.82 ± 0.07	$0(1^+)$	0.69 ± 0.11
7	6.36	0.91 ± 0.12	$0(1^+)$	0.77 ± 0.14
8	7.51	1.81 ± 0.18	$0(1^+)$	1.52 ± 0.25
9	8.56	2.29 ± 0.22	$0(1^+)$	1.92 ± 0.31
10	9.59	3.02 ± 0.32	$0(1^+)$	2.54 ± 0.43
11	10.61	2.89 ± 0.33	$0(1^+)$	2.43 ± 0.42
12	15.09	1.91 ± 0.25	$0(1^+)$	1.61 ± 0.29
13	14.85	10.26 ± 1.33	0^+	[44[a]]
14	15.16	23.99 ± 3.12	$0(1^+)$	20.19 ± 3.71[b]
15		85.39 ± 11.12	$0(1^+)$	71.84 ± 13.22[c]
16		79.16 ± 15.42	$0(1^+)$,$2(2^+)$	
17		62.96 ± 15.62	$0(1^+)$	
				$\sum_{B(GT)}$ 106.84 ± 13.75

[a] IAS

[b] GTGR

[c] GTGR

Table 3.1: *Measured differential cross sections and extracted Gamow-Teller strength associated with the* ^{208}Pb(p,n)^{208}Bi *reaction at* $E_p = 122\ MeV$. *B(F) in IAS was calculated from independent sum rule and not included in the total strength.*

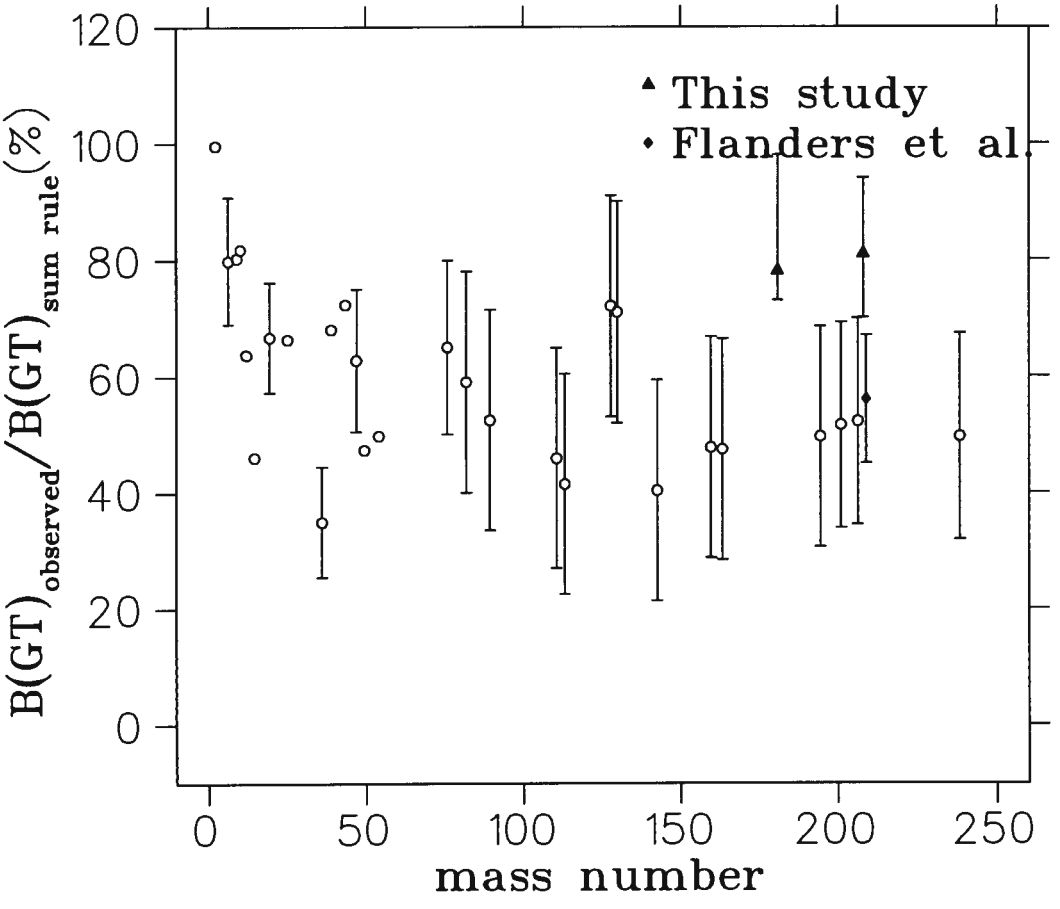

Figure 3.12: *Fraction of the Gamow-Teller sum rule strength observed in the* (p,n) *reactions from different targets. The data from present work is presented as solid triangles, including statistical and systematic errors. The data from Flanders et al. [Fla 89] is presented as solid diamond. The points and error bars of the open circles were estimated from Gaarde et al. [Gaa 85].*

- $\left(\frac{\Delta(\Delta\Omega)}{\Delta\Omega}\right)$ is the ratio of the uncertainty associated with the solid angle $\Delta\Omega$ to the solid angle;

- $\left(\frac{2\times\Delta E_p}{E_p}\right)$ is the ratio of the uncertainty associated with the proton beam energy to the proton beam energy; and

- $\left(\frac{2\times 0.4}{55.0}\right)$ is the ratio of the uncertainty associated with the dependence of strength on the proton beam energy to the dependence of strength on the proton beam energy.

^{181}Ta(p,n)

In appendix A it is explained how the different components of the spectra associated with ^{181}Ta(p,n)^{181}W reaction were identified. The Fermi strength exhausts the IAS in even-mass targets whereas in odd-mass targets a fraction, f_{GT}, of the strength is due to GT transitions. The cross section of one of the states must be known in both β decay and the (p,n) reaction in order to determine f_{GT} accurately. The extraction of $B(GT)$ the spectrum associated with ^{181}Ta(p,n)^{181}W reaction was performed by assuming that f_{GT} in the IAS is zero. In this work it was assumed that $f_{GT} = 0$.

The Fermi transition strength associated with the ^{181}Ta(p,n)^{181}W is given by $B(F) = N - Z = 35$.

The extracted $B(GT)$ associated with ^{181}Ta(p,n)^{181}W reaction are tabulated in table 3.2. The uncertainty of the $B(GT)$ were estimated by propagating errors associated with the terms in equation 1.12. The $\sum B(GT)$ of 82 ± 4 was obtained by summing strength associated with gaussians 1 to 10.

The independent sum rule predicted that the value for the $B(GT)$ is 105, and $78 \pm 3\%$ was extracted experimentally. 0.12% of the $B(GT)$ was extracted from the resolved state at 0.31 MeV, 21.13% was extracted from the broad

	E_x (MeV)	L(J^π)	$\frac{d\sigma}{d\Omega}(q,\omega)$ (mb/sr)	Strength ($B_{GT}(q,\omega)$ units)
1	0.31	$0(1^+)$	0.16 ± 0.02	0.13 ± 0.02
2	2.52	$0(1^+)$	2.00 ± 0.15	1.60 ± 0.21
3	4.29	$0(1^+)$,$2(2^+)$	2.57 ± 0.20	2.05 ± 0.28
4	7.19	$0(1^+)$,$2(2^+)$	4.58 ± 0.39	3.67 ± 0.51
5	9.63	$0(1^+)$,$2(2^+)$	6.61 ± 0.60	5.30 ± 0.75
6	11.91	$0(1^+)$,$2(2^+)$	6.47 ± 0.64	5.18 ± 0.77
7	14.60	$0(1^+)$,$2(2^+)$	5.48 ± 0.69	4.39 ± 0.73
8	14.76	0^+	8.58 ± 0.94	[35[a]]
9	15.78	$0(1^+)$,$2(2^+)$	36.07 ± 4.04	
10	19.22	$0(1^+)$,$2(2^+)$	74.72 ± 10.10	59.82 ± 10.43[b]
11	28.28	$0(1^+)$,$2(2^+)$	72.00 ± 13.87	
				$\sum_{B(GT)}$ 82.14 ± 3.54

[a] IAS

[b] GTGR

Table 3.2: *Measured differential cross sections and extracted Gamow-Teller strength associated with the* ^{181}Ta(p,n)^{181}W *reaction at* $E_p = 122\ MeV$. *B(F) in IAS was calculated from independent sum rule and not included in the total strength.*

bump below the IAS and 56.97% was extracted from the GTGR. In the ^{181}Ta(p,n)^{181}W reaction the quenching factor of 0.78 $\pm$ 0.03 was calculated. The uncertainty of 2 associated with the $B(GT)$ extracted from ^{181}Ta(p,n)^{181}W reaction was propagated from equation 3.9.

The MDA performed on the ^{181}Ta(p,n)^{181}W spectrum suggest that 15% of Gaussian number 11 is L=0. This contributes +2 to the B(GT). The MDA also suggests that the 10% of the strength in the region from 0 to 15 MeV is not L=0. This correction contributes -3 to the systematic error in the $B(GT)$.

The total systematic error is $^{+19}_{-3}$ as calculated in appendix B.3 and is unsymmetrical since the worst case error is to underestimate the $B(GT)$ by not including the $B(GT)$ from one of the fitted Gaussians.

Chapter 4

Conclusion

A quantitative study has been carried out on the ^{208}Pb(p,n)^{208}Bi and ^{181}Ta(p,n)^{181}W reactions at E_p = 122 MeV. In both reactions the TOF spectra (in channels) were converted to excitation energy spectra (in MeV). The position of each state in the spectra associated with ^{208}Pb(p,n)^{208}Bi and ^{181}Ta(p,n)^{181}W reactions was identified, in particular the IAS of Pb at 14.85 MeV, and the IAS of Ta at 14.34 MeV. The cross section for each state in the two spectra was calculated.

DWIA calculations were performed to estimate the cross sections due to L=0, 1 and 2 multipole transfers. The spectra associated with the two targets were decomposed into different multipoles. In the spectrum associated with the ^{208}Pb(p,n)^{208}Bi reaction, most of the components were L=0 except around excitation energies of 4 and 18 MeV where very little of the components were L=2. This $B(GT)$ extends into the continuum region.

In the spectrum associated with the ^{181}Ta(p,n)^{181}W reaction, the excitation energy spectrum was composed mainly of L=0 and L=2 in the region above 15 MeV. According to the MDA the L=0 multipole component vanishes above 29 MeV.

The $B(GT)$ of all states was estimated for the two reactions and it was found that in both cases it is less than the strength predicted by the sum rule. The value of the $\sum B(GT)$ extracted from the ^{208}Pb(p,n)^{208}Bi reaction with its statistical error and systematic error is $106 \pm 14|_{stat.}\,{}^{+5}_{-2}|_{syst.}$. An upper limit on the $\sum B(GT)$ extracted below an excitation energy of 26 MeV was 81 $\pm$ 10% of the model independent sum rule of $B(GT) = 3(N - Z) = 132$. The $B(GT)$ of 3.06%, 8.17% and 69.72% were extracted from the resolved discrete states up to 5 MeV, the broad bump below the IAS and the GTGR respectively.

The value of the $\sum B(GT)$ extracted from the ^{181}Ta(p,n)^{181}W reaction with its statistical error and systematic error is $82 \pm 4|_{stat.}\,{}^{+19}_{-3}|_{syst.}$. The $\sum B(GT)$ extracted below 20 MeV excitation energy was 78 $\pm$ 3% of the model independent sum rule of $B(GT) = 3(N - Z) = 105$. The $B(GT)$ of 0.12%, 21.13% and 56.97% were extracted from the resolved discrete state at 0.31 MeV, the broad bump below the IAS and the GTGR respectively.

The value of 81 $\pm$ 10% of the fraction of $B(GT)$ in the sum rule associated with ^{208}Pb(p,n)^{208}Bi reaction is higher than a measurement on the same target [Fla 89]. The value of 78 $\pm$ 3% of the fraction of $B(GT)$ in the sum rule associated with ^{181}Ta(p,n)^{181}W reaction is in good agreement with measurement the even-mass target in this work as shown in figure 3.12.

In ^{208}Pb(p,n)^{208}Bi reaction $B(GT)$ is quenched by a factor of 0.81 $\pm$ 0.10 whereas in ^{181}Ta(p,n)^{181}W reaction is quenched by a factor of 0.78 $\pm$ 0.03. The quenching of the $B(GT)$ remains an open question. Because of the difficulty of finding $B(GT)$ that has spread into the continuum, the amount of $B(GT)$ found is subject to large systematic errors. But the experiment does show that the quenching of the $B(GT)$ is the same in the odd mass nucleus ^{181}Ta and the even mass nucleus ^{208}Pb. This raises the interesting question of

whether the previous authors [Gaa 85] overestimated the background in odd A nuclei. If confirmed by further work, such an effect could provide a clue as to the nature of the quenching, which remains an area of active debate, more than two decades after its discovery.

The method used to extract the $B(GT)$ in this experiment is dependent on the normalization of the GT cross section to the Fermi cross section in the IAS. The situation is more complicated in the case of an odd-mass nuclei target where the IAS is composed of a mixture of $B(GT)$ and $B(F)$. A possible solution to this problem is to perform the (p,n) experiment using polarized beams, where one can separate $B(GT)$ and $B(F)$ components by a D_{NN} measurement.

Appendix A

Multipole decomposition analysis

Data were collected at low momentum transfer to ensure that the TOF spectra were not contaminated with higher multipole transfers. Nevertheless, the resulting total neutron TOF spectra are made up of different multipole L contributions. To extract the $B(GT)$ it is necessary to separate the L = 0 contribution from higher multipoles.

The contamination of the TOF spectrum with multipole components other than L=0, was estimated using the software package MDA by Park [Par 91]. The following ingredients are required to run these programs:

- differential cross sections from distorted-wave impulse approximation (DWIA) calculations,
- the Jacobian to transform laboratory angles to centre-of-mass(c.m.) angles
- and the excitation energy spectra, binned into 1 MeV bins.

A.1 DWIA calculations

The DWIA calculations were performed at the Indiana University Cyclotron Facility using the program DW81 [Com 81]. The following inputs were required:

- The Franey and Love [Fra 85] 140 MeV t-matrices form of the effective free NN-interactions needed to calculate the angular distributions for the E_p=122 MeV data, for ^{208}Pb(p,n)^{208}Bi and ^{181}Ta(p,n)^{181}W reactions.

- For the E_p=122 MeV ^{208}Pb(p,n)^{208}Bi and ^{181}Ta(p,n)^{181}W data, the optical model parameters used to generate the distorted wave are those of Schwandt's phenomelogical global parameters [Nad 81] and Raben [Rab 92], respectively;

- The harmonic oscillator single-particle wave functions are commonly used in studies of inelastic nucleon scattering. The harmonic oscillator parameter b was determined from [Ber 72] [Car 86],

$$b = 0.960A^{\frac{1}{6}}[1 - (0.556)A^{-\frac{1}{2}}]^{-\frac{1}{2}}(fm),$$

  where $b = 2.45\ fm$ and $b = 2.40\ fm$ for the ^{208}Pb and ^{181}Ta, respectively.

- Z_j is the nuclear structure coefficient that normalizes the p-h transition. The coefficients of the cross sections for different multipole (L) transfers are determined using a χ^2-minimization routine. The absolute cross section is not required, so an arbitrary choice of Z_j=1 was made in running the code DW81;

The above inputs, the incident nucleon energy and excitation energy are supplied for the DW81 calculation to create the outputs containing $\sigma(\theta)$ or $\sigma(q)$.

A.1.1 Optical Model potential

A local, complex, spin-dependent Optical Model potential of conventional form, containing a Coulomb term, a complex nuclear central term, and a complex nuclear spin-orbit (SO) term:

$$U(r) = U_{Coul}(r) - V f_0(r) - i(W_s - 4a_w W_D \frac{d}{dr}) f_w(r)$$
$$+2(V_{so} + iW_{so})\frac{1}{r}\frac{d}{dr} f_{so}(r)\vec{L}\cdot\vec{\sigma} \qquad \text{(A.1)}$$

with Woods-Saxon (WS) form factors $f_x(r; r_x, a_x)$ and 10 free parameters (V, r_0, a_0, W_S, r_w, a_w, V_{so}, W_{so}, r_{so}, and a_{so}) was used to perform the DWIA calculations. The factor 2 multiplying the SO term is the conventional pion Compton wavelength factor $(\hbar/m_\pi c)^2$ in fm^2.

The values of the 10 free parameters for the ^{208}Pb(p,n)^{208}Bi and ^{181}Ta(p,n)^{181}W reactions are given in tables A.1 and A.2 respectively.

Possible choices of 1p-1h configurations investigated for the ^{208}Pb(p,n)^{208}Bi and ^{181}Ta(p,n)^{181}W reactions for a given J$^\pi$ state were $1^+, 1^-, 2^-, 2^+$, these are not pure-L transitions, but coherent mixtures. These J$^\pi$ states were chosen because they dominate the L=0, L=1 and L=2 transfers.

(a) ^{208}Pb(p,n)^{208}Bi reaction DWIA output.

The output of the DW81 calculation for the $3p_{\frac{3}{2}}3p_{\frac{1}{2}}^{-1}$ 1p-1h configuration J$^\pi$=1$^+$ (L=0) can be found in figure A.1 (a). Figure A.1 (b) shows the $3d_{\frac{5}{2}}3p_{\frac{3}{2}}^{-1}$ 1p-1h configuration for J$^\pi$=2$^-$ (L= 1) peaking at 5° and figure A.1

symbols	Optical Model Parameterisation	Values used
V	$(92.5 + 64\ \frac{N-Z}{A})$(1-0.155ln E_p)	27.08
V	$(92.5 - 64\ \frac{N-Z}{A})$(1-0.155ln E_p)	20.16
r_o	$1.18 + (0.34 + 6.5\ A^{-1})\ 10^{-3}\ E_p$	1.23
W_s	$3.8 + 3\ \frac{N}{Z} + 1.23 \times 10^{-3}\ (E_p - 135)^2$	8.62
r_w	$1.16 + \beta$ ln(185 - E_p), $\beta \equiv 0.058$, Pb	1.40
a_w	$0.37 + 1.8 \times 10^{-3}\ E_p$	0.59
V_{so}	$16.5(1 - \eta \ln E_p)$, $\eta = 0.160 + 0.06\ \frac{N-Z}{A}$	2.81
W_{so}	5.2(1 - 0.262 ln E_p)	-1.34
r_{so}	$1.015 + 5 \times 10^{-4}$ A	1.12
a_{so}		0.60

Table A.1: *The optical model parameters [Nad 81] used in the distorted-wave impulse approximation calculations for the* ^{208}Pb(p,n)^{208}Bi *reaction. All potential depths are in MeV, and all geometrical parameters are in fm.*

symbols	Global Optical Model Parameters	Values used
V	$(95 + 40\ \frac{N-Z}{A})(1\text{-}0.16\ln E_p)$	23.76
V	$(95 - 40\ \frac{N-Z}{A})(1\text{-}0.16\ln E_p)$	20.19
r_o	$1.20 + 3.7 \times 10^{-4}\ E_p$	1.25
W_s	$(1 + 3.033\ \frac{N-Z}{A})(4.335 + 4.10 \times 10^{-2}\ E_p)$	14.81
r_w	$0.68 + 4 \times 10^{-3}\ E_p - 10^{-5}\ E_p^2$	1.32
a_w	$0.257 + 2.96 \times 10^{-3}\ E_p$	0.62
V_{so}	$7.09 - 2.44 \times 10^{-2}\ E_p$	4.11
W_{so}	$0.667 - 1.33 \times 10^{-2}\ E_p$	-0.96
r_{so}	$0.92 + 3.3 \times 10^{-3}\ A^{\frac{1}{3}}$	0.92
a_{so}	$0.484 + 3.98 \times 10^{-3}\ A^{\frac{1}{3}}$	0.49

Table A.2: *The optical model parameters [Rab 92] used in the distorted-wave impulse approximation calculations for the* ^{181}Ta(p,n)^{181}W *reaction. All potential depths are in MeV, and all geometrical parameters are in fm.*

(c) shows the $2f_{\frac{5}{2}}3p_{\frac{3}{2}}^{-1}$ 1p-1h and configuration for $J^{\pi}=2^{+}$ (L=2) peaking at 10°.

(b) ^{181}Ta(p,n)^{181}W reaction DWIA output.

The output of the DW81 calculation for the $1h_{\frac{11}{2}}1h_{\frac{9}{2}}^{-1}$ 1p-1h configuration $J^{\pi}=1^{+}$ (L=0) is shown in figure A.2 (a), and figure A.2 (b) shows the $3s_{\frac{1}{2}}3p_{\frac{3}{2}}^{-1}$ 1p-1h configuration for $J^{\pi}=2^{-}$ peaking at 5°. Figure A.2 (c) shows the $2f_{\frac{7}{2}}1h_{\frac{9}{2}}^{-1}$ 1p-1h configuration for $J^{\pi}=2^{+}$ peaking at 10°.
For each 1p-1h configuration DWIA calculations were performed in steps of 5 MeV from 0 to 30 MeV in excitation energy. The three 1p-1h configuration outputs for each excitation energy are shown in figures A.3 and A.4, for ^{208}Pb(p,n)^{208}Bi and ^{181}Ta(p,n)^{181}W reactions respectively.

A.2 MDA calculations

For both the ^{208}Pb(p,n)^{208}Bi and the ^{181}Ta(p,n)^{181}W data, a multipole decomposition analyses were performed to identify different L transfers contributing to the excitation energy spectra. The DW81 differential cross sections were calculated at 5 MeV in excitation energy intervals, from 0 to 30 MeV for each $p-h$ configuration to represent the J^{π} state of interest. the excitation energy interval of 5 MeV is adequate since the shapes of $\frac{d\sigma}{d\Omega}(\theta)$ do not change by much as shown in figure A.1 and A.2. To match 1 MeV binning of experimentally observed cross sections, an interpolation routine was used to supply necessary shapes in steps of 1 MeV.
The angular distribution for each 1 MeV excitation energy is given by [Blo 91]

$$\left(\frac{d\sigma}{d\Omega}\right)_{DATA} = \sum_{L=0}^{3} A_L \left(\frac{d\sigma}{d\Omega}(\theta)\right)_L .$$

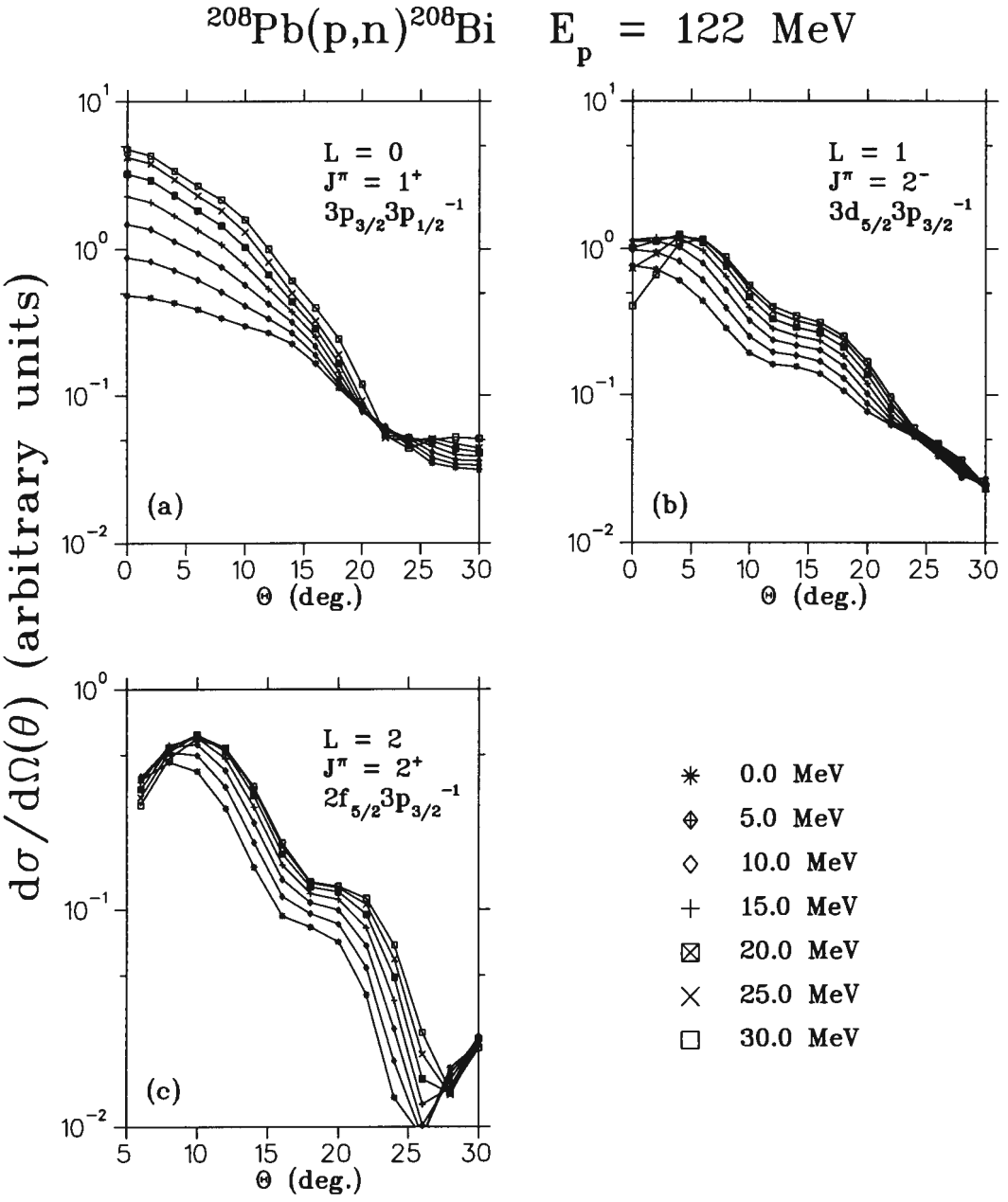

Figure A.1: *DWIA differential cross section for the ^{208}Pb(p,n)^{208}Bi reaction at incident energy of 122 MeV for (a) L- and J^π- transfers of 0 and 1^+, (b) L- and J^π- transfers of 1 and 2^- and (c) L- and J^π- transfers of 2 and 2^+ respectively. The differential cross sections were calculated in steps of 5 MeV from 0 to 30 MeV in excitation energy.*

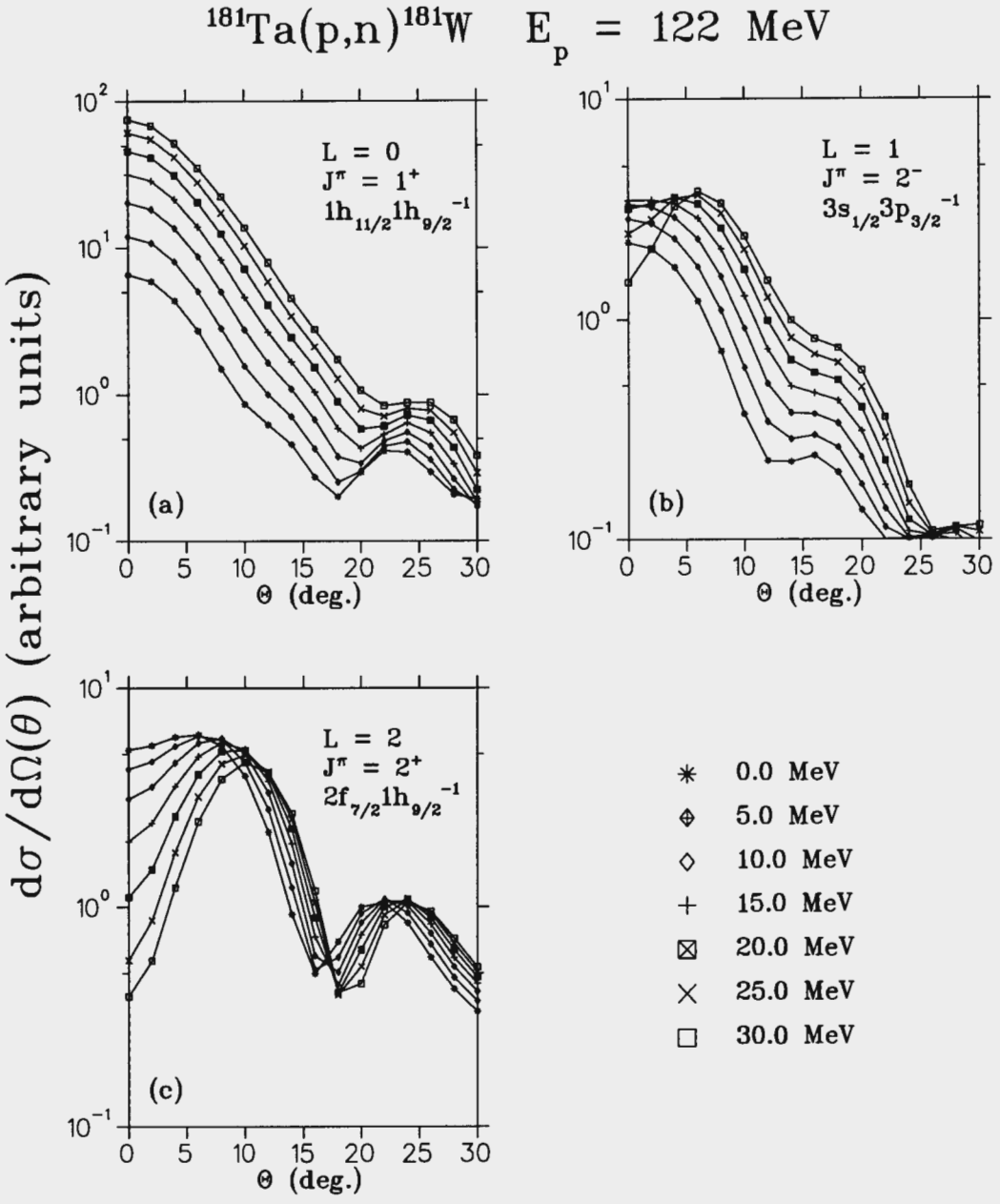

Figure A.2: *DWIA differential cross section for the* ^{181}*Ta*(p,n)^{181}*W reaction at incident energy of 122 MeV for (a) L- and* J^π*- transfers of 0 and* 1^+*, (b) L- and* J^π*- transfers of 1 and* 2^- *and (c) L- and* J^π*- transfers of 2 and* 2^+ *respectively. The differential cross sections were calculated in steps of 5 MeV from 0 to 30 MeV in excitation energy.*

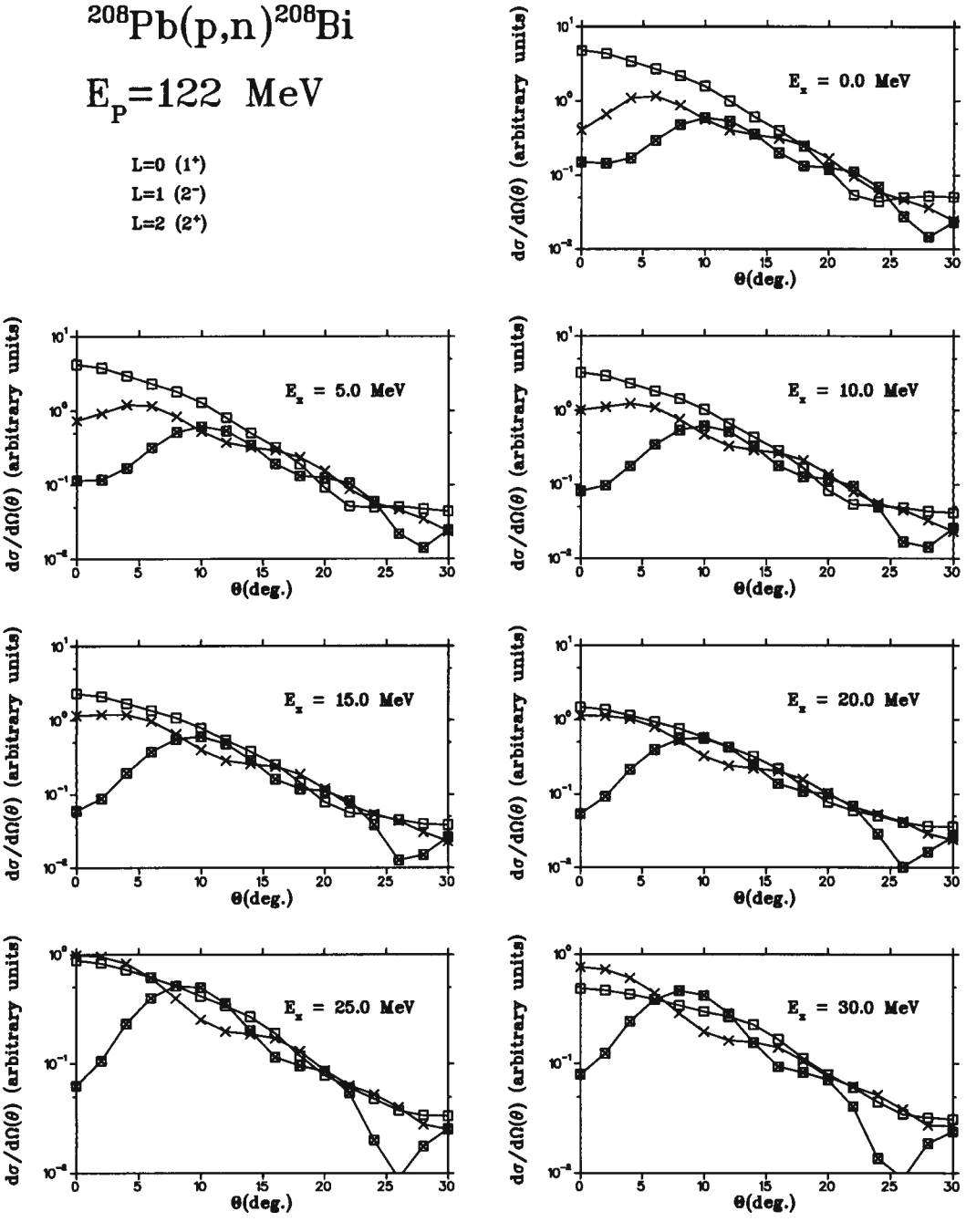

Figure A.3: *Calculated DWIA differential cross section for the* ^{208}Pb(p,n)^{208}Bi *reaction at an incident energy of 122 MeV.*

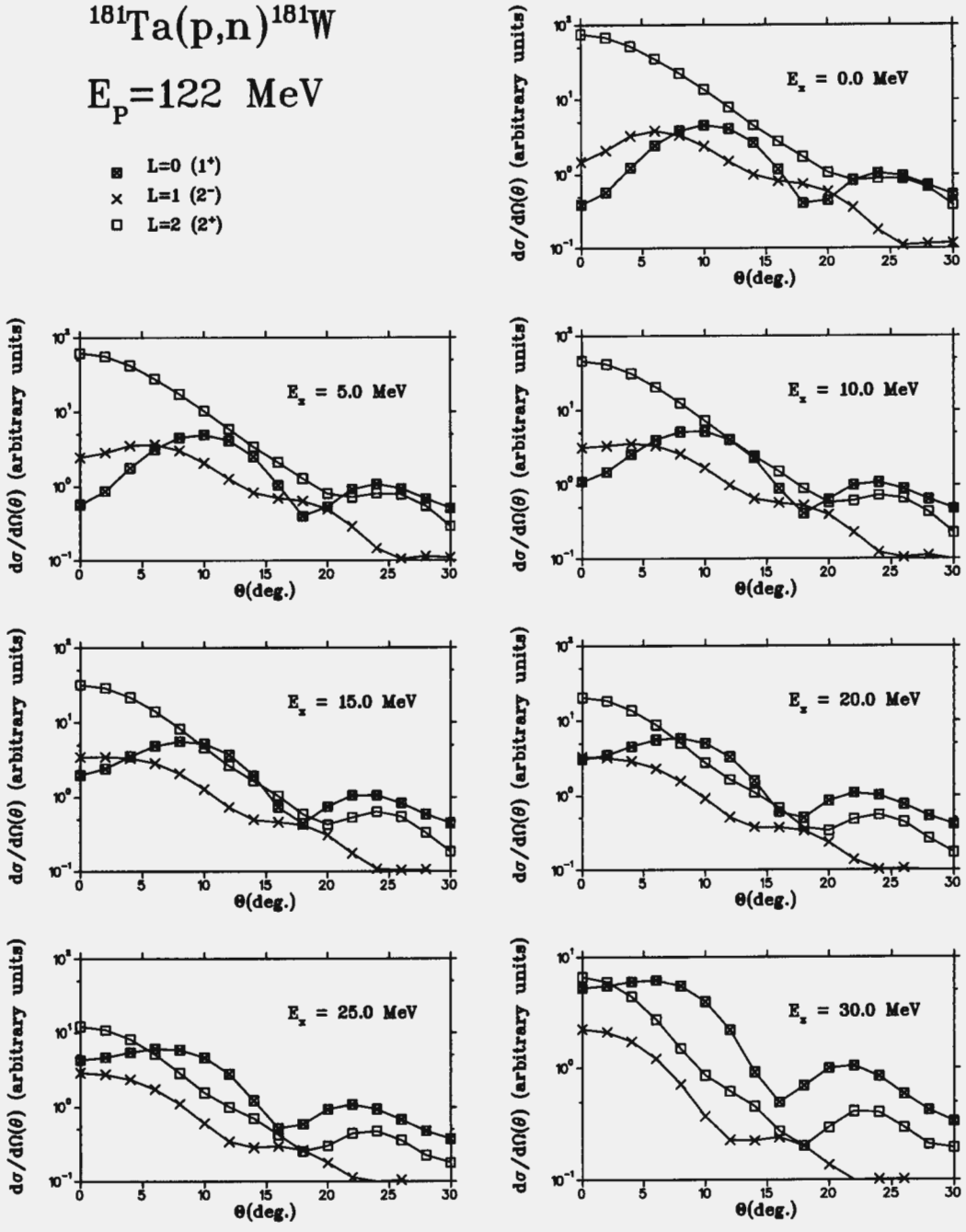

Figure A.4: *Calculated DWIA differential cross section for the* ^{181}*Ta*(p,n)^{181}*W reaction at an incident energy of 122 MeV.*

L	J^π	^{208}Pb(p,n)^{208}Bi	J^π	^{181}Ta(p,n)^{181}W
0	1^+	$3p_{\frac{3}{2}}3p_{\frac{1}{2}}^{-1}$	1^+	$1h_{\frac{11}{2}}1h_{\frac{9}{2}}^{-1}$
1	2^-	$3d_{\frac{5}{2}}3p_{\frac{3}{2}}^{-1}$	2^-	$3s_{\frac{1}{2}}3p_{\frac{3}{2}}^{-1}$
2	2^+	$2f_{\frac{5}{2}}3p_{\frac{3}{2}}^{-1}$	2^+	$2f_{\frac{7}{2}}1h_{\frac{9}{2}}^{-1}$

Table A.3: *The three particle-hole configurations used in multipole decomposition analysis.*

The coefficients A_L's were determined by a least-squares-fit method. The multipole decomposition analysis for the ^{208}Pb(p,n)^{208}Bi data was done by using 0°, 2° and 4° angles, and the ^{181}Ta(p,n)^{181}W data was done by using 0°, 2°, 4° and 10° angles.

The three 1p-1h configurations used in the multipole decomposition analysis for the ^{208}Pb(p,n)^{208}Bi and ^{181}Ta(p,n)^{181}W data are listed in table A.3.

The forward angle spectra for the ^{208}Pb(p,n)^{208}Bi and ^{181}Ta(p,n)^{181}W reactions are dominated by ΔL=0, ΔS=1, i.e. $\Delta J^\pi = 1^+$, transfer known as *GT* transitions.

(a) ^{208}Pb(p,n)^{208}Bi data

In figures A.5 and A.6, the multipole decomposed spectra are shown for the E_p=122 MeV ^{208}Pb(p,n)^{208}Bi data. In these figures, individual $\sigma(\theta)^{J^\pi}$'s are displayed with uncertainties from a χ^2-minimization routine for angles $\theta_{\rm Lab}$ = 0°, 2° and 4°, and the $\sigma(\theta)_L$ normalized to the α_L coefficients also shown with data. The statistical uncertainties of the measured cross section are shown in these figures.

For these data the sum of $\sigma(\theta)^{J^\pi}$'s with $J^\pi = 1^+$, 2^- and 1^+ states match the data reasonably well. But the MDA method was not sensitive enough

to identify all L transfers contributing to the excitation energy spectra since data were collected at only three angles. Nevertheless L=2 components can be seen near 4 MeV and 18 MeV.

(b) ^{181}Ta(p,n)^{181}W data

Figures A.7 and A.8, show the multipole decomposed spectra for the E_p = 122 MeV ^{181}Ta(p,n)^{181}W data. In these figures, individual $\sigma(\theta)^{J^\pi}$'s are displayed with uncertainties from a χ^2-minimization routine for angles θ_{Lab} = 0°, 2°, 4° and 10° and the $\sigma(\theta)_L$ normalized to the α_L coefficients also shown with data. The statistical uncertainties of the measured cross section are shown in these figures.

For these data the sum of $\sigma(\theta)^{J^\pi}$'s with $J^\pi = 1^+$, 2^- and 2^+ states match the data well. The presence of the $J^\pi = 2^+$ state is more pronounced at E_x greater than 15 MeV. The $J^\pi = 1^+$ also decreases with increasing θ_{Lab}, which is a characteristic of L=0 transfer.

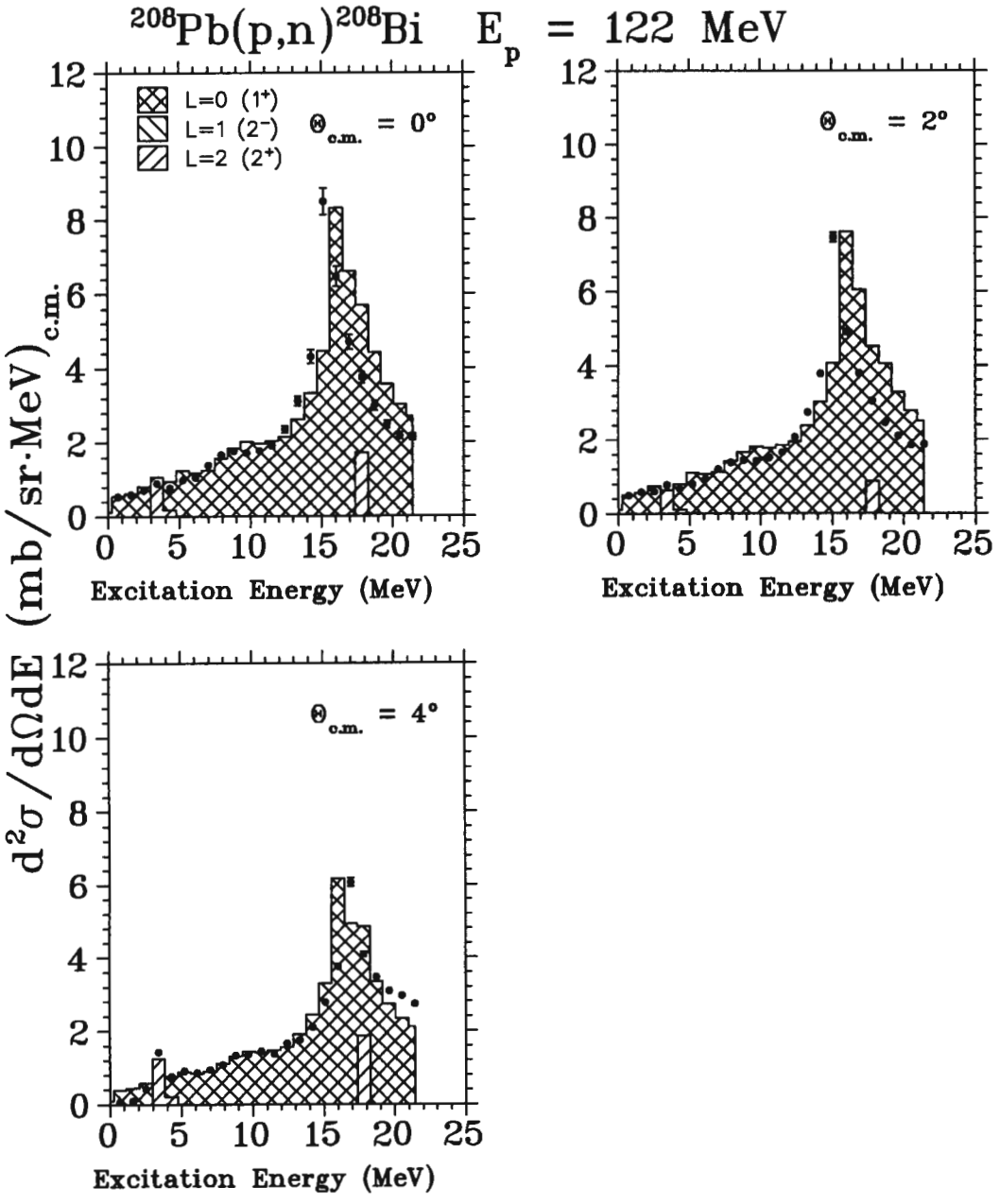

Figure A.5: *Multipole decomposed spectra for the* ^{208}Pb(p,n)^{208}Bi *data at* $\Theta_{c.m.} = 0°$, *2° and 4°. The assumed L- and* J^{π} *- transfers are shown.*

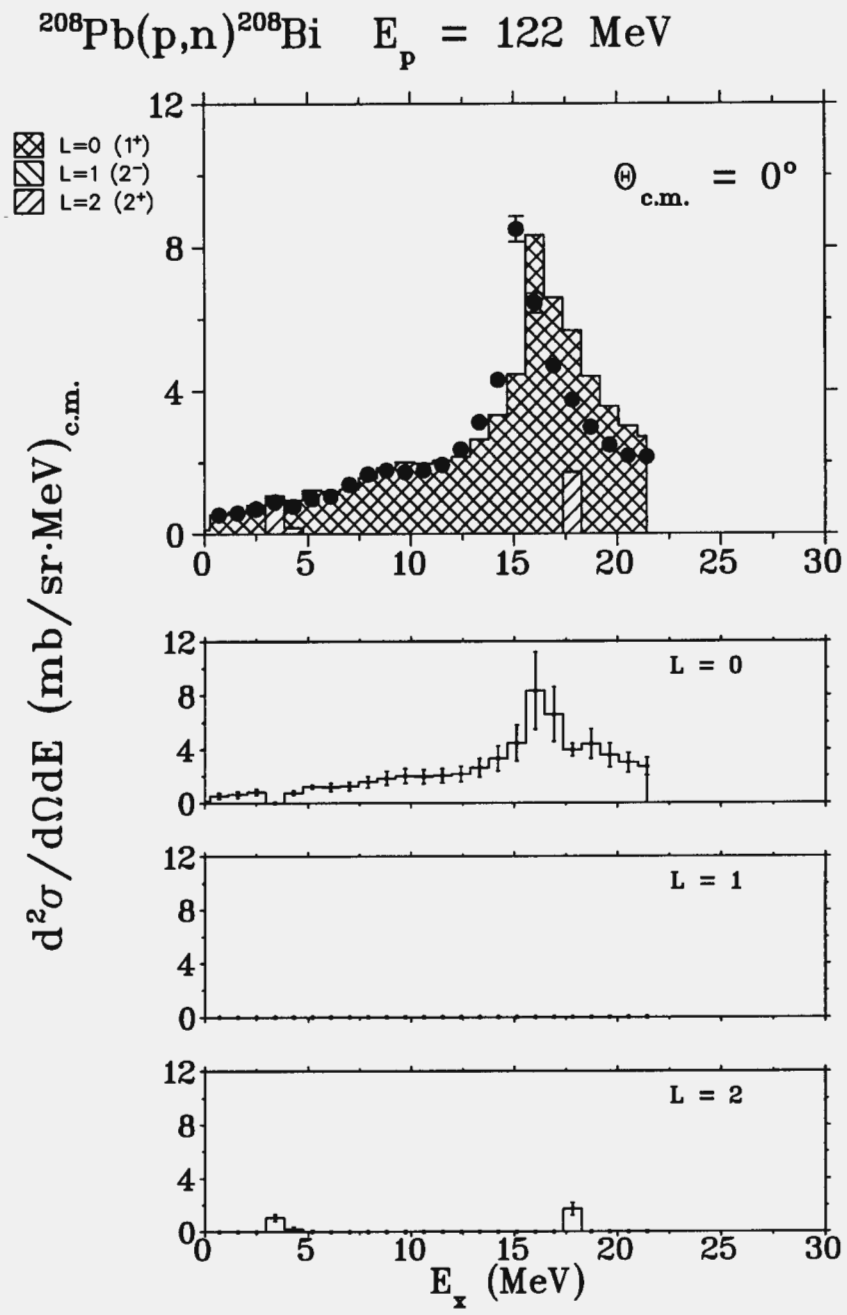

Figure A.6: *Multipole decomposed spectra for* ^{208}Pb(p,n)^{208}Bi *data at* $\Theta_{c.m.} = 0°$, *and individual* $\sigma(\theta)^{J^\pi}$*'s shown with uncertainties from a* χ^2*-minimization routine. The assumed L- and* J^π*- transfers are shown.*

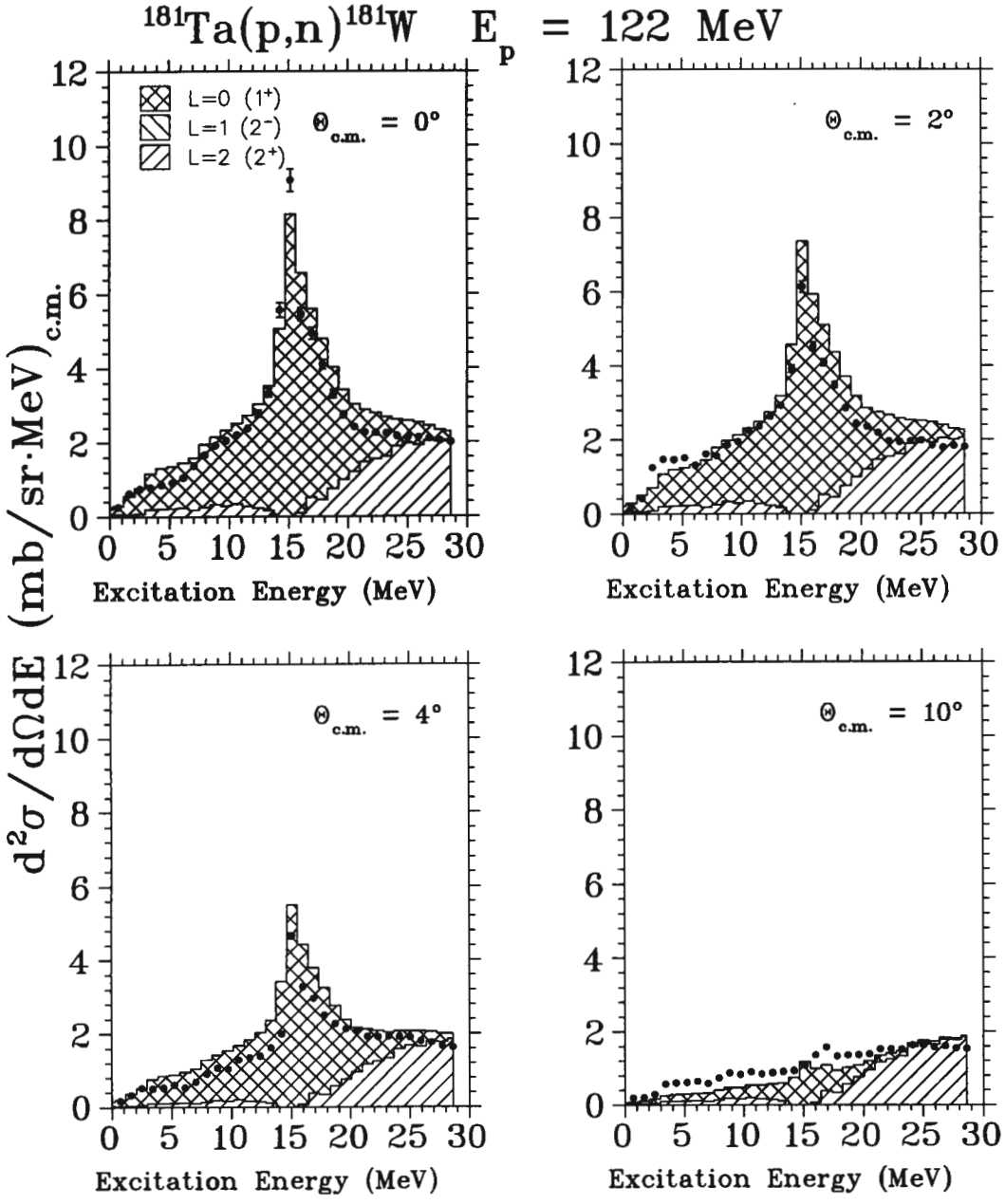

Figure A.7: *Multipole decomposed spectra for the* ^{181}*Ta*(p,n)^{181}*W data at* $\Theta_{c.m.}$*=0°, 2°, 4° and 10°. The assumed L- and* J^π*- transfers are shown.*

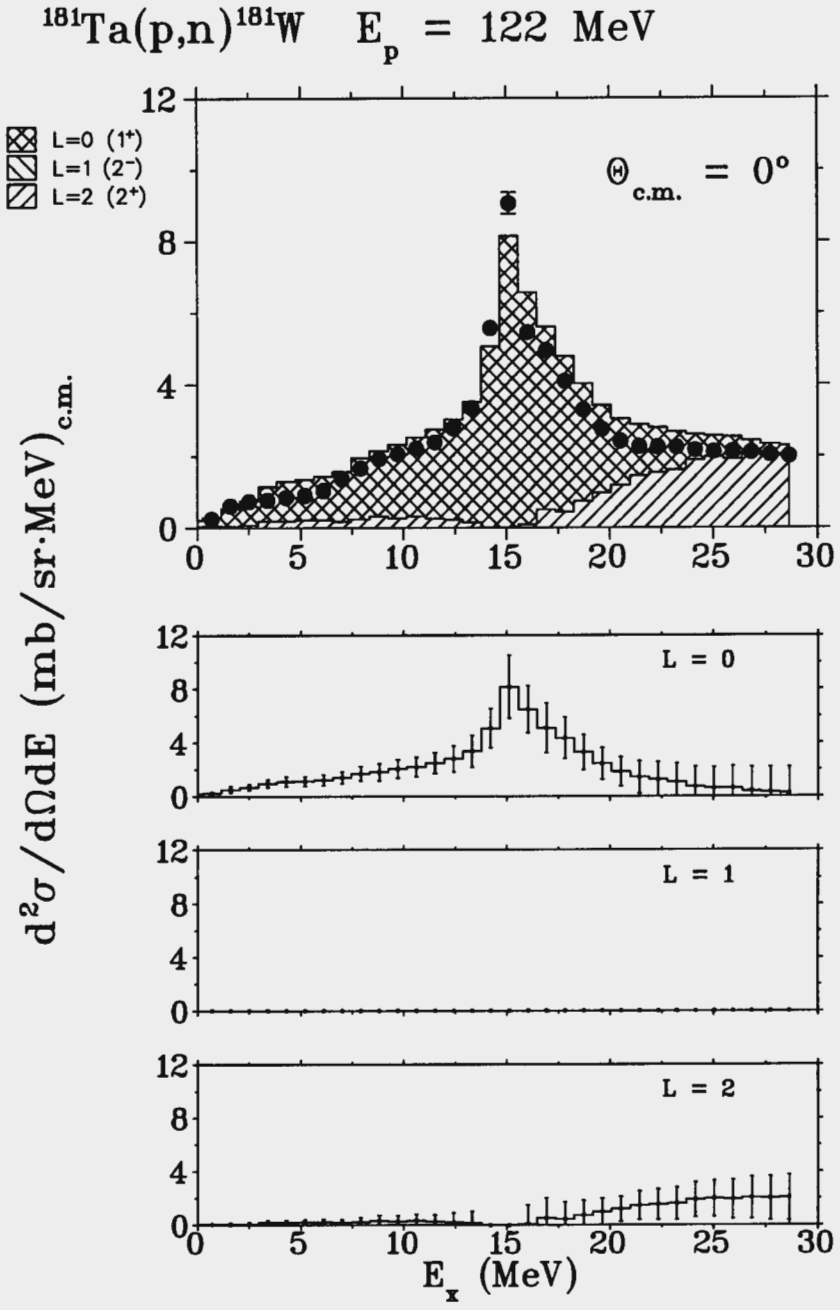

Figure A.8: *Multipole decomposed spectra for* ^{181}*Ta*(p,n)^{181}*W data at* $\Theta_{c.m.} = 0°$*, and individual* $\sigma(\theta)^{J^\pi}$*'s shown with uncertainties from a* χ^2*-minimization routine. The assumed L- and* J^π*- transfers are shown.*

Appendix B

Systematic errors

The systematic errors associated with beam current, target thickness, efficiency, deadtime and solid angle are all avoided because all B(GT) are calculated by normalizing to the IAS. Three types of systematic errors are involved in this experiment.

B.1 Systematic error of type A

The size and shape of the GTGR is not precisely known, and the fraction of $B(GT)$ associated with the ^{208}Pb(p,n)^{208}Bi reaction is mainly dependent on the choice of Gaussians that contribute to the GTGR and the region of excitation above the GTGR, and on into the continuum. The $\Delta B(GT)_{GTGR}$ systematic error due to exclusion or inclusion of fitted or part of fitted Gaussian number N is given by:

$$\Delta B(GT)_{GTGR} = \sum_{i=1}^{N} B(GT)_i - \sum_{i=1}^{N-1} B(GT)_i \qquad \text{(B.1)}$$

$$= B(GT)_N$$

Fitted spectra are shown in figures B.1 and B.2.

Good MDA must be performed before applying this estimation accurately. For the ^{208}Pb(p,n)^{208}Bi reaction data was collected only at angles of 0°, 2°, 4°, but not 10°. This was not enough to properly decompose the spectra. It was assumed that the decomposed ^{208}Pb(p,n)^{208}Bi spectra will be similar to that of ^{181}Ta(p,n)^{181}W spectra, since the relative contribution of various multipoles will depend mainly on reaction mechanism, and only weakly on details of nuclear structure.

Decomposed ^{181}Ta(p,n)^{181}W spectra suggest that a certain amount of strength be included or excluded from the fitted ^{208}Pb(p,n)^{208}Bi and ^{181}Ta(p,n)^{181}W spectra.

The 10% B(GT) subtracted from ^{208}Pb(p,n)^{208}Bi spectra in the region of 0 to 15 MeV contributes -2 to the systematic error. The inclusion of about 15% of fitted Gaussian number 16 contributes +5 to the systematic error in the $B(GT)$.

Similarly, the 10% B(GT) subtracted from ^{181}Ta(p,n)^{181}W spectra in the region of 0 to 15 MeV contributes -3 to the systematic error. The inclusion of about 15% of fitted Gaussian number 11 in the spectrum associated with the ^{181}Ta(p,n)^{181}W reaction contributes +2 to the systematic error in the $B(GT)$.

B.2 Systematic error of type B

The systematic error of type B only affects odd mass nuclei. It is dependent on the percentage of the IAS that is considered to be Fermi strength. The IAS in odd mass nuclei is made up of Fermi strength and a fraction of GT

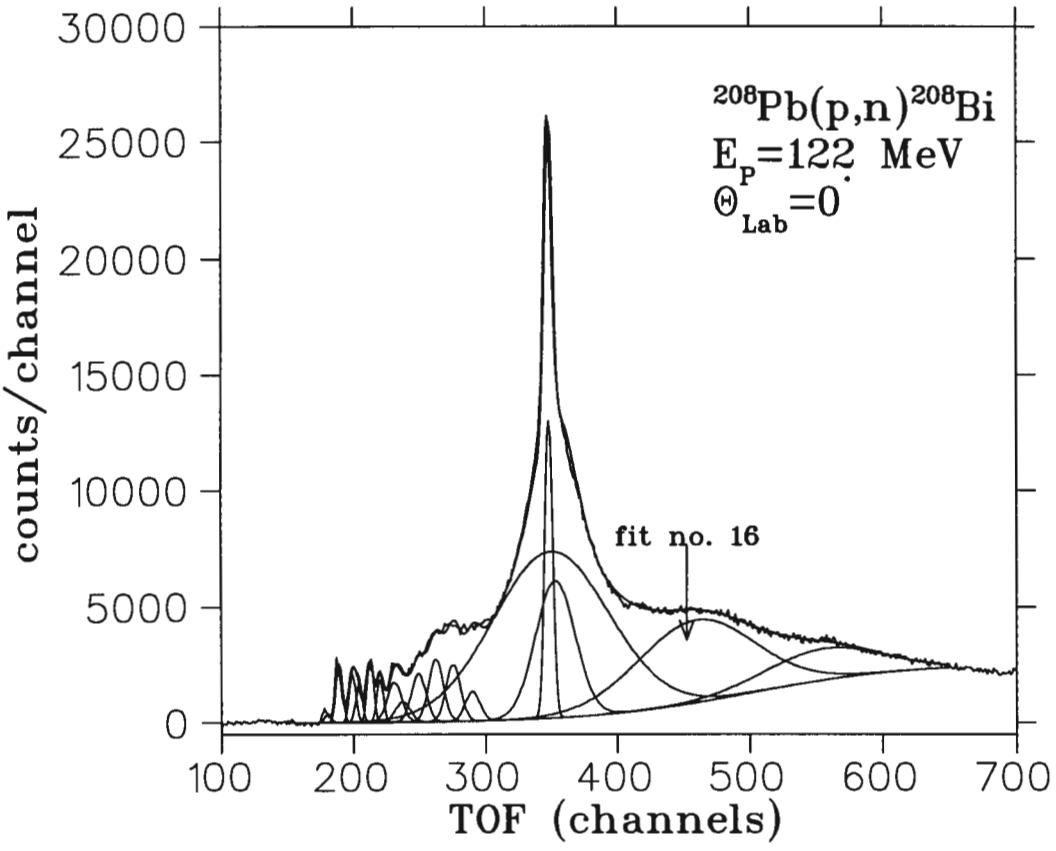

Figure B.1: *Neutron time-of-flight spectra at* $\Theta_{\mathrm{Lab}} = 0°$ *associated with the* $^{208}Pb(\mathrm{p,n})^{208}Bi$ *reaction at* E_{p}*=122 MeV. Systematic error increases by +5, if 15% of* $B(GT)$ *associated with fitted Gaussian number 16 is included in the total* $B(GT)$.

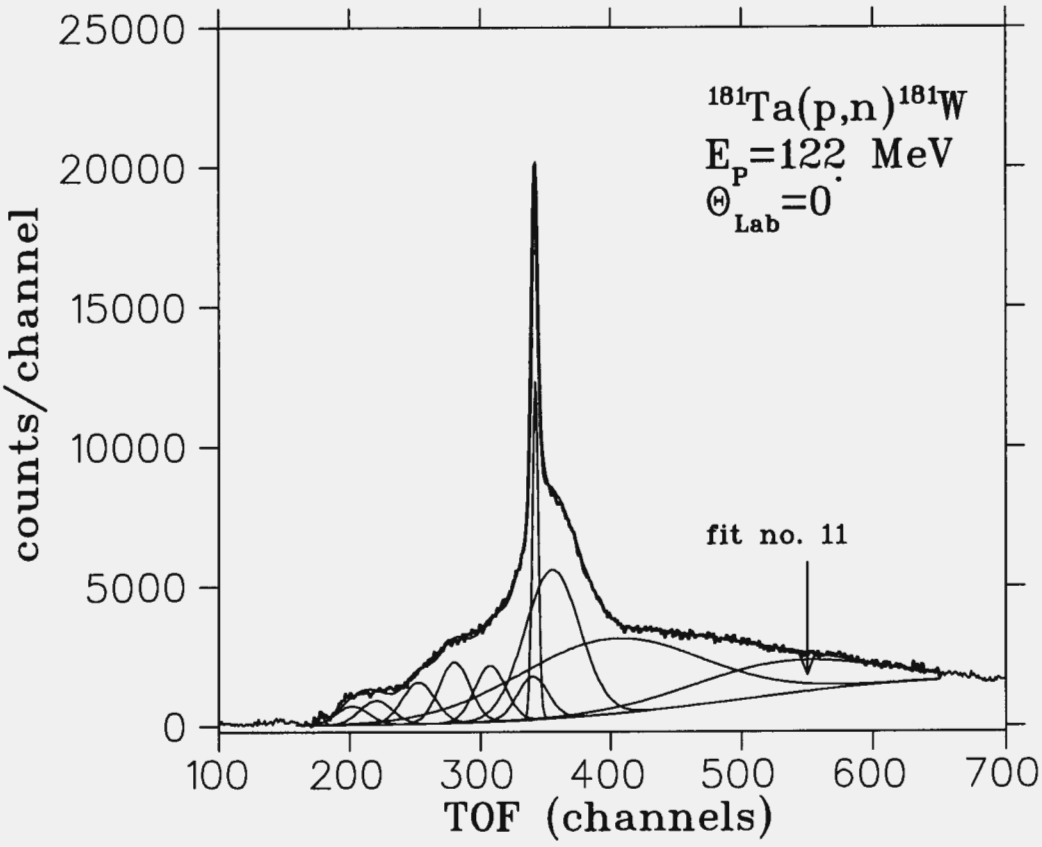

Figure B.2: *Neutron time-of-flight spectra at* $\Theta_{\mathrm{Lab}} = 0°$ *associated with the* $^{181}Ta(\mathrm{p,n})^{181}W$ *reaction at* E_{p}*=122 MeV. Systematic error increases by +2, if 15% of* $B(GT)$ *associated with fitted Gaussian number 11 is included in the total* $B(GT)$.

f_{GT}	$B(GT)_{sumrule}$	$\sum B(GT)$
0.0	105	67.15
0.1	105	74.56
0.2	105	83.97
0.3	105	95.89

Table B.1: *Gamow-Teller strength extracted from the spectrum with* ^{181}Ta(p,n)^{181}W *reaction for different fractions of* (f_{GT}) *in the IAS.*

strength f_{GT}. The f_{GT} is not known in the case of,[1] Ta target, an odd mass nucleus. The $B(GT)$ was calculated by assuming that the Fermi strength has exhausted the IAS, i.e. that $f_{GT} = 0$.
Then if $B(IAS) = B(F)$ then B(GT) = $B(GT)_{f_{GT}=0}$. However if $B(F)$ = fraction of $B(IAS)$ then B(GT) = $B(GT)_{f_{GT}=0.2}$ then the systematic error is given by:

$$\Delta B(GT) = B(GT)_{f_{GT}=0} - B(GT)_{f_{GT}=0.2} \tag{B.2}$$

The difference in the B(GT) calculated by assuming $f_{GT} = 0$, ie. the Fermi transition exhausts 100% of the IAS, and the B(GT) calculated by assuming that $f_{GT} = 0.2$ is 17 units. Thus the systematic error associated with the choice of f_{GT}, namely $f_{GT} = 0$ can be taken to be $^{+17}_{-0}$.

B.3 Addition of systematic error components

The total systematic error in $B(GT)$ associated with ^{208}Pb(p,n)^{208}Bi reaction is only that of type A and is $^{+5}_{-2}$. However the systematic error in $B(GT)$

[1] To estimate this strength one needs to know the $B(GT)$ strength of a state whose strength is also known from β decay.

associated with ^{181}Ta(p,n)^{181}W reaction is the sum of systematic errors of type A and B and is $^{+2}_{-3} + ^{+17}_{-0} = ^{+19}_{-3}$.

References

[Alv 38] L. W. Alvarez, Phys. Rev. **54** 609 (1938).

[And 61] J. D. Anderson and C. Wong, Phys. Rev. Lett. **7** (1961) 250.

[And 62] J. D. Anderson, C. Wong and J. W. McClure, Phys. Rev. **126** (1962) 2170.

[And 80] B. D. Anderson, J. N. Knudson, P. C. Tandy, J. W. Watson, R. Madey, and C. C. Foster, Phys. Rev. Lett. Vol. **45** (1980) 699.

[Bai 80] D. E. Bainum, J. Rapaport, C. D. Goodman, D. J. Horen, C. C. Foster, M. B. Greenfield, and C. A. Goulding, Phys. Rev. Lett. **44** (1980) 1751.

[Bal 47] G. G. Baldwin and G. S. Klaiber, Phys. Rev. **71** (1947) 3; ibid **73** (1948) 1156.

[Ber 70] A. Bernstein, *Advances in Nuclear Physics*, Vol. 3 (Plenum, New York 1970) 325.

[Ber 75] B. L. Berman and S. C. Fultz, Rev. Mod. Phys. **47** (1975) 713.

[Ber 72] G. F. Bertsch, *The practitioner's Shell Model*, (North-Holland, Amsterdam, 1972).

[Ber 78] G. F. Bertsch and I. Ichimura, and A. Arima, Nucl. Phys. **A226** (1978) 282.

[Blo 91] J. Blomgren, *Experimental studies of giant resonances in medium-weight spherical nuclei*, (Uppsala, 1991).

[Bue 79] M. Buenerd, D. Lebrun, P. Martin, J. Chauvin, G. Duhamel, G. Perrin, and P. de Saintignon, Phys. Lett. **84B** (1979) 305.

[Bet 57] H. A. Bethe and J. Goldstone, Proc. Roy. Soc **A238** (1957) 551.

[Bet 71] H. A. Bethe, Ann. Rev. Nucl. Sci. **21** (1971) 93.

[Ber 87] G. F. Bertsch and H. Esbensen, Rep. Prog. Phys. **50** (1987) 607.

[Boh 69] A. Bohr and B. Mottelson, *Nuclear Structure* Vol. I (1969) and Vol. II (1975) (Benjamin, New York).

[Bru 54] K. A. Brueckner, Phys. Rev. **96** (1954) 508.

[Bru 55] K. A. Brueckner and C. A. Levinson, Phys. Rev. **97** (1955) 1344.

[Car 86] M. Carchidi, B. H. Wildenthal and B. A. Brown, Phys. Rev. C**34** (1986) 2280.

[Cec 79] R. A. Cecil, B. D. Anderson, R. Madey, Nucl. Instr. and Meth. **161** (1979) 439.

[Com 81] Program DWBA70, R. Schaeffer and J. Raynal (unpublished); extended version DW81 by J. R. Comfort (unpublished).

[Day 67] B. D. Day, Rev. Mod. Phys. **39** (1967) 719; Phys. Rev. **C24** (1981) 1203.

[Doe 75] R. R. Doering, A. Galonsky, D. M. Patterson, and G. F. Bertsch, Phys. Rev. Lett. **35** (1975) 1691.

[Erk 74] K. Erkelenz, Phys. Rep. **13** (1974) 191.

[Fla 89] B. S. Flanders, R. Madey, B. D. Anderson, A. R. Baldwin, and J. W. Watson, Phys. Rev. **C40** (1989) 1985.

[Fra 85] M. A. Franey and W. G. Love Phys. Rev. C31 488 (1985).

[Gaa 81] C. Gaarde, J. Rapaport, T. N. Taddeucci, C. D. Goodman, C. C. Foster, D. E. Bainum, C. A. Goulding, M. B. Greenfield, D. J. Horen, and E. Sugarbaker, Nucl. Phys. **A369** (1981) 258.

[Gaa 85] C. Gaarde, *Proc. of the Niels Bohr Cent. Conf. on Nuclear Structure*, edited by R. Broglia et al., North-Holland, Amsterdam, (1985) 499c.

[Goo 79] C. D. Goodman, *The (p,n) reaction and the nucleon-nucleon force* edited by C. D. Goodman et al. (Plenum, New York, 1979).

[Goo 80] C. D. Goodman, C. A. Goulding, M. B. Greenfield, J. Rapaport, D. E. Bainum, C. C. Foster, W. G. Love, and F. Petrovich, Phys. Rev. Lett. **44** (1980) 1755.

[Goo 83] C. D. Goodman, *in proceedings of the International Conference on Nuclear Physics, Florence, 1983* edited by P. Blasi and R. A. Ricci. (Tipografia Compositori, Bologna, 1983).

[Goo 83] C. D. Goodman, Prog. in Part and Nucl. Phys. 475 (1983).

[Gou 81] C. R. Gould, L. G. Holzsweig, S. E. King, Y. C. Lau, R. V. Poore, N. R. Roberson, and S. A. Wender, IEEE Trans. Nucl. Sci. **NS-28**, 3708 (1981).

[Gou 83] C. R. Gould and N. R. Roberson, and S. A. Wender, IEEE Trans. Nucl. Sci. **NS-30** 5, 3758 (1983).

[Gro 83] K. Grotz, H. V. Klapdor, J. Metzinger, R. Madey, W. Pairsuwan, B. D. Anderson, A. R. Baldwin, B. S. Flanders, C. Lebo, J. W. Watson, and C. C. Foster, Phys. Lett. **126B**, (1983) 417.

[Har 77] M. N. Harakeh, B. van Heyst, K. van der Borg and A. van der Woude, Phys. Lett. **38** (1977) 676; Nucl. Phys. **A327** (1979) 373.

[Hol 77] K. Holinde and R. Machleidt, Nucl. Phys. **A280** (1977) 429.

[Hol 81] K. Holinde, Phys. Rep. **68** (1981) 121.

[Hor 80] D. J. Horen, C. D. Goodman, C. C. Foster, C. A. Goulding, M. B. Greenfield, J. Rapaport, E. Sugarbaker, T. G. Masterson, F. Petrovich, W. G. Love, Phys. Lett. **95B** (1980) 27.

[Hor 81] D. J. Horen, C. D. Goodman, D. E. Bainum, C. C. Foster, C. Gaarde, S. A. Goulding, M. B. Greenfield, J. Rapaport, T. N. Taddeucci, E. Sugarbaker, T. G. Masterson, S. M. Austin, A. Galonsky, and W. Sterrenburg, Phys. Lett. **99B** (1981) 383.

[Ike 63] K. I. Ikeda, S. Fujii, and J. I. Fujita, Phys. Lett. **3** (1963) 271.

[Jam 75] F. James and M. Roos, Comput. Phys. Commun. **10** 343 (1975).

[Ker 59] A. K. Kerman, H. McManus and R. M. Thaler, Ann. Phys. **8** (1959) 551.

[Lac 80] M. Lacombe, B. Loiseau, J. M. Richard, R. Vinh Mau, J. Cote, P. Pires and R. de Tourreil, Phys. Rev. **C21** (1980) 861.

[Leb 80] D. Lebrun, M. Buenerd, P. Martin, P. de Saintignon and G. Perrin, Phys. Lett. **97B** (1980) 358.

[Lew 72] M. B. Lewis and F. E. Bertrand, Nucl. Phys. **A196** (1972) 337.

[Lov 78] W. G. Love, Nucl. Phys. **A312** (1978) 160.

[Lov 80] W. G. Love, *The (p,n) Reaction and the Nucleon-Nucleon Force*, edited by C. D. Goodman, S. M. Austin, S. D. Bloom, J. Rapaport, G. R. Satchler (Plenum, New York, 1980), p. 23.

[Lov 81] W. G. Love and M. A. Franey, Phys. Rev. **C24** (1981) 1073.

[Lov 84] W. G. Love, M. A. Franey, and F. Petrovich, *Proc. of the Intern. Conf. on Spin Excitations in Nuclei*, ed. by F. Petrovich et al. (Plenum, New York, 1984), p. 205.

[Mac 87] R. Machleidt, K. Holinde, and Ch. Elster, Phys. Rep. **149** (1987) 1.

[Mad 89] R. Madey, B. S. Flanders, B. D. Anderson, A. R. Baldwin, J. W. Watson, S. M. Austin, C. C. Foster, H. V. Klapdor, and K. Grotz, Phys. Rev. **C40** (1989) 540.

[Mar 75] N. Marty, M. Morlet, A. Willis, V. Comparat, and R. Frascaria, *Proc. of the Intern. Conf. on Highly Excited States in Nuclei*, Julich, F. R. G., 1975, edited by A. Faessler, C. Mayer-Boricke, and P. Turek (KFA Julich, F. R. G., 1975) Vol. I, p. 17.

[Mar 92] Program ELOSS V2.0 (1984), P. Jipsen (unpublished);
extended version (1992) by J. Maritz (unpublished).

[McC 87] J. B. McClelland et al., Can. Jour. Phys. **65** (1987) 633.

[Nad 81] A. Nadasen, P. Schwandt, P. P. Singh, W. W. Jacobs, A. D. Bacher, P. T. Debevec, M. D. Kaitchuck, and J. T. Meek, Phys. Rev. **C23** 1023 (1981).

[Nag 78] M. M. Nagels, T. A. Rijken and J. D. de Swart, Phys. Rev. **D17** (1978) 768; D20 (1979) 1633.

[New 91] R. T. Newman, M.Sc. Thesis, University of Cape Town (1991) (unpublished).

[Ost 85] F. Osterfeld, D. Cha, and J. Speth, Phys. Rev. **C31** (1985) 372.

[Ost 92] F. Osterfeld, Reviews of Mordern Physics, Vol. 64, No. 2, April 1992.

[Par 91] B. K. Park, Ph.D. Thesis, University of Ohio (1991) (unpublished).

[Pet 69] F. Petrovich, H. McManus, V. A. Madsen, and J. Atkinson, Phys. Rev. Lett. **22** (1969) 895.

[Pet 79] F. Petrovich and W. G. Love, *Proceedings of LAMPF Workshop on Pion Single Charge Exchange*, Los Alamos, New Mexico, 1979 (unpublished), Document No. LA-7892C.

[Pet 80a] F. Petrovich, *Proc. of the Intern. Conf. on The (p,n) Reaction and the Nucleon-Nucleon Force*, edited by F. Petrovich et al. (Plenum, New York, 1980).

[Pet 80b] F. Petrovich, W. G. Love and R. J. McCarthy, Phys. Rev. **C21**, 1718 (1980).

[Pet 81] F. Petrovich and W. G. Love, Nucl. Phys. **A354** (1981) 499c.

[Pet 84] F. Petrovich, *Proc. of the Intern. Conf. on Spin Excitations in Nuclei*, edited by F. Petrovich et al. (Plenum, New York, 1984).

[Pet 86] F. Petrovich, J. A. Carr, and H. McManus, Ann. Rev. Nucl. Part. Sci. **36** (1986) 29.

[Pit 71] R. Pitthan and Th. Walcher, Phys. Lett. **36B** (1971) 563.

[Pil 88] J. V. Pilcher, NAC internal report, (National Accelerator Centre, Faure, 1988).

[Pil 92] J. V. Pilcher, NAC internal report, (National Accelerator Centre, Faure, 1992).

[Rab 92] H. B. M. Raben, Ph.D. Thesis, Urije Universiteit (1992) (unpublished).

[Rap 81] J. Rapaport, T. N. Taddeucci, C. Gaarde, C. D. Goodman, C. C. Foster, C. A. Goulding, D. J. Horen, E. Sugarbaker, T. G. Masterson, and D. Lind, Phys. Rev. **C34** (1981) 335.

[Rap 88] J. Rapaport, in *Workshop on Nuclear Structure with Medium Energy Probes*, (Santa Fe, New Mexico, 1988, World Scientific Publ. Company, Singapore).

[Ros 80] C. M. Rosza et al. Phys. Rev. **C21** 1980) 1252.

[Sat 64] G. R. Satchler, Nucl. Phys. **55**, 1 (1964).

[Sat 83] G. R. Satchler, *Direct Nuclear Reactions*, (Clarendon Press Oxford, New York 1983).

[Sty 97] D. Steyn, Ph.D. Thesis, University of Cape Town (1997) (unpublished).

[Tad 81] T. N. Taddeucci, J. Rapaport, D. E. Bainum, C. D. Goodman, C. C. Foster, C. Gaarde, J. Larsen, C. A. Goulding, D. J. Horen, T. Masterson, and E. Sugarbaker, Phys. Rev. **C25** (1981) 1094.

[Tad 87] T. N. Taddeucci, C. A. Goulding, T. A. Carey, R. C. Byrd, C. D. Goodman, C. Gaarde, J. Larsen, D. J. Horen, J. Rapaport and E. Sugarbaker, Nucl. Phys. **A469** (1987) 125.

[Tak 74] K. Takayanagi, K. Shimizu, and A. Arima, Nucl. Phys. **A226** (1974) 282.

[Tow 83] I. S. Towner, and F. C. Khanna, Nucl. Phys. **A226** (1983) 282.

[Tsh 92] V. M. Tshivhase, M.Sc. Thesis, University of Cape Town (1992) (unpublished).

[You 77] D. H. Youngblood, C. M. Rozsa, J. M. Moss, D. R. Brown, and J. D. Bronson, Phys. Rev. Lett. **39** (1977) 1188.

[You 81] D. H. Youngblood, J. D. Bronson, U. Garg, Y. W. Lui and C. M. Rozsa, Phys. Rev. **C23** (1981) 1997.

[Wat 85] J. W. Watson, W. Pairsuwan, B. D. Anderson, A. R. Baldwin, B. S. Flanders, R. Madey, R. J. McCarthy, B. A. Brown, B. H. Wildenthal, and C. C. Foster, Phys. Rev. Lett. **55** (1985) 1369.